DEVELOPMENT OF A COUPLED DEPTH AVERAGED-RANS 3D MODEL FOR OPEN CHANNEL FLOW USING HIGHER-ORDER UPWINDING SCHEMES

M.Sc. Engineering Thesis

By

NAILA MATIN

Student ID: 1018162006 P

DEPARTMENT OF WATER RESOURCES ENGINEERING

BANGLADESH UNIVERSITY OF ENGINEERING AND TECHNOLOGY,

DHAKA-1000, BANGLADESH

JANUARY 2023

DEVELOPMENT OF A COUPLED DEPTH AVERAGED-RANS 3D MODEL FOR OPEN CHANNEL FLOW USING HIGHER-ORDER UPWINDING SCHEMES

M.Sc. Engineering Thesis

By

NAILA MATIN

Student ID: 1018162006 P

DEPARTMENT OF WATER RESOURCES ENGINEERING

BANGLADESH UNIVERSITY OF ENGINEERING AND TECHNOLOGY,

DHAKA-1000, BANGLADESH

JANUARY 2023

DEVELOPMENT OF A COUPLED DEPTH AVERAGED-RANS 3D MODEL FOR OPEN CHANNEL FLOW USING HIGHER-ORDER UPWINDING SCHEMES

Submitted by

Naila Matin

(Student ID: 1018162006 P)

In partial fulfillment of the requirement for the degree of

MASTER OF SCIENCE IN WATER RESOURCES ENGINEERING

DEPARTMENT OF WATER RESOURCES ENGINEERING

BANGLADESH UNIVERSITY OF ENGINEERING AND TECHNOLOGY,

DHAKA-1000, BANGLADESH

JANUARY 2023

CERTIFICATION OF APPROVAL

The thesis titled "Development of a Coupled Depth Averaged-RANS 3D Model for Open Channel Flow Using Higher-Order Upwinding Schemes" submitted by Naila Matin, Student ID: 1018162006 P, Session: October 2018, has been accepted as satisfactory in partial fulfillment of the requirement for the degree of **Master of Science in Water Resources Engineering** on **9th January 2023**.

.....
Dr. A T M Hasan Zobeyer
Professor
WRE, BUET, Dhaka

Chairman
(Supervisor)

.....
Dr. A T M Hasan Zobeyer
Professor and Head
WRE, BUET, Dhaka

Member
(Ex-Officio)

.....
Dr. Md. Mostafa Ali
Professor
WRE, BUET, Dhaka

Member

.....
Dr. Badal Mahalder
Associate Professor
WRE, BUET, Dhaka

Member

.....
Dr. Mohammad Nasim Hasan
Professor
ME, BUET, Dhaka

Member (External)

CANDIDATE'S DECLARATION

It is hereby declared that this thesis or any part of it has not been submitted elsewhere for the award of any degree or diploma.

Signature of the Candidate

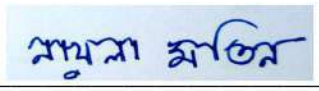

Naila Matin

TABLE OF CONTENTS

Table of Contents

LIST OF FIGURES

LIST OF TABLES

LIST OF ABBREVIATIONS

CFD	Computational Fluid Dynamics
NS	Navier-Stokes
RANS	Reynolds-Averaged Navier–Stokes
DA	Depth-Averaged
RANS-H	Reynolds-Averaged Navier–Stokes Hydrostatic
RANS-NH	Reynolds-Averaged Navier–Stokes Non-Hydrostatic
VOF	Volume of Fluid
NUV	Non-Uniform Velocity
NHP	Non-Hydrostatic Pressure
TVD	Total Variation Diminishing
NRMSE	Normalized Root Mean Square Error
NV	Normalized Variance

LIST OF SYMBOLS

b = half width of curved channel.

c_r = Courant number;

d = distance from bed;

g = acceleration due to gravity;

H = water surface elevation;

k_s = bed roughness height;

N = number of iteration of the DA-RANS model;

n = number of time step;

P = instantaneous pressure;

p = pressure;

p_{hs} = hydrostatic pressure;

p^p = non-hydrostatic pressure;

q_x, q_y = discharge per unit width;

t = time;

U,V,W = instantaneous point velocity in the x, y and z directions;

u,v,w = time averaged point velocity in the x, y and z directions;

u',v',w' = fluctuating velocity;

$\bar{u}, \bar{v}, \bar{w}$ = depth averaged velocity

u^p , v^p , w^p = perturbation velocity;

U_c , V_c, W_c = contravariant velocity components;

$\overline{U_c}, \overline{V_c}$ = depth averaged contravariant velocity components;

X, Y = correction terms;

Y_R = radial distance from the centerline of a bend;

$x, y, z =$ Cartesian coordinates;

$z_n =$ normal distance from bed;

$\Delta t =$ time step;

$\rho =$ density of water;

ξ , η , ζ= curvilinear coordinates;

$\xi_x, \xi_y, \xi_z, \eta_x, \eta_y, \eta_z, \zeta_x, \zeta_y, \zeta_z$ = matrices of transformation;

σ_x^v, σ_y^v , σ_z^v = viscous normal stress;

τ_{xy}^v, τ_{yz}^v , τ_{zx}^v = viscous shear stress;

σ_x, σ_y , σ_z = turbulent normal stress;

τ_{xy}, τ_{yz} , τ_{zx}= turbulent shear stress;

ACKNOWLEDGEMENT

I would like to express my deepest gratitude and appreciation to my supervisor Dr. A T M Hasan Zobeyer, whose guidance, support and expertise were invaluable throughout my research. His continuous encouragement and constructive feedback were instrumental in the successful completion of this work.

I am also thankful to the members of the Board of Examination, Dr. Md. Mostafa Ali, Professor, Department of WRE, BUET, Dr. Badal Mahalder, Associate Professor, Department of WRE, BUET, and Dr. Mohammad Nasim Hasan, Professor, Department of ME, BUET for their valuable and constructive suggestions regarding this study.

Finally, and most importantly, I am indebted to my parents, my sister and my husband for their unconditional love, support and relentless faith in me, which keeps me going even during the toughest of times.

ABSTRACT

The analysis of flow in open channels is of fundamental importance in river engineering and related areas. In numerical simulations of open channels, predictions of flow conditions are generally conducted through one and two-dimensional depth-averaged (DA) models. While the 2D models are relatively simpler and require less computational effort, they fall short in representing complex flow phenomena, where the flow field has highly non-uniform velocity and non-hydrostatic pressure, which requires the use of complete three-dimensional models. However, 3D modeling can be more computationally intensive and require sophisticated techniques. In an effort to develop a 3D river model requiring computational time comparable to that of 2D models, a novel approach was formulated by coupling both DA and 3D Reynolds-Averaged Navier-Stokes (RANS) model, that enabled faster convergence but at the same time provided high accuracy of 3D models. However, the RANS 3D model used only the first-order upwind method to resolve the advective terms, which, although stable in simulating advection, are also known to suffer from excessive numerical diffusion. In the present study, a RANS 3D model is developed by implementing higher-order discretization of the convective terms.

To select suitable higher-order schemes for the RANS model, at first, thirty higher-order schemes were tested for pure advection as a preliminary assessment of the methods against the analytical solution in a simpler context. The best performing five methods were identified as the Adaptive stencil, Superbee, fifth-order upwinding with limiter, QUICKEST, and MUSCL schemes. For one of the test cases with triangular distribution, the normalized root mean square error (NRMSE) and the normalized variance (NV) index for the first-order upwinding method were calculated to be 10.09 and -10.37, respectively. Whereas for the same test case, NRMSE values were in the range of 1.93 to 3.45 for the top five schemes, suggesting reasonably good accuracy, and NV indices were within ±0.5, indicating that they were neither too diffusive nor compressive.

The best-performing methods were then selected and used in the RANS model. Initially, performance of the higher-order schemes were investigated for various 2D plane flow scenarios, where the flow varied only in the longitudinal and vertical directions. The model was verified with experimental results of flow development, flow over a symmetric hump

and series of dunes. The validated model was then used to simulate synthetic scenarios of flow over dunes in long reaches with different numerical grid coarseness in the longitudinal flow direction. The higher-order schemes resulted in 20-30% better results for coarser grid resolution, especially the second-order upwind, Adaptive and QUICKEST schemes.

Finally, the 3D model was developed with these selected higher-order schemes and different flow scenarios were simulated. The higher-order methods provided more accurate solutions against the mesh-independent solution than the first-order differencing methods. A comparative analysis was also done, with gradual coarsening of the numerical grid, between the increased savings in computational time and the associated accuracy of flow variables, and the QUICKEST scheme was found to perform better than the other methods. The upgraded 3D model with selected higher-order schemes was also used to simulate a real case open channel flow scenario of Padma River near Naria Upazila. The 3D model provided almost a 10-15% increase in the overall surface velocity of the channel from the 2D depth-averaged model and at the same time, significantly higher bed shear stress was observed in some locations. Near-bed vortex was also simulated in the 3D model which may cause undercut of bank and increases the potential for bank erosion. The 3D model was able to provide a greater level of information regarding the flow variables while at the same time having a computational time comparable to that of a 2D model.

CHAPTER 1

INTRODUCTION

1.1. Background

A thorough understanding of river hydrodynamics is essential for addressing the various environmental and engineering issues related to flow patterns, design of hydraulic structures, sediment transport, channel geomorphology, etc. Currently, mathematical models are widely used in modeling river hydrodynamics for developing strategies for managing and protecting these systems. Numerical modeling allows researchers and engineers to study the behavior of fluids in open channels under a wide range of conditions, including conditions that may be difficult or impossible to recreate in the laboratory. It can also be used to study the time-varying behavior of the fluid and the impact of complex geometries and large-scale systems.

Until recently, predictions of flow conditions have been made mostly using one-dimensional or two-dimensional depth-averaged (DA) models due to their simplicity. Although DA simulations require relatively less computational effort, they often do not reflect actual flow behavior due to their inherent assumption of uniform velocity and hydrostatic pressure distribution. It often falls short in accurately representing the rapidly varied flows with highly non-uniform velocity distribution and non-hydrostatic pressure, as the 2D equations do not provide any vertical details of the flow fields. As a result, 2D simulations are only applicable for flows that have a larger length scale compared to the flow depth. To overcome the limitations of the 2D models and to obtain more accurate flow characteristics in rivers or structures, researchers are becoming more interested in using 3D models for open channels. Although studies involving natural rivers with complex geometries are limited in numbers compared to 2D models, three-dimensional models are steadily gaining more popularity. Three-dimensional computational fluid dynamic (CFD) models have been developed based on the Reynolds-averaged- Navier-Stokes (RANS) equations. But even with the exponential growth in computing power in the last few decades, some challenges still remain in 3D

open channel flow modeling, namely computing the dynamic free surface, maintaining mass balance using a pressure-velocity coupling method with a large mesh aspect ratio and slow convergence towards steady state solution for large computational domains.

To address some of these challenges that have been identified in 3D modeling of natural rivers, a novel approach was formulated by coupling both depth-averaged and RANS models, in a previous study of Zobeyer (2012). In this coupled model, initially the water surface and DA velocity are estimated by a DA model neglecting non-uniform velocity and non-hydrostatic pressure. Then in the RANS model, the horizontal momentum and the continuity equations are solved for the horizontal and vertical velocity respectively, with the water surface from DA model as a fixed zero pressure boundary. The pressure Poisson equation is solved for the non-hydrostatic pressure as well, in the non-hydrostatic RANS model. This coupled model was able to conserve mass by devising correction terms, and enabled faster convergence of the 3D model requiring computational effort comparable to that of 2D depth-averaged models, even in large domains with a refined grid. However, one limitation there was the use of only first-order upwind method to discretize the advective terms in the RANS model. Although the low-order upwind schemes helps to maintain stability in simulating advection, their accuracy is only first-order in terms of Taylor series truncation error. Thus they suffer from excessive diffusion, particularly when the numerical grid has a coarse resolution. While increasing the resolution of the numerical grid can help to mitigate these issues, it is often not practical to use such high degree of refinement for modeling complex, rapidly changing, three-dimensional turbulent flows in engineering applications.

This numerical diffusion problem can be minimized by employing higher-order differencing of the advection term, which involves more neighbouring nodes, and reduce the discretization errors by bringing in a wider influence. Again with regard to efficiency, the higher-order methods allow for more accurate solutions to be obtained even in a coarser mesh compared to first-order differencing methods, which require a finer mesh to achieve similar levels of accuracy. So their use can potentially provide significant practical benefits in terms of accuracy, speed and storage requirements. The present study aims to implement higher-order advective schemes in the coupled DA-

RANS model and assess their performance in terms of accuracy and diffusivity. The methods were first tested for pure advection scenarios, which was followed by their applicability and performance analysis in 2D and 3D open channel flow models respectively.

1.2. Objectives of the study

The specific objectives of this study are given below:

i. To evaluate the performance of thirty higher-order upwinding schemes for 1D pure advection in terms of accuracy and stability.

ii. To develop a coupled DA-RANS 2D model with higher-order discretization of the advection terms for plane open channel flows and validate it against experimental data.

iii. To simulate different 2D plane open channel flow scenarios for coarser numerical grids using the selected higher-order schemes to obtain the best-performing methods.

iv. To extend the coupled model for 3D flow and simulate different flow scenarios.

1.3. Outline of the thesis

This thesis has been organized into five chapters, which are described below:

Chapter 1 contains an overview of the study's background, highlights the study's objectives and outlines of the study.

Chapter 2 discusses the literature review of the study. Through literature review, some context for the research being conducted is provided, thus helping to situate the research within the broader area of 3D modeling of open channel flow, and the existing knowledge gaps and scopes of the study were identified.

Chapter 3 details the methodology of the study step by step. The codes and model development procedures are presented, as well as the various test cases and evaluation methods used.

Chapter 4 presents the overall results and discussions of this study. First the results of the higher-order methods are described for pure advection case, followed by the coupled DA-RANS of 2D plane flow and finally, in the complete 3D open channel flow version. Several test cases were simulated in each stage, and the results were analyzed.

Chapter 5 summarizes the conclusions of this study. Some recommendations for future work are also provided.

CHAPTER 2

LITERATURE REVIEW

2.1. Introduction

In this chapter, many relevant studies have been reviewed for proper comprehension of the problems and to identify the existing knowledge gap. The reviewed studies helped significantly in understanding the present state of open channel flow modeling by providing context for the research being conducted, helping to place the research within the broader area of study and to highlight scopes of further contribution to the field.

2.2. Open channel flow modeling

Open channel flow refers to the movement of fluids, such as water, through channels or conduits that are not completely enclosed (Chaudhry, 2007). Natural channels, such as rivers and streams, as well as man-made channels, such as canals, irrigation ditches, and stormwater drains are all open channel flows (Chanson, 2004; French, 1985). Numerical modeling of open channel flow is a valuable tool for understanding and predicting the behavior of fluids in open channels, such as rivers and streams (Lai, 1986). It is used for a wide range of applications, including the design and analysis of hydraulic structures, the prediction of flood hazards, the assessment of the impacts of environmental factors, the study of ecosystem interactions, and the development of laboratory testing alternatives (Anees et al., 2016; Chao et al., 2017; Nagata et al., 2003; Pinder and Sauer, 1971). In some cases, conducting physical experiments to study open channel flow may not be practical or possible. In these cases, numerical modeling can be used as an alternative to laboratory testing, allowing researchers to study the behavior of the fluid under a wide range of conditions (Heller, 2011). Moreover, numerical modeling can be used to study the behavior of the fluid in large-scale systems, such as river basins or coastal regions, which may be impractical or infeasible to study in the laboratory (Nguyen et al., 2018). By using mathematical

and computational techniques, numerical modeling allows researchers and engineers to study the behavior of the fluid under a wide range of conditions and to make informed decisions about the management and protection of open channel flow systems.

To model the behavior of fluids in open channels, it is necessary to use numerical techniques to solve the partial differential equations that describe the motion of the fluid. These equations, known as the Navier-Stokes equations, are based on the principles of fluid mechanics and describe the relationship between the forces acting on the fluid and its motion (Temam, 2001). There are several different types of open channel flow models that are commonly used to study the behavior of fluids in open channels, such as rivers and streams. Two main types of open channel flow models are: depth-averaged model and complete 3D model (Neill et al., 2007). The choice of which type of model to use depends on the specific goals of the study and the balance between accuracy and computational efficiency that is required.

2.2.1. Depth averaged modeling

A depth-averaged model is a numerical model that represents the flow as a two-dimensional (2D) flow over the channel bed. Depth-averaged models typically use the shallow water equations, also known as the Saint Venant equations. De Saint-Venant (1871) derived the equations for one dimensional flow (Chaudhry, 2007). These are a set of simplified equations that describe the motion of the fluid in terms of the average depth and velocity of the flow (Horrit and Bates, 2002).

The set of equations used to describe two-dimensional flow consists of a continuity equation and two horizontal depth-averaged momentum equations. These equations are typically obtained by applying conservation laws to a vertical column of fluid (Daubert and Graffe, 1967; Van Rijn, 1990), with the assumption that the vertical distributions of the u and v velocities are uniform and that vertical acceleration is insignificant, resulting in a hydrostatic pressure distribution. However, the complete depth-averaged equations can also be derived without these assumptions by integrating the Reynolds equations over the flow depth (Steffler and Jin, 1993; Weiyan, 1992) and then applying these assumptions to simplify the equations to the Saint Venant equations. The depth-averaged equations are generally hyperbolic in nature due to the

small horizontal turbulent stress gradients (Caballeria et al., 2002). For subcritical flow, one characteristic enters the domain through both the upstream and downstream boundaries, so one boundary condition is needed at each boundary. For supercritical flow, two characteristics enter the domain through the upstream boundary, requiring two boundary conditions at that boundary (Szymkiewicz, 1993).

Modeling techniques for open channel flow are primarily developed for the Saint Venant equations, which have similar mathematical properties to the compressible Navier-Stokes or Euler equations and are predominantly hyperbolic. Numerical techniques developed for compressible flow equations have been successfully applied to the depth-averaged equations as well. The Lax Wendroff (1960) and MacCormack (1969) schemes are two classic finite difference methods that provide second-order accuracy in space and time, but may require artificial viscosity to dampen high-frequency oscillations. Upwind methods, which are based on the characteristic directions of the Saint Venant equations, split the flux into positive and negative components based on the eigenvalues that represent the characteristics of the hyperbolic equations. Higher-order accuracy can be achieved with second-order upwind methods based on the total variation diminishing (TVD) concept (Garcia-Navarro et al., 1992; Louked and Hanich, 1998; Wang et al., 2000). The finite element method allows for the representation of irregular geometry in modeling natural rivers and can be made upwind biased through the use of Petrov Galerkin finite element methods. The Characteristic Dissipative Galerkin (CDG) finite element method, developed by Hicks (1990) for one-dimensional open channel flow equations and extended in later studies for two-dimensional depth-averaged flow, has been found to be the best method in terms of both accuracy and stability in a wide range of test problems. The river modeling software 'River2D' (Steffler and Blackburn, 2002) which uses the CDG method, is currently in use by practitioners.

Currently, depth-averaged (DA) models are commonly used for river flow modeling rather than full 3D computational fluid dynamics (CFD) models. The classical Saint Venant equations used for one- and two-dimensional depth-averaged flow simulation in open channels are based on the assumptions of uniform velocity, hydrostatic pressure, and small channel slope (Chaudhry, 2007). However, these equations do not provide any vertical detail of the flow field and are not suitable for

rapidly varied flows with highly non-uniform velocity distributions and significantly non-hydrostatic pressure. Therefore, these equations only apply to flows with length scales much greater than the flow depth. Due to the inherent assumption of uniform velocity and hydrostatic pressure distribution in the depth-averaged model, they often do not reflect the actual flow behavior (Lai and Khan, 2018; Shahriari et al., 2020).

2.2.2. 3D modeling

A complete 3D model represents the flow fully with its three-dimensional (3D) characteristics, taking into account the variations in the flow velocity and depth at every point within the channel. Complete 3D models typically use more complex equations (i.e. the Navier-Stokes equations) to describe the motion of the fluid. Depth-averaged models are generally simpler and more computationally efficient than complete 3D models, but they may not capture the full complexity of the flow and may be less accurate in situations where the flow is strongly three-dimensional (Qin et al., 2018). Complete 3D models, on the other hand, can provide a more accurate representation of the flow. This can be particularly important in the case of a river, as the flow may be affected by the shape and slope of the riverbed, as well as any obstacles or structures present in the river (Cardenas and Zlotnik, 2003; Lien et al., 1999; Sivakumaran et al., 1983). Still, they may require more computational resources and may be more complex to implement and analyze (Fischer-Antze et al., 2001).

The Navier-Stokes equations, which consist of the continuity and three momentum equations, are the governing equations for three-dimensional isothermal flow of any fluid (Doering and Gibbon, 1995). However, numerical modeling of turbulent flow using these equations is limited by the smallest turbulence scales. Most flows of engineering importance, particularly open channel flows, are turbulent and it is practically impossible to describe such a chaotic flow using the instantaneous continuity and Navier-Stokes equations (Alfonsi, 2009). To model turbulent flow, these equations are time-averaged to derive the Reynolds-averaged Navier-Stokes (RANS) equations, which require the modeling of turbulent stresses produced by the time-averaging process. Fluid density is generally considered constant in open channel flow modeling, and special techniques are needed for pressure modeling and free surface computation.

To obtain detailed and accurate velocity, pressure, and bed stress distributions, 3D computational fluid dynamics (CFD) models based on the Reynolds-averaged Navier-Stokes (RANS) equations have been developed for open channel flow computation. 2D plane open channel flow computation can also be performed using CFD models based on the RANS equations with free surface variation. Lee et al. (2006) developed a free surface flow model that decomposes the pressure into hydrostatic and hydrodynamic components, while Stansby and Zhou (1998) used a depth-averaged continuity equation for water surface computation and a pressure correction technique for non-hydrostatic pressure computation and mass balance. Namin et al. (2001) used a kinematic free surface equation to compute free surface variation in their implicit non-hydrostatic model for 2D plane flow.

There have been many studies on the use of 3D models to simulate flow in physical models, with or without free surface variation, but there are relatively few studies on the use of these models to simulate natural rivers with complex geometries. Sinha et al. (1998) simulated the flow in a 4 km stretch of the Columbia River with complex bed topography using a mesh with 0.33 million nodes and a mesh aspect ratio of up to 20. They used the k-ε turbulence model for closure and treated the water surface boundary as a fixed lid using measured data. To increase computational efficiency, they employed fully vectorizable algorithms to invert the implicit operators. Despite these efforts, they were unable to reduce the residual by more than three orders of magnitude and had to accept a mass imbalance of 3% through each streamwise cross-section. Dargahi (2004) used the FLUENT model with a million unstructured elements to simulate the flow in a 6 km reach of the Klarälven river, including a bifurcation. He attempted to use the volume of fluid (VOF) method of Hirt and Nichols (1981) but was unable to model the free surface variation and had to model the water surface boundary as a rigid lid instead. It is common to use a coarse mesh with a high aspect ratio to discretize the domain, but this can make it difficult to use a fully coupled implicit solver that solves for all flow variables simultaneously, as it would require solving a large matrix. Instead, sequential implicit solvers that require iterative matrix solvers to invert the implicit operators are often used. This approach requires a larger number of time steps compared to a fully coupled model (Zobeyer, 2012).

For complex geometry of natural channel- often making the model development impossible commercially available CFD models are not suited (Biron et al., 2007). As

flow in a natural river usually have a much larger horizontal extent compared to the vertical depth, using a general CFD model to simulate can be very difficult (Hardy et al., 2005). Spatial resolution in all directions is usually determined by the need for about 10-20 nodes in the vertical direction (roughly 10 cm spacing), while the horizontal dimensions may span several kilometers. So the mesh used is often very coarse overall with a high aspect ratio when the domain is discretized (Nicholas, 2001; Shen and Diplas, 2008). Again the depth in natural rivers is often highly varying even at the same cross-section, which poses as another problem- since ten nodes at 10 cm spacing may be sufficient for small to moderate channel depths, but for depths as high as 50 m, the same choice of resolution would be inadequate. So it is often too difficult to resolve natural rivers in CFD model, and even impossible for complex geometry. Even when it becomes possible to setup a complete CFD model for rivers, the extremely high number of computational nodes makes the convergence rate incredibly slow and inefficient, or may not converge to a solution at all (Lane et al., 2005).

Modeling the free surface in 3D river flow is another significant challenge and there are two main options: dynamically computing the free surface or assuming a fixed (rigid) water surface. The volume of fluid (VOF) method is a robust option for the dynamic computation, but it can be computationally intensive (Ingham and Ma, 2005). Other methods may be less accurate or efficient and may require remeshing of the domain each time the water surface is updated, leading to increased computational effort even with the assumption of hydrostatic pressure. Assuming a fixed water surface using measured data can simplify the modeling process, but it may require a large number of measurements to accurately define the computational domain and is only applicable for specific discharges for which the measurements were taken. Non-hydrostatic pressure must be computed throughout the domain for mass balance using a pressure-velocity coupling technique, even if it is not significant. The pressure equations are elliptic, meaning that information travels in all directions, and the flow of information may take a long time in a natural river. A large mesh aspect ratio can cause numerical stiffness and hinder the convergence of the solution (Buelow et al., 1994; Sinha et al., 1998), making it difficult to use refined discretization, sophisticated turbulence models, higher-order upwind methods and allow for free surface variation due to computational time limitations in natural channels.

2.3. Coupled DA-RANS model used in this study

From the discussion above, the main challenges in 3D modeling become apparent, which includes computing the dynamic free surface, maintaining mass balance using a pressure-velocity coupling method with a large mesh aspect ratio, and the efficiency of iterative solvers for large computational domains. A novel approach to these problems was formulated in the coupled DA-RANS model of Zobeyer (2012). In this study, a new approach was used for modeling open channel flow that aims to address some of the challenges that have been identified in 3D modeling of natural rivers. In the coupled model, the DA part provides the water surface and DA velocity (neglecting non-uniform velocity and non-hydrostatic pressure). This basic flow field is then used as input in the RANS model, which results in a much faster convergence. Computational time for the coupled model is comparable to that of DA model, but at the same provides high accuracy of CFD model.

The distribution of water depth and depth-averaged (DA) velocity in a natural channel is usually determined by the upstream, downstream, and bed boundary conditions, and is partially influenced by non-uniform velocity and non-hydrostatic pressure. On the other hand, the vertical profiles of velocity and non-hydrostatic pressure are mainly affected by the bed profile, roughness, and local flow field. The proposed approach involves separating the depth-averaged (DA) variables from the 3D distributions, computing the DA variables using any DA model, and then using the RANS model to compute the 3D variations in velocity and non-hydrostatic pressure while keeping the DA outputs fixed. This is expected to be a faster process because the 3D variations mainly depend on the local DA flow fields and bed variations, which will remain unchanged, and are not affected by the upstream and the downstream flow conditions.

The coupled DA-RANS model consists of two parts: a depth-averaged model and a Reynolds-averaged Navier-Stokes (RANS) model. The depth-averaged model is solved to a steady state first to calculate the water surface elevation and depth-averaged velocity, ignoring the effects of non-uniform velocity (NUV) and non-hydrostatic pressure (NHP). The hydrostatic RANS (RANS-H) model is used to calculate horizontal velocity profiles and the RANS continuity equation is used to calculate vertical velocity profiles using the computed water surface as a fixed upper boundary.

The mass balance obtained in the depth-averaged computation is maintained by adding correction terms to the horizontal momentum equations. The non-hydrostatic model (RANS-NH) uses the pressure Poisson equation derived from the RANS equations to calculate NHP, assuming a zero pressure at the water surface and using the z momentum equation for the bed pressure. The zero pressure condition at the surface has a stronger influence on the pressure field than the upstream and downstream boundaries, as the depth of flow is significantly less than the horizontal dimensions, resulting in a faster solution for pressure. The zero pressure condition at the surface is expected to have a strong influence on the pressure field and will result in a faster solution. The mass balance is maintained using correction terms. The RANS horizontal momentum equations are discretized explicitly in the horizontal direction with an implicit coupling in the vertical direction. Once the NUV and NHP are obtained from the RANS model, their effects are included in the DA model to update the depth-averaged velocity and water depth. The updated depth-averaged flow field is then used to recalculate 3D flow variations using the Reynolds-averaged Navier-Stokes (RANS) model.

This couple DA-RANS model of Zobeyer (2012) resulted in excellent computation efficiency of the RANS part and, at the same time, enabled the modeling of large domains with a refined mesh. But one limitation was the use of only first-order upwind method to discretize the advective terms in the RANS model. Although the first-order upwinding scheme is highly stable in simulating advection, they are also known to suffer from excessive numerical diffusion, particularly in the case of coarse resolution of the numerical grid. One recommendation from that study was to implement higher-order discretization of the advection terms in the RANS model.

2.4. Higher-order differencing schemes for advection

In problems of fluid flow, the effects of advection play a significant role. Perfect modeling of the convection-dominated flow still remains a challenge in Computational Fluid Dynamics (CFD). A great many numerical schemes have been developed in the last few decades for better approximation of the convective terms in CFD. Although traditional low-order schemes like the first-order upwindning scheme are highly stable in simulating advection, they are also known to suffer from excessive numerical

diffusion. The accuracy of hybrid schemes is only first-order in terms of Taylor series truncation error (TSTE) as well (Qian et al., 2007). Using upwind quantities ensures that the schemes obey the transportiveness requirement very well to maintain stability, but the first-order accuracy makes them prone to numerical diffusion errors. Theoretically, grid refinement can alleviate all these problems; however, the necessary degree of refinement is often totally impracticable for engineering purposes, especially if one is attempting to model rapid unsteady three-dimensional turbulent flows.

Employing higher-order differencing can minimize these errors, which involve more neighbour points, and reduce the discretization errors by bringing in a wider influence. Schemes like the central differencing scheme, which has second-order accuracy, do not possess the transportiveness property and prove to be unstable (Versteeg and Malalasekera, 2007). Only formulations that take into account the flow direction have been observed to overcome this problem. So higher-order schemes with more accuracy and, at the same time, sensitivity to the flow direction preserving upwinding for stability are the more desirable choice in this case. Higher-order schemes are also expected to help with the efficiency of modeling. Although the computational effort required at each point on the grid is similar for refined grid, the use of higher-order methods allows for more accurate solutions to be obtained with a larger grid spacing than what is typically required for similar levels of accuracy using the first-order differencing. So their use can potentially provide significant practical benefits in terms of precision, speed and storage requirements.

Simply switching to higher-order schemes does not automatically guarantee better results, however. Numerous higher-order schemes have been developed for the discretization of convective terms with improved accuracy and less numerical diffusion, but they are prone to introducing spurious oscillations, especially when the solution includes sharp discontinuities or gradients (Tamamidis and Assanis, 1993; Hayase et al., 1992). The concept of flux limiters was developed (Harten, 1983) to overcome this problem by suppressing the wiggles in regions of sharp gradient and not affecting the accuracy of the solution elsewhere. The schemes implemented with flux limiters, thus try to combine the best features of both methods – smooth and oscillation-free solution of low-order scheme and greater accuracy and efficiency of high-order schemes. The tendency towards fluctuation is counteracted by adding an artificial

diffusion fragment or a weighting towards upstream contribution. However, such bounded or limited solutions can sometimes exhibit flattening or clipping of local maxima if steep gradient is present, which is the case for many Total variation diminishing (TVD) schemes. The TVD scheme becomes a first-order upwind scheme near local extrema. They suffer from a well-known inherent drawback that even the high-order TVD schemes degrade to first-order at local extrema and produce unphysical clipping at local extrema (Yang and Przekwas, 1992; Leonard et al., 1996). Nonetheless, many of the developed higher-order schemes have exhibited varying degrees of success in simulating the advection phenomenon. But it is very difficult to conclusively state if one scheme or the other will yield the best results since none of the methods are completely free from drawbacks. Again, the performance of the various discretization methods developed over the last many years cannot be easily compared since each of the studies used different test conditions.

2.4.1. Schemes used in the present study

The present study attempted to bring together thirty such higher-order schemes and assess their performance in terms of accuracy and diffusivity, against a common standard of comparison. All the schemes were subjected to identical numerical testing conditions and thereby the solutions of the different schemes could all be directly compared. Flux limiters of different forms were imposed on many of these schemes.

The thirty schemes chosen for the current study include QUICK and QUICKEST schemes of Leonard (1979). Quadratic upstream interpolation for convective kinetics (QUICK) scheme uses a three-point upstream-weighted quadratic interpolation for face values, where the cell face value is obtained from a quadratic function passing through two bracketing nodes and one additional node on the upstream side. Again, Leonard proposed the QUICK formulas mainly for steady or quasi-steady flow in which the Peclet number is large only in one direction. The same study presented the corresponding unsteady-flow formulas as the QUICKEST (QUICK with Estimated Streaming Terms) scheme. These methods have properties of high accuracy (third-order spatial truncation error and third-order in time for the QUICKEST method). Under highly convective conditions, however, the QUICK scheme has been observed

to introduce unphysical overshoots and oscillatory results in regions where the convected variables experience sharp changes in gradients or discontinuities. Flux limiters need to be employed in such cases to achieve oscillation-free higher-order accuracy. Two other versions of QUICK with limiters were also tested in the presented study along with the original schemes of Leonard. One of these were with steady limiter (Versteeg and Malalasekera, 2007), and another with CFL-WACEB limiter (Kuan and Lin, 2000).

MUSCL is another notable scheme used in this study, which stands for Monotonic Upstream-centered Scheme for Conservation Laws. It was developed by van Leer (1979) and is a finite volume method that can provide highly accurate numerical solutions for a given system, even in cases where the solutions exhibit shocks, discontinuities, or large gradients. Superbee-CFL (Kemm, 2011; Roe, 1985) is another bounded solution scheme, that considers the courant number effect in the more restrictive TVD region, so that the clipping phenomena is somewhat minimized.

Conservative explicit advection schemes of arbitrarily high order has also been composed from 'Transient Iinterpolation Modeling' (TIM), where the accuracy (in both space and time) of the approximate numerical method is determined solely by spatial interpolation at the previous timestep. 2nd, 4th and 5th order upwinding methods included here are derived from upwinding TIM found in Leonard (1991), that can be continued up to arbitrarily high order, based on binomial coefficients or Pascal's triangle. The 3rd order TIM is similar to the QUICKEST scheme. In the same paper, Leonard also introduced the 'Universal Limiter' which is claimed in the study to suppress oscillations without corrupting the expected accuracy of the higher-order method as this system of limiter also considers the effect of courant number in the TVD constraints. The 2nd, 4th and 5th order upwinding methods are also tested in the present study in conjunction with Leonard's universal limiter. This approach was termed as the ULTIMATE conservative difference scheme in the study, which consists of using the universal limiter for transient interpolation modeling of the advective transport equations.

The Arora-Roe scheme (Arora and Roe, 1997) resembles the QUICKEST scheme when used with a universal limiter. Another scheme developed by Leonard and

Niknafs (1991) is the Adaptive stencil expansion, in which universally limited QUICKEST scheme (3rd order) is used as a base method that automatically switches to a higher resolution (7th or 9th order TIM) in small, isolated regions of high curvature or high gradient. This method can be used in conjunction with a discriminator, that can identify well-defined narrow local maxima and switches off the limiter there, but elsewhere it keeps the limiter activated to suppress spurious oscillations. Since this method uses very high orders of upwinding, an alternative is also tried in this paper by combining the discriminator with the QUICKEST scheme. Other schemes included in this study are: WENO-5, WENO-5 with limiter and ENO-2 (Salih and Ghosh Moulic, 2009), MIN-MOD (Roe, 1985), SPUDS (Leonard, 1995), SMART (Lin and Lin, 1997), Hyperbee, Superpower and van Leer with sharpener (Kemm, 2011), Euler Quick (Leonard, 1988), PHIB and WSN (Qian et al., 2007), TCDF (Zhang et al., 2015) and UMIST (Lien and Leschziner, 1994).

CHAPTER 3

METHODOLOGY

3.1. Introduction

This chapter details the various approaches used in this study to evaluate the performance of the higher-order schemes in simulating advection terms. The evaluation was done in multiple stages of varying intricacies. The methods were first tested for pure advection scenarios, which was followed by their applicability and performance analysis in 2D and 3D open channel flow models respectively.

3.2. Comparative evaluation for pure advection

To get an initial idea about the accuracy and stability of the various schemes, they were first applied to simplified cases of pure advection. The schemes were analysed in terms of solving unsteady advection with constant velocity for various distributions of tracer concentration both for 1D and 2D.

3.2.1. 1D Advection model

For the one-dimensional case, the equation to be modeled can be written as

$$\frac{\partial C}{\partial t} + u\frac{\partial C}{\partial x} = 0 \tag{3.1}$$

Here, C represents tracer concentration at a particular time and at a particular location. In governing equations of open channel flows, this variable C is usually replaced with velocity or discharge variables. Pure advection equation assumes that there is no diffusion, and since the velocity field is constant at all points in this case, the concentration distribution should not alter in shape or peak. The analytical solution of the above equation can simply be expressed as

$$C(x,t) = C_0(x - ut) \tag{3.2}$$

The analytical solution shows that a given initial concentration will travel with a velocity u without any decay or diffusion. The shape and the peak will remain same as the initial distribution.

For the numerical solution of advection, the finite difference approach substitutes the partial differential equations with finite difference equations in terms of spatial and temporal grid coordinates. A sketch of the grid coordinate system of FDM is illustrated in figure 3.1. Again, many of the schemes, such as QUICK, MUSCl etc. used in this study, were developed originally based on the finite volume method. Since for regular grids (i.e., the same value of Δx throughout the grid), finite volume and finite difference methods give the same results (Botte et al., 2000), the definition sketch of FVM shown in figure 3.2 is used in this study to resolve the advection terms.

The time derivative in equation 3.1 is conventionally discretized using the forward difference scheme, mainly due to it being an explicit scheme and the simplicity in its implementation (Hindmarsh et al., 1984). The equation can be discretized to take on the following form, using forward difference in the temporal discretization

$$C_i^{n+1} = C_i^n - u.\Delta t\frac{dC}{dx} \tag{3.3}$$

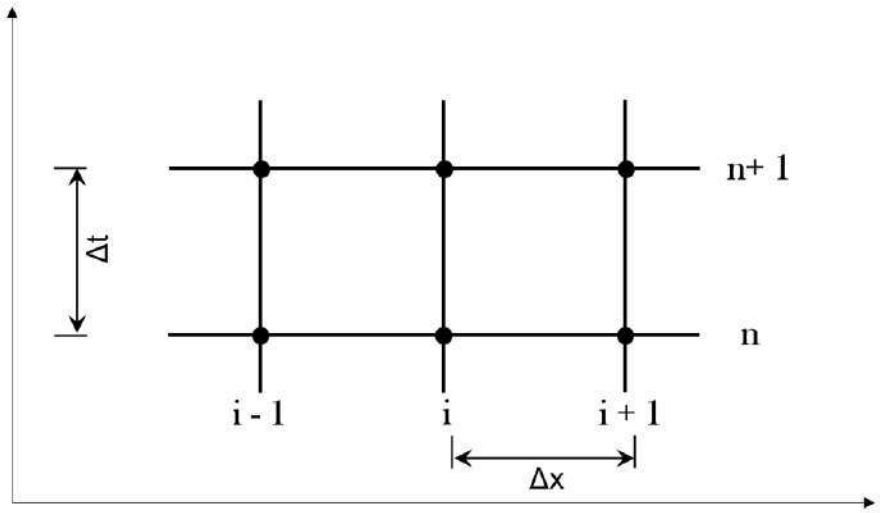

Figure 3.1 Finite difference method grid

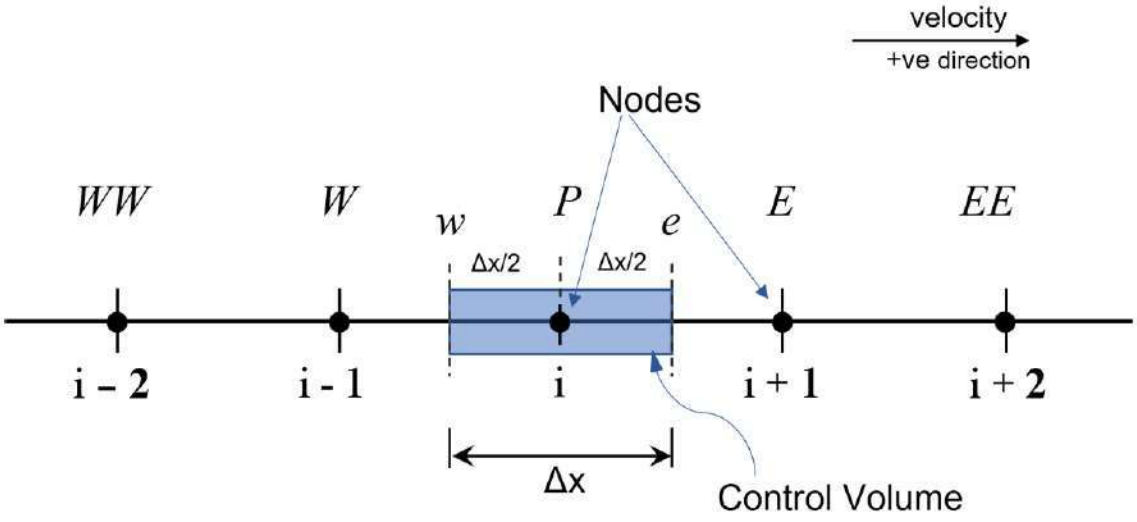

Figure 3.2 Definition sketch of grid used in the present study

3.2.2. Programmes developed for higher-order numerical discretization

Pure advection is a hyperbolic type of partial differential equation, and therefore for a stable solution, it requires some form of upwinding scheme. Corresponding to the grid shown in figure 3.2, the advective term at node i can be expressed as

$$\frac{d\varphi_i}{dx} = \frac{\varphi_e - \varphi_w}{\Delta x} \tag{3.4}$$

Here, φ is a general flow variable (i.e., it can be any discharge or velocity component, etc.). In this particular case $\varphi = C$, tracer concentration, and φ_w, φ_e corresponds to upstream and downstream face values of the control volume respectively. The discretization is shown for positive velocity direction from left to right. If the velocity direction reverses, the face values would change accordingly. Matlab® (R2021b) programmes were developed for thirty high-order schemes that evaluated the cell face values in distinct ways and thus approximated the advective derivative in equation 3.4. Each scheme varies in regards to how many nodes upstream or downstream it takes into consideration when evaluating the cell face values, and the weightage assigned to the nodes considered.

For example, in the first-order upwind method, the cell faces are assigned the value of a single node just upstream of the face. No nodes from further upstream or downstream play any role in the first-order upwind discretization. So for positive flow direction, cell faces are estimated as $\varphi_w = \varphi_{i-1}$ and $\varphi_e = \varphi_i$. If the flow direction changes to the opposite direction (-ve velocity), then the face values will be changed as $\varphi_w = \varphi_i$ and $\varphi_e = \varphi_{i+1}$. Again, a higher-order scheme like QUICK uses a three-point upstream-weighted quadratic interpolation for cell face values: two bracketing nodes (on each side of the face) and a node on the upstream side. For the QUICK scheme and +ve velocity direction, φ at the left cell face is given by $\varphi_w = \frac{6}{8}\varphi_{i-1} + \frac{3}{8}\varphi_i - \frac{1}{8}\varphi_{i-2}$. Other higher-order methods may use more points downstream and upstream to get a more accurate approximation. The process of how the left (or upwind) cell face value, φ_w was expressed using different schemes used in this study, is shown in table 3.1 along with references of relevant literature. In the same way φ_e was estimated with a similar set of nodes. All the schemes were written using Matlab® (R2021b), and the code had a built-in provision to take into account the flow direction and select the correct set of nodes for cell face approximation.

Table 3.1 First-order and higher-order scheme programmes developed in Matlab®

Scheme Name	**Cell Face value** (left face, $\boldsymbol{\varphi_w}$ for positive velocity)	**Reference**
FOU	$\varphi_w = \varphi_{i-1}$	Versteeg and Malalasekera (2007)
QUICK	$r = (\varphi_{i-1} - \varphi_{i-2}) / (\varphi_i - \varphi_{i-1})$ $\Psi = 1/4*(3+r)$ $\varphi_w = \varphi_{i-1} + 0.5* \Psi *(\varphi_i - \varphi_{i-1})$	Leonard (1979)
QUICK-SL	$r = (\varphi_{i-1} - \varphi_{i-2}) / (\varphi_i - \varphi_{i-1})$ $\Psi = 1/4*(3+r)$ $\Psi = \max(0, \min(2, \Psi, 2r))$ $\varphi_w = \varphi_{i-1} + 0.5* \Psi *(\varphi_i - \varphi_{i-1})$	Versteeg and Malalasekera (2007)
QUICK-L	$r = (\varphi_{i-1} - \varphi_{i-2}) / (\varphi_i - \varphi_{i-1})$ $\Psi = 1/4*(3+r)$ $\Psi = \max(0, \min(2/(1 - cr), \Psi, 2*r/cr))$ $\varphi_w = \varphi_{i-1} + (1 - cr)*0.5* \Psi *(\varphi_i - \varphi_{i-1})$	Kuan and Lin (2000)

QUICKEST	$\varphi_w^{(2)} = 0.5*((\varphi_i + \varphi_{i-1}) - cr*(\varphi_i - \varphi_{i-1}))$ $\varphi_w = \varphi_w^{(3)} = \varphi_w^{(2)} - (1- cr^2)/6*(\varphi_i - 2\varphi_{i-1} + \varphi_{i-2})$	Leonard (1979) Leonard (1988)

QUICKEST-D	$\varphi_w^{(2)} = 0.5*((\varphi_i + \varphi_{i-1}) - cr*(\varphi_i - \varphi_{i-1}))$
	$\varphi_w = \varphi_w^{(3)} = \varphi_w^{(2)} - (1- cr^2)/6*(\varphi_i - 2\varphi_{i-1} + \varphi_{i-2})$
	$del = (\varphi_i - \varphi_{i-2})$; $adel = abs(del)$; $acurv = abs(\varphi_i - 2*\varphi_{i-1} + \varphi_{i-2})$
	if acurv>0.6*adel → limiter will activate
	if acurv ≥ adel → $\varphi_w = \varphi_{i-1}$
	else $\varphi_{ref} = \varphi_{i-2} + (\varphi_{i-1} - \varphi_{i-2})/cr$
	if del > 0 → $\varphi_w = \min(\max(\varphi_w, \varphi_{i-1}), \varphi_{ref}, \varphi_i)$
	if del ≤ 0 → $\varphi_w = \max(\min(\varphi_w, \varphi_{i-1}), \varphi_{ref}, \varphi_i)$
	Discriminator condition (limiter will not activate):
	$D_1 = (\varphi_{i-3} - \varphi_{i-4}), D_2 = (\varphi_{i-2} - \varphi_{i-3}), \ldots\ldots, D_6 = (\varphi_{i+2} - \varphi_{i+1})$
	Condition for Maxima
	if (D1>0 & D2>0 & D3<0 & D4<0 & abs(D2)<abs(D1)& abs(D3)<abs(D4)) or (D2>0 & D3>0 & D4<0 & D5<0 & abs(D3)<abs(D2)& abs(D4)<abs(D5)) or (D3>0 & D4>0 & D5<0 & D6<0& abs(D4)<abs(D3)& abs(D5)<abs(D6))
	Condition for Minima
	if (D1<0 & D2<0 & D3>0 & D4>0 & abs(D2)<abs(D1)& abs(D3)<abs(D4)) or (D2<0 & D3<0 & D4>0 & D5>0 & abs(D3)<abs(D2)& abs(D4)<abs(D5)) or (D3<0 & D4<0 & D5>0 & D6>0& abs(D4)<abs(D3)& abs(D5)<abs(D6))
		Leonard (1979)
		Leonard and Niknafs (1991)

MUSCL	$r = (\varphi_{i-1} - \varphi_{i-2}) / (\varphi_i - \varphi_{i-1})$ $\Psi = 1/2*(1+r)$ $\Psi = \max(0, \min(2/(1- cr), \Psi, 2*r/cr))$ $\varphi_w = \varphi_{i-1} + (1 - cr)*0.5* \Psi *(\varphi_i - \varphi_{i-1})$	Van Leer (1977) Waterson and Deconinck (2007)
Superbee	$r = (\varphi_{i-1} - \varphi_{i-2}) / (\varphi_i - \varphi_{i-1})$ $\Psi = \max(1,r)$ $\Psi = \max(0, \min(2/(1- cr), \Psi, 2*r/cr))$ $\varphi_w = \varphi_{i-1} + (1 - cr)*0.5* \Psi *(\varphi_i - \varphi_{i-1})$	Roe (1985) Kemm (2011)
Arora-Roe	$r = (\varphi_{i-1} - \varphi_{i-2}) / (\varphi_i - \varphi_{i-1})$ $\Psi = 1 - (1+ cr)/3*(1-r)$ $\Psi = \max(0, \min(2/(1- cr), \Psi, 2*r/cr))$ $\varphi_w = \varphi_{i-1} + (1 - cr)*0.5* \Psi *(\varphi_i - \varphi_{i-1})$	Arora and Roe (1997)
2ndOU	$\varphi_w^{(2)} = 0.5*((\varphi_i + \varphi_{i-1}) - cr*(\varphi_i - \varphi_{i-1}))$ $\varphi_w = \varphi_w^{(2U)} = \varphi_w^{(2)} - (1-abs(cr))/2(\varphi_i - 2\varphi_{i-1} + \varphi_{i-2})$	Leonard (1988)
2ndOU-L	$\varphi_w^{(2)} = 0.5*((\varphi_i + \varphi_{i-1}) - cr*(\varphi_i - \varphi_{i-1}))$ $\varphi_w = \varphi_w^{(2U)} = \varphi_w^{(2)} - (1-abs(cr))/2*(\varphi_i - 2\varphi_{i-1} + \varphi_{i-2})$ $del = (\varphi_i - \varphi_{i-2})$; $adel = abs(del)$; $acurv = abs(\varphi_i - 2\varphi_{i-1} + \varphi_{i-2})$ limiter condition: if acurv ≥ adel → $\varphi_w = \varphi_{i-1}$ else $\varphi_{ref} = \varphi_{i-2} + (\varphi_{i-1} - \varphi_{i-2})/cr$ if del > 0 → $\varphi_w = \min(\min(\max(\varphi_w, \varphi_{i-1}), \varphi_{ref}), \varphi_i)$ if del ≤ 0 → $\varphi_w = \max(\max(\min(\varphi_w, \varphi_{i-1}), \varphi_{ref}), \varphi_i)$	Leonard (1988)
4thOU	$\varphi_w^{(2)} = 0.5*((\varphi_i + \varphi_{i-1}) - cr*(\varphi_i - \varphi_{i-1}))$ $\varphi_w = \varphi_w^{(4)} = \varphi_w^{(2)} - (1-cr^2)/12*(\varphi_{i+1} - \varphi_i - \varphi_{i-1} + \varphi_{i-2} - cr/2*(\varphi_{i+1} - 3\varphi_i + 3\varphi_{i-1} - \varphi_{i-2}))$	Leonard (1988)

4thOU-L	$\varphi_w^{(2)} = 0.5*((\varphi_i + \varphi_{i-1}) - cr*(\varphi_i - \varphi_{i-1}))$ $\varphi_w = \varphi_w^{(4)} = \varphi_w^{(2)} - (1-cr^2)/12*(\varphi_{i+1} - \varphi_i - \varphi_{i-1} + \varphi_{i-2} - cr/2*(\varphi_{i+1} - 3\varphi_i + 3\varphi_{i-1} - \varphi_{i-2}))$ del = $(\varphi_i - \varphi_{i-2})$; adel = abs(del); acurv= abs $(\varphi_i - 2\varphi_{i-1} + \varphi_{i-2})$ if acurv>0.6*adel → limiter will activate if acurv ≥ adel → $\varphi_w = \varphi_{i-1}$ else $\varphi_{ref} = \varphi_{i-2} + (\varphi_{i-1} - \varphi_{i-2})/cr$ if del > 0 → φ_w = min (min(max(φ_w , φ_{i-1}), φ_{ref}), φ_i) if del ≤ 0 → φ_w = max (max(min(φ_w , φ_{i-1}), φ_{ref}), φ_i)	Leonard (1988)
5thOU	$\varphi_w^{(2)} = 0.5*((\varphi_i + \varphi_{i-1}) - cr*(\varphi_i - \varphi_{i-1}))$ $\varphi_w^{(4)} = \varphi_w^{(2)} - (1-cr^2)/12*(\varphi_{i+1} - \varphi_i - \varphi_{i-1} + \varphi_{i-2} - cr/2*(\varphi_{i+1} - 3\varphi_i + 3\varphi_{i-1} - \varphi_{i-2}))$ $\varphi_w = \varphi_w^{(5)} = \varphi_w^{(4)} + (1-cr^2)*(4 - cr^2)/120*(\varphi_{i+1} - 4\varphi_i + 6\varphi_{i-1} - 4\varphi_{i-2} + \varphi_{i-3})$	Leonard (1988)
5thOU-L	$\varphi_w^{(2)} = 0.5*((\varphi_i + \varphi_{i-1}) - cr*(\varphi_i - \varphi_{i-1}))$ $\varphi_w^{(4)} = \varphi_w^{(2)} - (1-cr^2)/12*(\varphi_{i+1} - \varphi_i - \varphi_{i-1} + \varphi_{i-2} - cr/2*(\varphi_{i+1} - 3\varphi_i + 3\varphi_{i-1} - \varphi_{i-2}))$ $\varphi_w = \varphi_w^{(5)} = \varphi_w^{(4)} + (1-cr^2)*(4 - cr^2)/120*(\varphi_{i+1} - 4\varphi_i + 6\varphi_{i-1} - 4\varphi_{i-2} + \varphi_{i-3})$ del = $(\varphi_i - \varphi_{i-2})$; adel = abs(del); acurv= abs $(\varphi_i - 2\varphi_{i-1} + \varphi_{i-2})$ if acurv>0.6*adel → limiter will activate if acurv ≥ adel → $\varphi_w = \varphi_{i-1}$ else $\varphi_{ref} = \varphi_{i-2} + (\varphi_{i-1} - \varphi_{i-2})/cr$ if del > 0 → φ_w = min (min(max(φ_w , φ_{i-1}), φ_{ref}), φ_i) if del ≤ 0 → φ_w = max (max(min(φ_w , φ_{i-1}), φ_{ref}), φ_i)	Leonard (1988)
ENO	$\varphi_w = \varphi_{i-1} + \Delta x/2*\text{minmod}((\varphi_{i+1} - 2\varphi_i + \varphi_{i-1})/\Delta x^2, (\varphi_i - 2\varphi_{i-1} + \varphi_{i-2})/\Delta x^2)$ if a*b >0, minmod(a, b) = S(a) * min(|a|, |b|) else minmod(a, b) = 0 S(a) = -1 if a<0 = 1 if a>0 = 0 if a=0	Salih and Ghosh Moulic (2009)
WENO	$\varphi_1 = 1/3*\varphi_{i-3} - 7/6*\varphi_{i-2} + 11/6*\varphi_{i-1}$; $\varphi_2 = -1/6*\varphi_{i-2} + 5/6*\varphi_{i-1} + 1/3*\varphi_i$; $\varphi_3 = 1/3*\varphi_{i-1} + 5/6*\varphi_i - 1/6*\varphi_{i+1}$; $S_1 = 13/12*(\varphi_{i-3} - 2\varphi_{i-2} + \varphi_{i-1})^2 + 1/4*(\varphi_{i-3} - 4\varphi_{i-2} + 3\varphi_{i-1})^2$; $\alpha_1 = 0.1/(S_1+\epsilon)^2$ $S_2 = 13/12*(\varphi_{i-2} - 2\varphi_{i-1} + \varphi_i)^2 + 1/4*(\varphi_{i-2} - \varphi_i)^2$; $\alpha_2 = 0.6/(S_2+\epsilon)^2$ $S_3 = 13/12*(\varphi_{i-1} - 2\varphi_i + \varphi_{i+1})^2 + 1/4*(3\varphi_{i-1} - 4\varphi_i + \varphi_{i+1})^2$; $\alpha_3 = 0.3/(S_3+\epsilon)^2$ $\epsilon = 10^{-6}$; $\omega_i = \alpha_i / \Sigma\alpha$ $\varphi_w = \alpha_1*\varphi_1 + \alpha_2*\varphi_2 + \alpha_3*\varphi_3$	Salih and Ghosh Moulic (2009)
WENO-L	$\varphi_1 = 1/3*\varphi_{i-3} - 7/6*\varphi_{i-2} + 11/6*\varphi_{i-1}$; $\varphi_2 = -1/6*\varphi_{i-2} + 5/6*\varphi_{i-1} + 1/3*\varphi_i$; $\varphi_3 = 1/3*\varphi_{i-1} + 5/6*\varphi_i - 1/6*\varphi_{i+1}$; $S_1 = 13/12*(\varphi_{i-3} - 2\varphi_{i-2} + \varphi_{i-1})^2 + 1/4*(\varphi_{i-3} - 4\varphi_{i-2} + 3\varphi_{i-1})^2$; $\alpha_1 = 0.1/(S_1+\epsilon)^2$ $S_2 = 13/12*(\varphi_{i-2} - 2\varphi_{i-1} + \varphi_i)^2 + 1/4*(\varphi_{i-2} - \varphi_i)^2$; $\alpha_2 = 0.6/(S_2+\epsilon)^2$ $S_3 = 13/12*(\varphi_{i-1} - 2\varphi_i + \varphi_{i+1})^2 + 1/4*(3\varphi_{i-1} - 4\varphi_i + \varphi_{i+1})^2$; $\alpha_3 = 0.3/(S_3+\epsilon)^2$ $\epsilon = 10^{-6}$; $\omega_i = \alpha_i / \Sigma\alpha$ $\varphi_w = \alpha_1*\varphi_1 + \alpha_2*\varphi_2 + \alpha_3*\varphi_3$	Salih and Ghosh Moulic (2009) Leonard (1988)

	del = (φ_i - φ_{i-2}); adel = abs(del); acurv= abs (φ_i - 2φ_{i-1} + φ_{i-2}) if acurv>0.6*adel → limiter will activate if acurv ≥ adel → $\varphi_w = \varphi_{i-1}$ else $\varphi_{ref} = \varphi_{i-2} + (\varphi_{i-1} - \varphi_{i-2})/cr$ if del > 0 → φ_w = min (min(max(φ_w , φ_{i-1}), φ_{ref}), φ_i) if del ≤ 0 → φ_w = max (max(min(φ_w , φ_{i-1}), φ_{ref}), φ_i)	
MIN-MOD	$r = (\varphi_{i-1} - \varphi_{i-2}) / (\varphi_i - \varphi_{i-1})$ Ψ = max(0, min(r,1)) $\varphi_w = \varphi_{i-1} + 0.5 * \Psi * (\varphi_i - \varphi_{i-1})$	Roe (1985)
SPUDS	$r = (\varphi_{i-1} - \varphi_{i-2}) / (\varphi_i - \varphi_{i-1})$ $\Psi = 1/3*(2+r)$; $\varphi_w = \varphi_{i-1} + 0.5 * \Psi * (\varphi_i - \varphi_{i-1})$	Leonard (1995)
Superpower	$r = (\varphi_{i-1} - \varphi_{i-2}) / (\varphi_i - \varphi_{i-1})$ p(r) = 2/cr*2*(1- (1+cr)/3) → if r ≤ 1 = 2/(1-cr)*2*(1+cr)/3 → if r > 1 Ψ = max(0, (1- (1+cr)/3*(1-r))*(1- abs((1-abs(r))/(1+abs(r)))^{pr})) $\varphi_w = \varphi_{i-1} + 0.5*(1-cr)* \Psi * (\varphi_i - \varphi_{i-1})$	Kemm (2011)
Van Leer	$r = (\varphi_{i-1} - \varphi_{i-2}) / (\varphi_i - \varphi_{i-1})$ Ψ = max(0, (1+r)/2*(1-abs((1-abs(r))/(1+abs(r)))^2)) $\varphi_w = \varphi_{i-1} + 0.5 * \Psi * (\varphi_i - \varphi_{i-1})$	Kemm (2011)
SMART	$r = (\varphi_{i-1} - \varphi_{i-2}) / (\varphi_i - \varphi_{i-2})$ φ_l = r → if, r ∉ [0, 1] ; φ_l = 2r → if, r ∈ [0, 3/10] φ_l = 3/4*r + 3/8 → if, r ∈ [3/10, 5/6] ; φ_l = 1 → if, r ∈ [5/6, 1] $\varphi_w = \varphi_l * (\varphi_i - \varphi_{i-2}) + \varphi_{i-2}$	Lin and Lin (1997)
Euler QUICK	if abs(φ_i - φ_{i-2})< 10^{-5} or abs(φ_i -2φ_{i-1}+ φ_{i-2}) ≤0.3*abs(φ_i - φ_{i-2}) → φ_w = 3/8*φ_i + 6/8* φ_{i-1} -1/8* φ_{i-2}; else → r=(φ_{i-1}- φ_{i-2})/(φ_i - φ_{i-2}) φ_w = 3/8*φ_i +6/8*φ_{i-1} -1/8*φ_{i-2} → if, r ∉ [-1, 1.5] or r ∈ [0.35, 0.65] φ_w = 3/8*r *(φ_i - φ_{i-2})+ φ_{i-2} → if, r ∈ [-1, 0] φ_w = r *(φ_i - φ_{i-2})+ φ_{i-2} → if, r ∈ [1, 1.5] $\varphi_w = \varphi_l * (\varphi_i - \varphi_{i-2}) + \varphi_{i-2}$ → if, r ∈ [0, 0.35] or r ∈ [0.65, 1] $\varphi_l = ((r*(1-r)^3)^{0.5} - r^2)/(1-2r)$	Leonard (1988)
WSN	$\varphi_L = \varphi_{i-1}$; φ_H = = 3/8*φ_i +6/8*φ_{i-1} -1/8*φ_{i-2} α = 0 → if γ < 0 ; α = γ/0.2 → if 0≤ γ ≤0.2 ; α = 1 → if 0.2 < γ <0.8 ; α = (1-γ)/0.2 → if 0.8≤ γ ≤1 ; α = 0 → if 1 < γ $\gamma = (\varphi_{i-1} - \min(\varphi_{i-2}, \varphi_i)) / (\max(\varphi_{i-2}, \varphi_i) - \min(\varphi_{i-2}, \varphi_i))$ $\varphi_w = (1 - \alpha)\ \varphi_L + \alpha\ \varphi_H$	Qian et al. (2007)
Hyperbee	$r = (\varphi_{i-1} - \varphi_{i-2}) / (\varphi_i - \varphi_{i-1})$ Ψ = 0 → if r ≤ 0 = 1 → if r = 1 = max(0, min(2*r/cr, min(2/(1-cr), (2*r/(cr*(1-cr)))*((cr*(r-1) + (1-r^{cr}))/((r-1)^2))))) $\varphi_w = \varphi_{i-1} + 0.5 * \Psi * (1-cr) * (\varphi_i - \varphi_{i-1})$	Kemm (2011)
PHIB	$\varphi_L = \varphi_{i-1}$; φ_H = = 3/8*φ_i +6/8*φ_{i-1} -1/8*φ_{i-2} α = 0 → if φ_{i-1} < 0 = 1 → if 0 ≤ φ_{i-1} ≤ 1 = 0 → if 1 < φ_{i-1} $\varphi_w = (1 - \alpha)\ \varphi_L + \alpha\ \varphi_H$	Qian et al. (2007)

Adaptive	$\varphi_w^{(2)} = 0.5*((\varphi_i + \varphi_{i-1}) - cr*(\varphi_i - \varphi_{i-1}))$ $\varphi_w = \varphi_w^{(3)} = \varphi_w^{(2)} - (1- cr^2)/6*(\varphi_i - 2\varphi_{i-1} + \varphi_{i-2})$ [QUICKEST] In small localized large gradient or large-curvature regions: curvav=0.5 * abs($\varphi_{i+1} - \varphi_i - \varphi_{i-1} + \varphi_{i-2}$) grad=abs($\varphi_i - \varphi_{i-1}$) for 0.025<curvav<0.15 → switch to 7thOU $\varphi_w^{(4)} = \varphi_w^{(2)} - (1-cr^2)/(2*3!)*(\varphi_{i+1} - \varphi_i - \varphi_{i-1} + \varphi_{i-2}$ $-cr/2*(\varphi_{i+1} -3\varphi_i+3\varphi_{i-1} - \varphi_{i-2}))$ $\varphi_w^{(6)} = \varphi_w^{(4)} + (1-cr^2)*(4-cr^2)/(2*5!)*(\varphi_{i+2} -3\varphi_{i+1} +2\varphi_i +2\varphi_{i-1}$ $-3\varphi_{i-2} + \varphi_{i-3} -cr/3*(\varphi_{i+2} -5\varphi_{i+1} +10\varphi_i -10\varphi_{i-1} +5\varphi_{i-2} - \varphi_{i-3}))$ $\varphi_w = \varphi_w^{(7)} = \varphi_w^{(6)} - (1-cr^2)*(4-cr^2)*(9-cr^2)/7!*(\varphi_{i+2} -6\varphi_{i+1} +15\varphi_i$ $-20\varphi_{i-1} +15\varphi_{i-2} -6\varphi_{i-3} + \varphi_{i-4})$ for curvav>0.15 or grad>0.2 → switch to 9thOU $\varphi_w^{(8)} = \varphi_w^{(6)} - (1-cr^2)*(4-cr^2)*(9-cr^2)/(2*7!)*(\varphi_{i+3} -5\varphi_{i+2} +9\varphi_{i+1} -5\varphi_i$ $-5\varphi_{i-1} +9\varphi_{i-2} -5\varphi_{i-3} + \varphi_{i-4} -cr/4*(\varphi_{i+3} -7\varphi_{i+2}$ $+21\varphi_{i+1} -35\varphi_i +35\varphi_{i-1} -21\varphi_{i-2} +7\varphi_{i-3} - \varphi_{i-4}))$ $\varphi_w = \varphi_w^{(9)} = \varphi_w^{(8)} + (1-cr^2)*(4-cr^2)*(9-cr^2)*(16-cr^2)/9!*(\varphi_{i+3} -8\varphi_{i+2}$ $+28\varphi_{i+1} -56\varphi_i +70\varphi_{i-1} -56\varphi_{i-2} +28\varphi_{i-3} -8\varphi_{i-4} + \varphi_{i-5})$ del = ($\varphi_i - \varphi_{i-2}$); adel = abs(del); acurv= abs ($\varphi_i - 2\varphi_{i-1} + \varphi_{i-2}$) if acurv ≥ adel → $\varphi_w = \varphi_{i-1}$ else $\varphi_{ref} = \varphi_{i-2} + (\varphi_{i-1} - \varphi_{i-2})/cr$ if del > 0 → φ_w = min (min(max(φ_w, φ_{i-1}), φ_{ref}), φ_i) if del ≤ 0 → φ_w = max (max(min(φ_w, φ_{i-1}), φ_{ref}), φ_i)	Leonard (1988) Leonard and Niknafs (1991)

Adaptive-D	$\varphi_w^{(2)} = 0.5*((\varphi_i + \varphi_{i-1}) - cr*(\varphi_i - \varphi_{i-1}))$
	$\varphi_w = \varphi_w^{(3)} = \varphi_w^{(2)} - (1- cr^2)/6*(\varphi_i - 2\varphi_{i-1} + \varphi_{i-2})$ [QUICKEST]
	In small localized large gradient or large-curvature regions:
	curvav=0.5 * abs($\varphi_{i+1} - \varphi_i - \varphi_{i-1} + \varphi_{i-2}$)
	grad=abs($\varphi_i - \varphi_{i-1}$)
	for 0.025<curvav<0.15 → switch to 7thOU
	$\varphi_w^{(4)} = \varphi_w^{(2)} - (1-cr^2)/(2*3!)*(\varphi_{i+1} - \varphi_i - \varphi_{i-1} + \varphi_{i-2}$
	$-cr/2*(\varphi_{i+1} -3\varphi_i+3\varphi_{i-1} - \varphi_{i-2}))$
	$\varphi_w^{(6)} = \varphi_w^{(4)} + (1-cr^2)*(4-cr^2)/(2*5!)*(\varphi_{i+2} -3\varphi_{i+1} +2\varphi_i +2\varphi_{i-1}$
	$-3\varphi_{i-2} + \varphi_{i-3} -cr/3*(\varphi_{i+2} -5\varphi_{i+1} +10\varphi_i -10\varphi_{i-1} +5\varphi_{i-2} - \varphi_{i-3}))$
	$\varphi_w = \varphi_w^{(7)} = \varphi_w^{(6)} - (1-cr^2)*(4-cr^2)*(9-cr^2)/7!*(\varphi_{i+2} -6\varphi_{i+1} +15\varphi_i$
	$-20\varphi_{i-1} +15\varphi_{i-2} -6\varphi_{i-3} + \varphi_{i-4})$
	for curvav>0.15 or grad>0.2 → switch to 9thOU
	$\varphi_w^{(8)} = \varphi_w^{(6)} - (1-cr^2)*(4-cr^2)*(9-cr^2)/(2*7!)*(\varphi_{i+3} -5\varphi_{i+2} +9\varphi_{i+1} -5\varphi_i$
	$-5\varphi_{i-1} +9\varphi_{i-2} -5\varphi_{i-3} + \varphi_{i-4} -cr/4*(\varphi_{i+3} -7\varphi_{i+2}$
	$+21\varphi_{i+1} -35\varphi_i +35\varphi_{i-1} -21\varphi_{i-2} +7\varphi_{i-3} - \varphi_{i-4}))$
	$\varphi_w = \varphi_w^{(9)} = \varphi_w^{(8)} + (1-cr^2)*(4-cr^2)*(9-cr^2)*(16-cr^2)/9!*(\varphi_{i+3} -8\varphi_{i+2}$
	$+28\varphi_{i+1} -56\varphi_i +70\varphi_{i-1} -56\varphi_{i-2} +28\varphi_{i-3} -8\varphi_{i-4} + \varphi_{i-5})$
	del = ($\varphi_i - \varphi_{i-2}$); adel = abs(del); acurv= abs ($\varphi_i - 2\varphi_{i-1} + \varphi_{i-2}$)
	if acurv ≥ adel → $\varphi_w = \varphi_{i-1}$
	else $\varphi_{ref} = \varphi_{i-2} + (\varphi_{i-1} - \varphi_{i-2})/cr$
	if del > 0 → φ_w = min (max(φ_w, φ_{i-1}), φ_{ref}, φ_i)
	if del ≤ 0 → φ_w = max (min(φ_w, φ_{i-1}), φ_{ref}, φ_i)
	Discriminator condition (limiter will not activate):
	$D_1 = (\varphi_{i-3} - \varphi_{i-4})$, $D_2 = (\varphi_{i-2} - \varphi_{i-3})$, ……, $D_6 = (\varphi_{i+2} - \varphi_{i+1})$
	Condition for Maxima
	if (D1>0 & D2>0 & D3<0 & D4<0 & abs(D2)<abs(D1)& abs(D3)<abs(D4)) or (D2>0 & D3>0 & D4<0 & D5<0 & abs(D3)<abs(D2)& abs(D4)<abs(D5)) or (D3>0 & D4>0 & D5<0 & D6<0& abs(D4)<abs(D3)& abs(D5)<abs(D6))
	Condition for Minima
	if (D1<0 & D2<0 & D3>0 & D4>0 & abs(D2)<abs(D1)& abs(D3)<abs(D4)) or (D2<0 & D3<0 & D4>0 & D5>0 & abs(D3)<abs(D2)& abs(D4)<abs(D5)) or (D3<0 & D4<0 & D5>0 & D6>0& abs(D4)<abs(D3)& abs(D5)<abs(D6))
		Leonard (1988)
		Leonard and Niknafs (1991)

UMIST	$r = (\varphi_{i-1} - \varphi_{i-2})/(\varphi_i - \varphi_{i-1})$ $\Psi_1 = 1/4*(3+r)$ $\Psi_2 = 1/4*(1+3*r)$ $\Psi = \max(0, \min(2, \Psi_1, \Psi_2, 2*r))$ $\varphi_w = \varphi_{i-1} + 0.5*\Psi*(\varphi_i - \varphi_{i-1})$	Lien and Leschziner (1994)
TCDF	$r = (\varphi_i - \varphi_{i-1})/(\varphi_{i-1} - \varphi_{i-2})$ $\Psi = r*(r+1)/(r^2+1) \rightarrow$ if $r<0$ $= r^3 - 2*r^2 + 2*r \rightarrow$ if $0 \leq r \leq 0.5$ $= 0.75*r+0.25 \rightarrow$ if $0.5 \leq r \leq 2$ $= (2*r^2 - 2*r - 9/4)/(r^2 - r - 1) \rightarrow$ if $2 < r$ $\varphi_w = \varphi_{i-1} + 0.5*\Psi*(\varphi_{i-1} - \varphi_{i-2})$	Zhang et al. (2015)

3.2.3. Use of flux limiters

Flux limiters are used in higher-order spatial discretization schemes to avoid the spurious oscillations or wiggles that would otherwise occur due to shocks, discontinuities, or sharp changes in the solution domain. Although many higher-order schemes surpass FOU scheme with respect to accuracy, they are prone to give rise to wiggles under certain conditions. A desirable property for a stable, non-oscillatory, higher-order scheme is preserving 'monotonicity'. No undershoots and overshoots in the solution are created in such monotonicity-preserving schemes and as a result, the solution becomes free of oscillations. The first-order upwind scheme is a classic example of monotonic schemes but has the drawback of being highly dissipative and lacking accuracy. It was previously established in a study by Godunov and Bohachevsky (1959) that linear monotonic schemes are, at most, only first-order accurate. But schemes having greater accuracy than first-order in space can be made monotonic with the help of some kind of artificial modification to ensure monotonicity.

Monotonic limiter functions usually make the solution second-order TVD, in order to guarantee stability of the scheme (Harten, 1983). TVD (or total variation diminishing) solution refers to a certain region of the solution, known as the TVD region. Sweby (1984) gave the following conditions for a TVD scheme to be at least second-order accurate in terms of the $r - \psi$ relationship:

- $\psi(r) \leq 2r$ for $0 < r < 1$
- $\psi(r) \leq 2$ for $r \geq 1$
- $r \leq \psi(r) \leq 1$ for $0 < r < 1$
- $1 \leq \psi(r) \leq r$ for $r \geq 1$

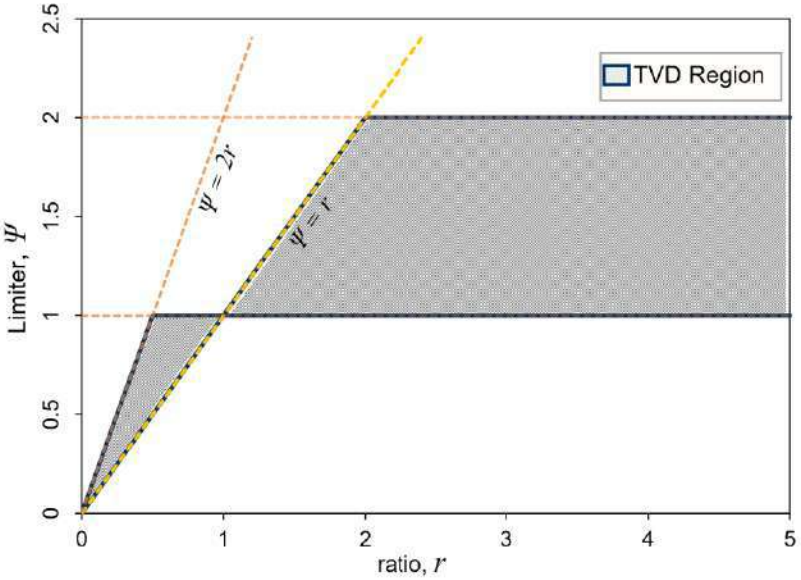

Figure 3.3 A graphical representation of second-order TVD scheme region

Here, r is a ratio of the upwind-side gradient to the downwind-side gradient, and $\psi(r)$ is called a flux limiter function (Versteeg and Malalasekera, 2007). The resulting region is usually known as Sweby's region of second-order TVD scheme, or simply as Sweby's $r - \psi$ diagram.

Although more accurate for smooth solutions, higher-order linear schemes tend to introduce spurious wiggles where discontinuities or shocks arise. Non-linear high-order techniques developed with flux limiters overcome these drawbacks. The limiter function activates only in regions of discontinuities, while for the rest of the domain, the solution remains as before. For some critical conditions, such as the presence of a steep gradient, a TVD flux limiter switches from a high-order scheme to a low-order diffusive/compressive scheme, and vice versa, to bypass the numerical dilemma. For the left cell face, r is defined as follows

$$r = \frac{\varphi_{i-1} - \varphi_{i-2}}{\varphi_i - \varphi_{i-1}} \tag{3.5}$$

The limiter function $\psi(r)$ varies for different higher-order schemes but must satisfy the above criteria to qualify as a TVD scheme. For example, in the QUICK

function, $\psi(r)$ is defined as $\Psi(r) = \frac{1}{4}(3 + r)$, or for the MUSCL function $\Psi(r) = \frac{1}{2}(1 + r)$. To ensure TVD property, these higher-order schemes were further conditioned according to Sweby's criteria, as can be seen in table 3.1.

However, a well-known inherent drawback of the classical TVD schemes is that they are sometimes 'over-restrictive' and result in clipping of extremas (Čada and Torrilhon, 2009; Zhang et al., 2015). It, therefore, cannot recover the full order of accuracy in those cases. Another similar type of limiter region was presented in a study by Leonard (1988), known as the universal limiter. Leonard named this approach as the 'ultimate strategy' and was represented in terms of normalized variables, as shown in figure 3.4 (a). The dashed line denotes the courant-number-dependent boundary, $\tilde{\varphi}_f = \tilde{\varphi}_c^n / c_r$. The normalized variable diagram is shown for $c_r = 0.5$. The normalization is done as $\tilde{\varphi}_c^n = \tilde{\varphi}_i^n = (\varphi_i^n - \varphi_{i-1}^n)/(\varphi_{i+1}^n - \varphi_{i-1}^n)$; this expression is similar to the ratio r of Sweby region. And the limiter function $\tilde{\varphi}_f = f(\tilde{\varphi}_c^n, c_r)$, depending on the higher-order scheme used. An extended version of the courant number dependent Sweby diagram in (r, Ψ) coordinates, corresponding to the universal limiter, is portrayed in figure 3.4 (b). It is evident that compared to this extended TVD region, the one shown in figure 3.3 is much more restrictive. The left boundary in the extended diagram has a slope of $2/c_r$, compared to the slope of 2 in the original diagram. As the courant number changes from 0 to 1, the extended diagram will gradually approach the original slope. Also, the upper

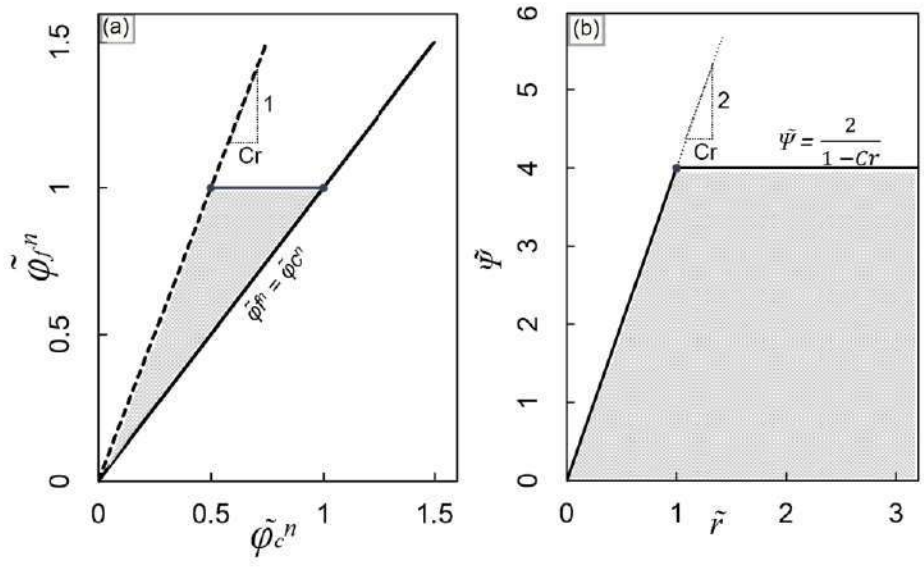

Figure 3.4 (a) Universal limiter region (b) CFL-dependent extended Sweby diagram

boundary in figure 3.4(b) increases in height with increasing c_r value. In his study, Leonard had denoted the Sweby limiter almost same as 'ultimate' strategy but with a courant number set of zero. In the present study, both types of limiters were according to their suitability, as seen in some schemes in table 3.1.

3.2.4. Metrics used for performance analysis

The accuracy of the schemes was quantitatively measured using two statistical parameters. One of them is the normalized root mean square error (NRMSE), which estimates the deviation from the analytical solution. The schemes were ranked using this NRMSE parameter, with the schemes producing the least error values being assigned smaller ranks and the more deviating ones getting larger ranks. The formula used for calculating NRMSE is as follows

$$NRMSE = \sqrt{\frac{\sum_{i=1}^{N}(\varphi_i^{n\,(numertical)} - \varphi_i^{n\,(exact)})^2}{\sum_{i=1}^{N}(\varphi_i^{n\,(exact)})^2}} \tag{3.6}$$

Here, $\varphi^{numertical}$ and φ^{exact} denotes the numerical and exact solution respectively at any node i and at any time n. In this case, the solution refers to the concentration of tracer distribution. N is the total number of nodes in the grid.

The other parameter used was the normalized variance (NV) index which reflects the scheme's numerical diffusion. The closer the NV index value is to zero, the closer the scheme is to exact solution. On the other hand, the more negative the NV index is (when NV<0) the more diffusive the scheme is, and conversely the more positive the NV index is (when NV>0) the more compressive the scheme is (causes artificial steepening instead of dissipation). This method of assessing numerical diffusion is also known as the variance-variation diagnostic method (Lin and Liu, 2019; Wu and Zhu, 2010).

$$NV\ index = \frac{\sum_{i=1}^{N}(\varphi_i^{n\,(numertical)})^2}{\sum_{i=1}^{N}(\varphi_i^{n\,(exact)})^2} - 1 \tag{3.7}$$

The first-order upwinding method was also tested alongside the higher-order schemes. Although the first-order upwinding method introduces significant artificial diffusion, it is one of the most stable differencing methods. So, it was considered as a

good base condition for visual comparison in assessing the performance of the higher-order schemes.

3.2.5. 2D Advection model

In the next stage of the study, the schemes that proved to be more numerically stable and accurate were transformed from one to two dimensions and applied to more complicated flow patterns. The governing equation of two-dimensional advection can be given by

$$\frac{\partial C}{\partial t} + u\frac{\partial C}{\partial x} + v\frac{\partial C}{\partial y} = 0 \tag{3.8}$$

Tracer concentration, *C,* is the advected variable here, and *u*, *v* represent the local velocity in the x- and y-direction respectively. The advective transport was caused due to a given uniform velocity field (i.e., velocity *u* and *v* were set as 1m/s throughout the grid) that is oblique to the horizontal direction at an angle of 45°. Equation 3.5 can be resolved into the following form

$$C_i^{n+1} = C_i^n - u.\Delta t\frac{\partial C}{\partial x} - v.\Delta t\frac{\partial C}{\partial y} \tag{3.9}$$

The advective terms in both x and y directions are resolved by extending the Matlab® (R2021b) programmes developed for 1D advection to 2D. Instead of two control volume faces as shown in the grid of figure 3.2, there were now four cell faces for two-dimensional advection. Each of the cell faces were estimated by the updated programmes.

3.3. Performance analysis for 2D plane open channel flow

The higher-order advective schemes will next be tested in the two-dimensional coupled DA-RANS model of Zobeyer (2012), developed for simulating flow in rivers. Before moving on to the more complicated 3D flow cases, it was essential to understand the behavior of the schemes in simple yet representative 2D flow problems. Flow varies only in the longitudinal and vertical directions, with no variation in the transverse direction in this plane flow model.

3.3.1. Boundary-fitted grid coordinate system

For the RANS model, governing equations were represented in a non-orthogonal boundary-fitted grid coordinate system (ξ, ζ) from the Cartesian coordinate system (x, z). In transforming the equations from Cartesian to generalized boundary-fitted coordinate, ζ direction coincides with the vertical direction and parallel to the z axis, while ξ follows the bed and water surface in the longitudinal direction. Figure 3.5 shows a schematic diagram of this transformed grid system. As the new grid coordinates are generally non-orthogonal, it means the angle between the new coordinates may deviate from 90°.

3.3.2. Governing equations of 2D flow model

In this coupled model, results from the DA model (i.e., water surface elevation and depth-averaged velocity) were linked with the RANS model. Another unique feature of the model was the conservation of mass balance by introducing correction terms in the RANS horizontal momentum equations.

The governing equations of the 2D depth-averaged model consist of the one-dimensional continuity equation and the DA x-momentum equation. The continuity equation can be written as

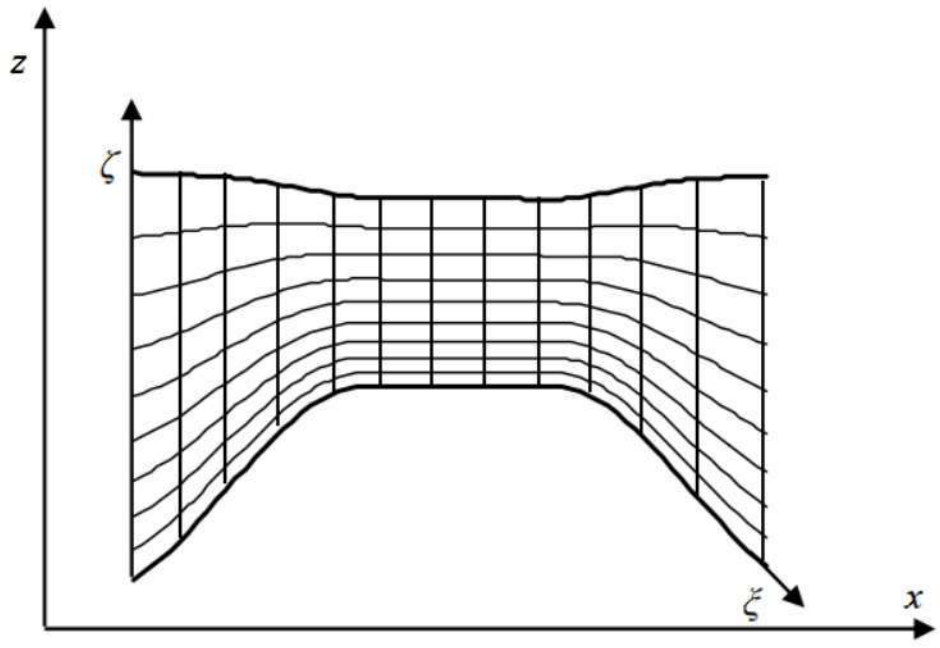

Figure 3.5 Schematic diagram of boundary-fitted grid coordinate system (Zobeyer, 2012)

$$\frac{\partial h}{\partial t} + \frac{\partial h\bar{u}}{\partial x} = 0 \tag{3.10}$$

Depth-averaged (DA) x-momentum equation

$$\frac{\partial h\bar{u}}{\partial t} + \frac{\partial h\bar{u}^2}{\partial x} + \frac{\partial h\overline{u^p u^p}}{\partial x} + gh\frac{\partial (h+z_b)}{\partial x} \tag{3.11}$$
$$+ \frac{1}{\rho}\left(\frac{\partial h\overline{p^p}}{\partial x} + p_b^p\frac{\partial z_b}{\partial x}\right) - \frac{1}{\rho}\frac{\partial h(\sigma_x^d + \overline{\sigma_x^p})}{\partial x} + \frac{1}{\rho}(\tau_{bx}^d + \tau_{bx}^p) - hX = 0$$

Initially, when the DA model is run, the water surface elevation and the depth-averaged velocity will be computed from equation 3.11, neglecting the primed terms. Perturbation velocities and non-hydrostatic pressure are together called the 'primed terms'. Here, X is the correction term, and the primed terms' effects are lumped in the term hX.

The RANS x-momentum and the pressure Poisson equations for incompressible fluid, including the correction term (X) in the non-orthogonal boundary-fitted coordinate system, are solved neglecting the normal stress. The equations were partially transformed from Cartesian to the boundary-fitted grid, i.e. leaving the velocity components in Cartesian coordinate as before.

The RANS x-momentum equation

$$\frac{\partial u}{\partial t} + \boldsymbol{U_c}\frac{\boldsymbol{\partial u}}{\boldsymbol{\partial \xi}} + W_c\frac{\partial u}{\partial \zeta} = -\frac{1}{\rho}\left(\xi_x\frac{\partial p}{\partial \xi} + \zeta_x\frac{\partial p}{\partial \zeta}\right) + \frac{1}{\rho}\left(\zeta_z\frac{\partial \tau_{xz}}{\partial \zeta}\right) + X \tag{3.12}$$

The pressure Poisson equation

$$\left(\xi_x\frac{\partial}{\partial \xi} + \zeta_x\frac{\partial}{\partial \zeta}\right)\left(\xi_x\frac{\partial p^p}{\partial \xi} + \zeta_x\frac{\partial p^p}{\partial \zeta}\right) + \left(\xi_z\frac{\partial}{\partial \xi} + \zeta_z\frac{\partial}{\partial \zeta}\right)\left(\xi_z\frac{\partial p^p}{\partial \xi} + \zeta_z\frac{\partial p^p}{\partial \zeta}\right) \tag{3.13}$$
$$= 2\rho\left(\xi_z\frac{\partial w}{\partial \xi} + \zeta_z\frac{\partial w}{\partial \zeta}\right)\left(\xi_x\frac{\partial u}{\partial \xi} + \zeta_x\frac{\partial u}{\partial \zeta}\right) - 2\rho\left(\xi_x\frac{\partial w}{\partial \xi} + \zeta_x\frac{\partial w}{\partial \zeta}\right)\left(\xi_x\frac{\partial u}{\partial \xi} + \zeta_x\frac{\partial u}{\partial \zeta}\right)$$
$$+2\left(\xi_x\frac{\partial}{\partial \xi} + \zeta_x\frac{\partial}{\partial \zeta}\right)\left(\xi_z\frac{\partial \tau_{xz}}{\partial \xi} + \zeta_z\frac{\partial \tau_{xz}}{\partial \zeta}\right) + \rho\left(\xi_x\frac{\partial X}{\partial \xi} + \zeta_x\frac{\partial X}{\partial \zeta}\right)$$
$$-\rho g\left(\xi_x\frac{\partial H}{\partial \xi} + \zeta_x\frac{\partial H}{\partial \zeta}\right)$$

The RANS z-momentum equation

$$U_c \frac{\partial w}{\partial \xi} + W_c \frac{\partial w}{\partial \zeta} = -\frac{1}{\rho}\left(\zeta_z \frac{\partial p^p}{\partial \zeta}\right) + \frac{1}{\rho}\left(\xi_x \frac{\partial \tau_{xz}}{\partial \xi} + \zeta_x \frac{\partial \tau_{xz}}{\partial \zeta}\right) \tag{3.14}$$

Here, $U_c = u\xi_x + w\xi_z$, and $W_c = u\zeta_x + w\zeta_z$, are called the contravariant velocity components and ξ_x , ξ_z , $\zeta_x$and ζ_z are components of the transformation matrix.

3.3.3. Development of 2D RANS model with higher-order discretization

In the original model of Zobeyer (2012), the bold term highlighted in equation 3.12, $\boldsymbol{U_c \frac{\partial u}{\partial \xi}}$ was discretized with the dissipative first-order upwind method by default. In the present study, the code of the model was modified in such a way that there was a provision to select whether to run the RANS model with first-order or higher-order advective methods. All the schemes were created as function files in Matlab® (R2021b), which could be called into the main programme file of the RANS model, depending on which higher-order scheme the user intends to apply. Figure 3.6 displays a flowchart of the original coupled 2D DA-RANS model of Zobeyer. The stage where changes were made in the present study is highlighted in the figure.

3.3.4. Verification of model and testing of higher-order schemes

The model was simulated for the selected higher-order methods, as found from the pure advection case. Validation of the model was done by comparing its output with experimental results. The RANS model was then used to simulate hypothetical scenarios of long reaches with different numerical grid coarseness in the longitudinal flow direction. The model was run with the original first-order upwind discretization as well; this served as a measure of quantification to understand the improvement in performance of the RANS model with the new integration of higher-order schemes, compared to the original model. Since no field data were available for the hypothetical test cases, the grid-independent model results were taken as a benchmark for error analysis. With the increased coarsening of the grid, the accuracy of the schemes was analyzed by comparing the velocity profiles with the grid-independent model results, and the schemes with relatively better performance were identified.

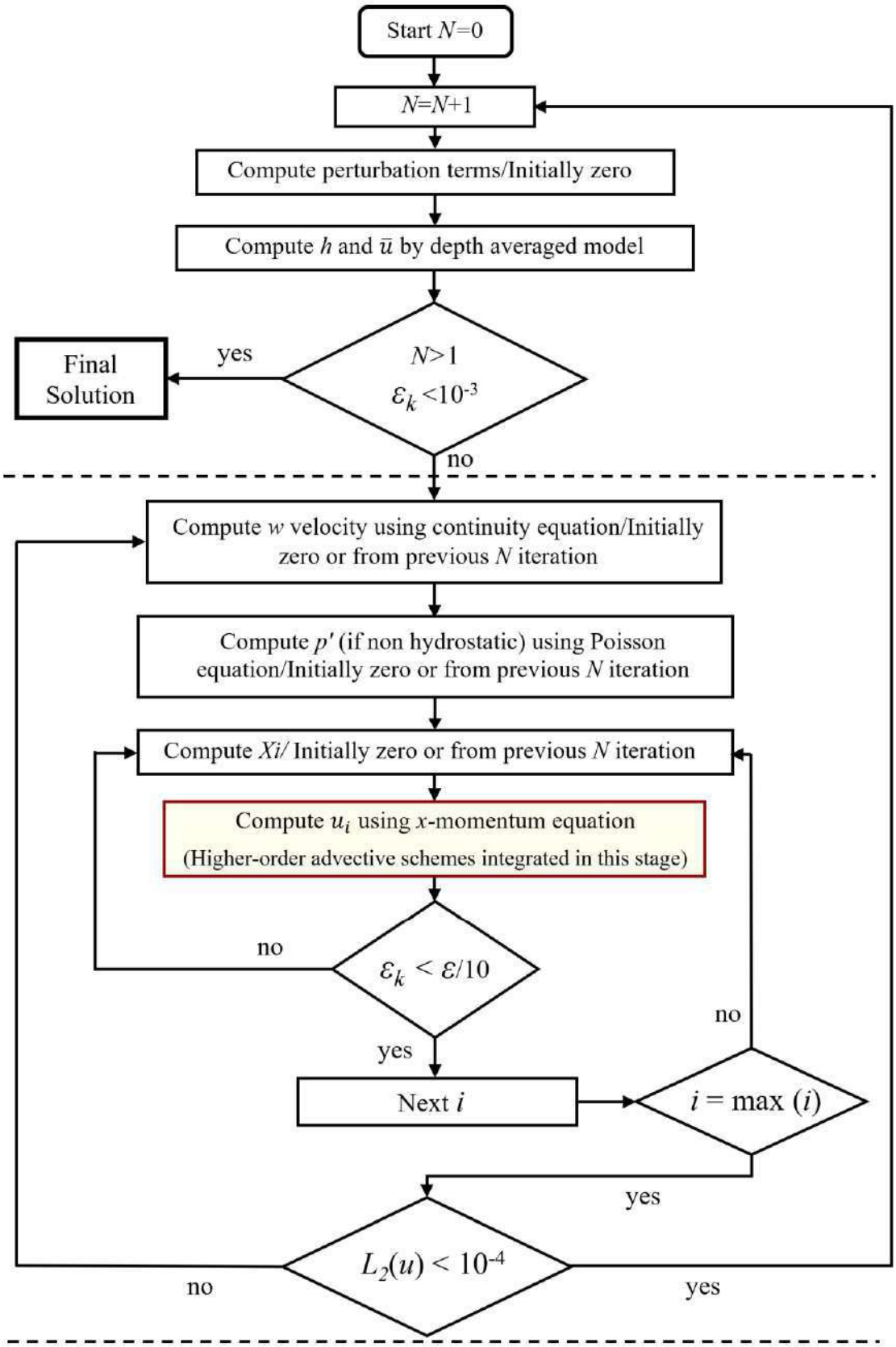

Figure 3.6 Flowchart of the coupled 2D DA-RANS model (Zobeyer, 2012)

3.4. Extension of coupled DA-RANS model for 3D flow

After the higher-order schemes were found to produce sufficiently stable and accurate results in the 2D flow simulations, the approach was then applied to the more complex three-dimensional flow, as observed in nature. The model was extended for the 3D version of the coupled DA-RANS model using numerical techniques similar to the 2D plane flow.

3.4.1. Governing equations and grid system of 3D model

The depth-averaged equations used here were two-dimensional. The depth-averaged continuity or the mass conservation equation in two dimensions is

$$\frac{\partial h}{\partial t} + \frac{\partial h\bar{u}}{\partial x} + \frac{\partial h\bar{v}}{\partial y} = 0 \tag{3.15}$$

And the depth-averaged (DA) x- and y-momentum equations are

$$\frac{\partial h\bar{u}}{\partial t} + \frac{\partial h\bar{u}^2}{\partial x} + \frac{\partial h\overline{u^p u^p}}{\partial x} + \frac{\partial h\bar{u}\bar{v}}{\partial y} + \frac{\partial h\overline{u^p v^p}}{\partial y} + gh\frac{\partial (h+z_b)}{\partial x} + \frac{1}{\rho}\left(\frac{\partial h\overline{p^p}}{\partial x} + p_b^p\frac{\partial z_b}{\partial x}\right) - \frac{1}{\rho}\left(\frac{\partial h(\sigma_x^d + \overline{\sigma_x^p})}{\partial x} + \frac{\partial h(\tau_{xy}^d + \overline{\tau_{xy}^p})}{\partial x}\right) + \frac{1}{\rho}(\tau_{bx}^d + \tau_{bx}^p) - hX = 0 \tag{3.16}$$

$$\frac{\partial h\bar{v}}{\partial t} + \frac{\partial h\bar{u}\bar{v}}{\partial x} + \frac{\partial h\overline{u^p v^p}}{\partial x} + \frac{\partial h\bar{v}^2}{\partial y} + \frac{\partial h\overline{v^p v^p}}{\partial y} + gh\frac{\partial (h+z_b)}{\partial y} + \frac{1}{\rho}\left(\frac{\partial h\overline{p^p}}{\partial y} + p_b^p\frac{\partial z_b}{\partial y}\right) - \frac{1}{\rho}\left(\frac{\partial h(\tau_{xy}^d + \overline{\tau_{xy}^p})}{\partial x} + \frac{\partial h(\sigma_y^d + \overline{\sigma_y^p})}{\partial y}\right) + \frac{1}{\rho}(\tau_{by}^d + \tau_{by}^p) - hY = 0 \tag{3.17}$$

DA model is simulated first by neglecting the primed terms again, as was done in the 2D case. The normal stresses are neglected here in this model as well. All the effects of perturbation velocities and non-hydrostatic pressure are stored in hX and hY, and for the two depth-averaged momentum equations, X and Y represent the two correction terms. The DA equations were expressed in the conservative form after

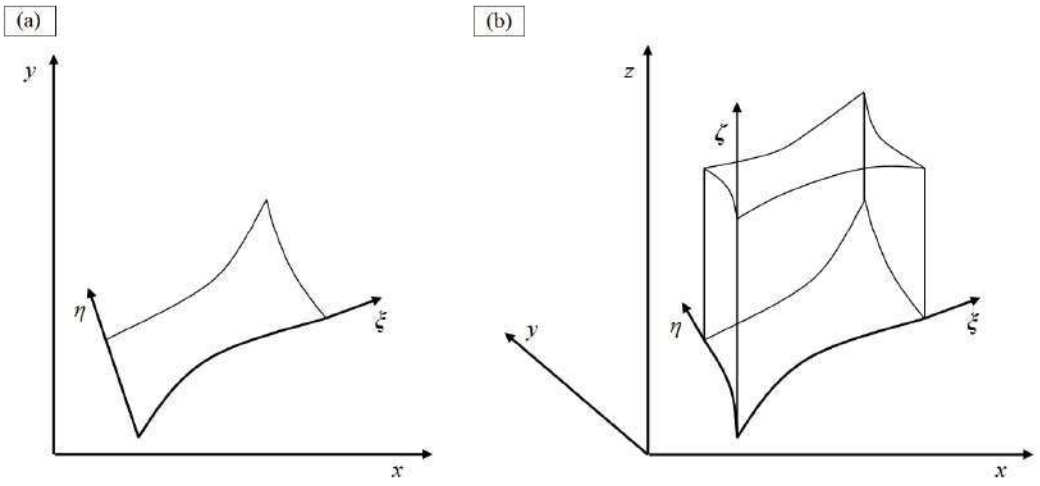

Figure 3.7 Boundary-fitted grid coordinate system in the **(a)** *x, y* dimensions **(b)** *x, y, z* dimensions (Zobeyer, 2012)

transforming them from Cartesian to non-orthogonal boundary-fitted coordinates by the partial transformation approach. The velocity components were left in Cartesian coordinates. The (x,y) to (ξ,η) transformation is shown in figure 3.7(a).

The RANS continuity, x- and y-momentum equations, including two correction terms (X and Y) were expressed in a similar manner, but the transformation here was from the Cartesian coordinate (x,y,z) to boundary-fitted coordinates ($\boldsymbol{\xi}$, η, $\boldsymbol{\zeta}$) of figure 3.7(b). The $\boldsymbol{\zeta}$ direction coincides with the vertical direction, while $\boldsymbol{\xi}$ and η follow the bed and water surface profile. The 3D RANS x-, y-momentum equations are as follows

$$\frac{\partial u}{\partial t} + \boldsymbol{U_c}\frac{\boldsymbol{\partial u}}{\boldsymbol{\partial \xi}} + \boldsymbol{V_c}\frac{\boldsymbol{\partial u}}{\boldsymbol{\partial \eta}} + W_c\frac{\partial u}{\partial \zeta} = -\frac{1}{\rho}\left(\xi_x\frac{\partial p^p}{\partial \xi} + \eta_x\frac{\partial p^p}{\partial \eta} + \zeta_x\frac{\partial p^p}{\partial \zeta}\right) + g\left(\xi_x\frac{\partial H}{\partial \xi} + \eta_x\frac{\partial H}{\partial \eta}\right) + \frac{1}{\rho}\left(\xi_z\frac{\partial \sigma_x}{\partial \xi} + \eta_z\frac{\partial \tau_{xy}}{\partial \eta} + \zeta_z\frac{\partial \tau_{xz}}{\partial \zeta}\right) + X \tag{3.18}$$

$$\frac{\partial v}{\partial t} + \boldsymbol{U_c}\frac{\boldsymbol{\partial v}}{\boldsymbol{\partial \xi}} + \boldsymbol{V_c}\frac{\boldsymbol{\partial v}}{\boldsymbol{\partial \eta}} + W_c\frac{\partial v}{\partial \zeta} = -\frac{1}{\rho}\left(\xi_y\frac{\partial p^p}{\partial \xi} + \eta_y\frac{\partial p^p}{\partial \eta} + \zeta_y\frac{\partial p^p}{\partial \zeta}\right) + g\left(\xi_y\frac{\partial H}{\partial \xi} + \eta_y\frac{\partial H}{\partial \eta}\right) + \frac{1}{\rho}\left(\xi_z\frac{\partial \tau_{xy}}{\partial \xi} + \eta_z\frac{\partial \sigma_y}{\partial \eta} + \zeta_z\frac{\partial \tau_{yz}}{\partial \zeta}\right) + Y \tag{3.19}$$

The pressure Poisson equation and the z-momentum equations were similarly expressed in the new coordinate system. Once the RANS model results are available, DA model results can be updated iteratively by incorporating the effects of non-uniform velocity and non-hydrostatic pressure.

3.4.2. Development of the updated 3D RANS model

The advective terms in the RANS x- and y-momentum equations are highlighted in equations 3.18 and 3.19 as bold terms, $\boldsymbol{U_c \frac{\partial u}{\partial \xi}}$, $\boldsymbol{V_c \frac{\partial u}{\partial \eta}}$, $\boldsymbol{U_c \frac{\partial v}{\partial \xi}}$ and $\boldsymbol{V_c \frac{\partial v}{\partial \eta}}$. In the original 3D RANS model of Zobeyer (2012), these terms were again discretized with the first-order upwind scheme, suffering from numerical diffusion. In the present study, this portion of the model's code was omitted, in favour of a new external function that has the flexibility of selecting an advective scheme of the user's choice. This function accepts relevant inputs to run the chosen higher-order discretizing schemes created in Matlab® (R2021b), and returns the advective term. A similar set of commands was integrated four times in the model with different inputs of regular and contravariant velocity components for each of the four convective terms. The coupling with the depth-averaged model was kept the same as before.

3.4.3. Simulation of 3D flow test cases

The newly updated coupled 3D DA-RANS model was used to simulate different experimental flow conditions, and the simulated velocity profiles were compared with experimental results for model verification. The performance of the three-dimensional model, in terms of accuracy and computational efficiency, was next analyzed for various 3D open channel flow scenarios and varying grid coarseness. However, most of these experimental cases were found to be inadequate for efficiency analysis, as the grid coarseness could not be increased significantly. Experiments carried out in laboratories were often on a small scale and were limited in size and extent. For larger values of space discretization Δx and Δy, bathymetric features in the physical model may be lost, and the numerical simulation would not be representative of the laboratory experiments. Several hypothetical conditions of sufficiently large dimensions were simulated to overcome this limitation. The grid-independent model results were taken

as a standard for comparison in these test cases. Finally, a comparative analysis was done between the increased savings in computational time and the associated reductions in the accuracy of flow variables with gradual coarsening of the numerical grid.

The upgraded 3D model was also used to simulate a real case open channel flow scenario of Padma River near Naria Upazila. In recent years, the riverbanks of Padma river near Naria Upazila of Shariatpur are experiencing severe erosion, and it has become growing concern for Bangladesh (RRI, 2019). Several studies have already been conducted in this region, but most of them were limited to two-dimensional modeling (Noor et al., 2021). However, the complex hydro-morphology at this location makes it much more difficult to attain representative flow parameters (i.e., bed shear, nearbed velocity, vertical distribution of velocity etc.) from 2D simulations. In the present study, a three-dimensional model has been setup and the resulting flow variables found from the 3D model were then compared with the results from a conventional and widely used 2D depth-averaged hydrodynamic model, River2D.

CHAPTER 4

RESULTS AND DISCUSSION

4.1. Introduction

First, the results of the higher-order methods are presented here for the pure advection case. The performance of the schemes was assessed against the analytical solution, and the best-performing ones were identified from this simplified case and were then further tested in the coupled DA-RANS of two-dimensional plane flow, and finally in the complete three-dimensional open channel flow version. Numerical results of the models provided some valuable observations regarding the performance of the higher-order schemes and their advantages over the basic first-order upwind method.

4.2. Idealized test cases for pure advection

The schemes were applied to unsteady, one-dimensional and two-dimensional pure advection at constant velocity scenario to demonstrate the stability and accuracy of the higher-order schemes. The accuracy of the schemes was quantitatively measured using the normalized root mean square error (NRMSE), which estimates the deviation from the analytical solution, and the normalized variance (NV) index which reflects the scheme's numerical diffusive tendency. First-order upwinding method was also tested alongside - which provided a good base condition for visual comparison, being one of the most stable differencing methods.

4.2.1. Results for 1D advection

For the one-dimensional testing, three different tracer concentration profiles were used to evaluate the performance of the schemes. The three initial tracer distribution profiles were that of a triangular, a rectangular, and a half-circular distribution. At the same time, the results were observed for three different values of courant number, $c_r =$ 0.1, 0.5 and 0.9. Each of the three initial profiles that were selected

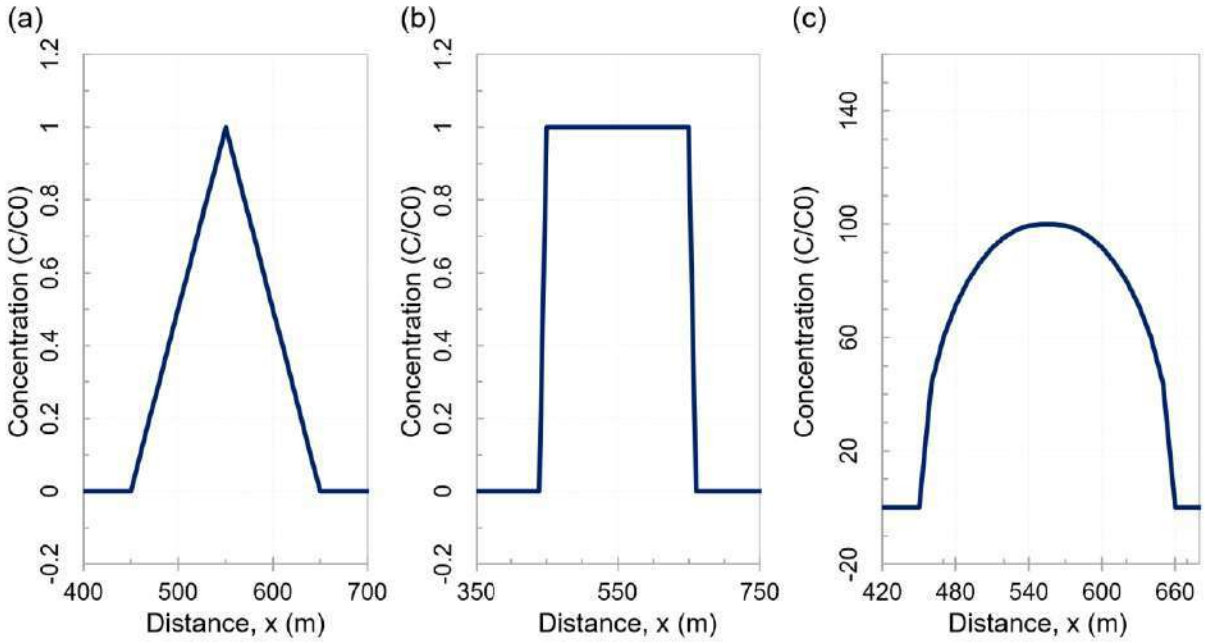

Figure 4.1 Initial tracer concentration profiles (a) triangular, (b) rectangular, and (c) half-circular distribution

represented a different slope condition: constant slope in the triangular distribution, gradually changing slope in the half-circular distribution and sudden slope change in the rectangular distribution. The distribution shapes are chosen so that the results may represent fundamental characteristics of behavior that might be encountered in real-life scenarios. The courant number values chosen were used to represent one low, one moderate and one high value. Too small values of courant numbers (i.e. below 0.1) were deliberately avoided in the test cases, since smaller courant numbers have been observed to produce worse artificial numerical diffusion and phase lags in previous studies (e.g., Leonard, 1991). All nine numerical test cases were simulated for 450 seconds in unsteady, one-dimensional pure advection at a constant velocity scenario.

Flux limiters of different forms were imposed on many of the schemes implemented in the present study, which resulted in total variation diminishing (TVD) solutions. In regions of oscillations or wiggles due to shocks, discontinuities, or sharp changes, these limiters 'smoothens' out the discontinuities to produce a more stable

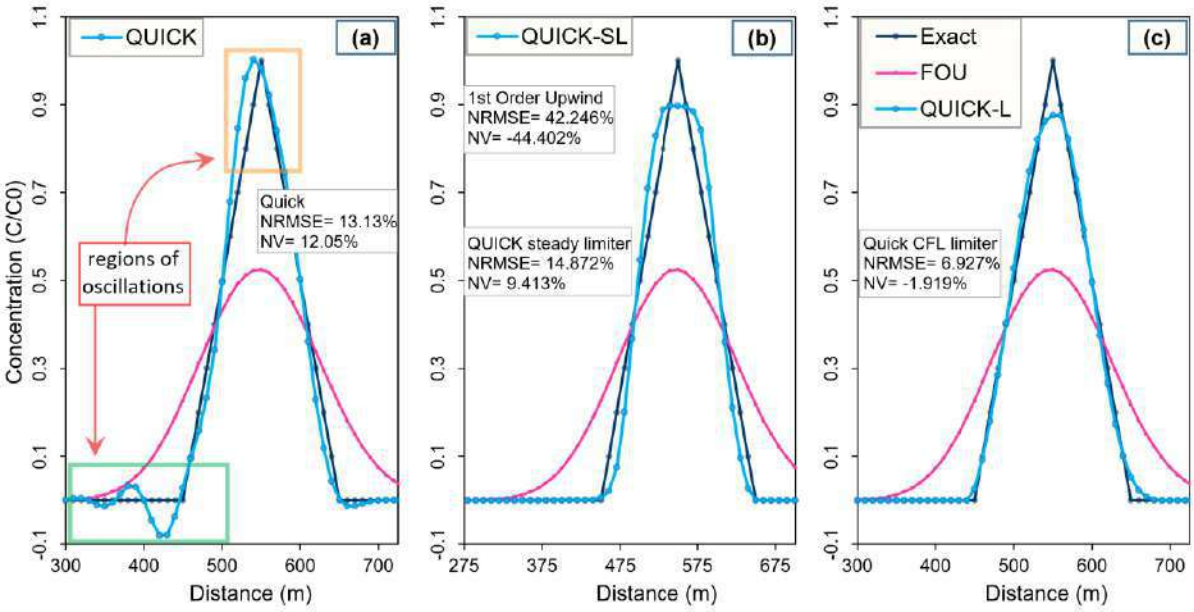

Figure 4.2 QUICK scheme results, (a) without limiter, (b) with steady limiter, and (c) with CFL limiter

solution overall. Broadly, two types of limiters were used in this study. One of which was independent of the courant number of the simulation – this is the steady limiter. And the other one is a function of courant number – termed here as CFL limiter. Figure 4.2(a) shows the third-order QUICK scheme of Leonard (1979) at the end of the 450s simulation for c_r=0.1. It is evident that oscillations or wiggles are present in regions of discontinuity. It gives rise to physically unrealistic negative values and instability, even though its peak accuracy is much better than the FOU scheme. Figures 4.2(b) and (c) respectively show the QUICK scheme with the steady limiter and the CFL limiter. Both the limiters are effective in making the solution oscillation-free, but the steady limiter distorts the shape of the distribution significantly, and the peak is flattened. The CFL-limiter on the other hand, approximates the exact solution much more closely. Figure 4.2 also gives a visual representation of the NV index. When the numerical solution causes artificial steepening instead of dissipation, the NV index is positive (seen here for QUICK and QUICK-SL). Whereas negative values of NV represent the dissipative nature of the scheme (seen here for FOU and QUICK-L).

Table 4.1 Unstable higher-order schemes that were skipped

Scheme	Error (%)		
	$c_r = 0.1$	$c_r = 0.5$	$c_r = 0.9$
QUICK	13.128	5035.082	11745803
QUICK-SL	14.872	18.649	8808.774
WENO	11.192	38.09	388.279
ENO	12.429	32.862	312.519
MIN-MOD	11.913	19.111	189.431
SPUDS	9.919	4353.355	26070897
Van Leer	14.338	39.854	7031.474
SMART	14.872	18.649	8808.774
Euler QUICK	14.801	127.615	37167.57
WSN	14.729	46.31	20804.63
UMIST	11.895	40.056	3173.256

For higher courant number values of cr=0.5 and 0.9, however, the QUICK scheme and some of the original thirty schemes were found to become unstable and produced large oscillations with increasing time. These unstable schemes that produced extremely large NRMSE values were QUICK, QUICK with steady limiter, WENO-5, ENO-2, MIN-MOD, SPUDS, van Leer limiter with sharpener, SMART, Euler QUICK, WSN and UMIST. Although for low values like $c_r = 0.1$, these methods produced stable and more accurate results compared to the FOU scheme, for higher values like $c_r = 0.5$ and 0.9, the NRMSE values were in the order of thousands. As an example of these unstable schemes under the simulated condition, WENO scheme is shown in figure 4.3. The scheme performs considerably well for low courant number values, and the error value is much lower than the FOU method figure 4.3(a). However, as the courant number was increased, the solution became increasingly unstable with elapsing time. Although when used in conjunction with a CFL-limiter, some of these oscillating schemes, produced better results, such as (QUICK-L, WENO-L). Table 4.1 shows the progression of error in these schemes as courant number is increased, for the triangular distribution. These eleven higher-order schemes were not taken into consideration for further analysis.

The rest of the higher-order schemes along with the first-order upwinding method were ranked according to the sum of their NRMSE values for the three different tracer distributions. The results of numerical test cases and the ranking of the schemes

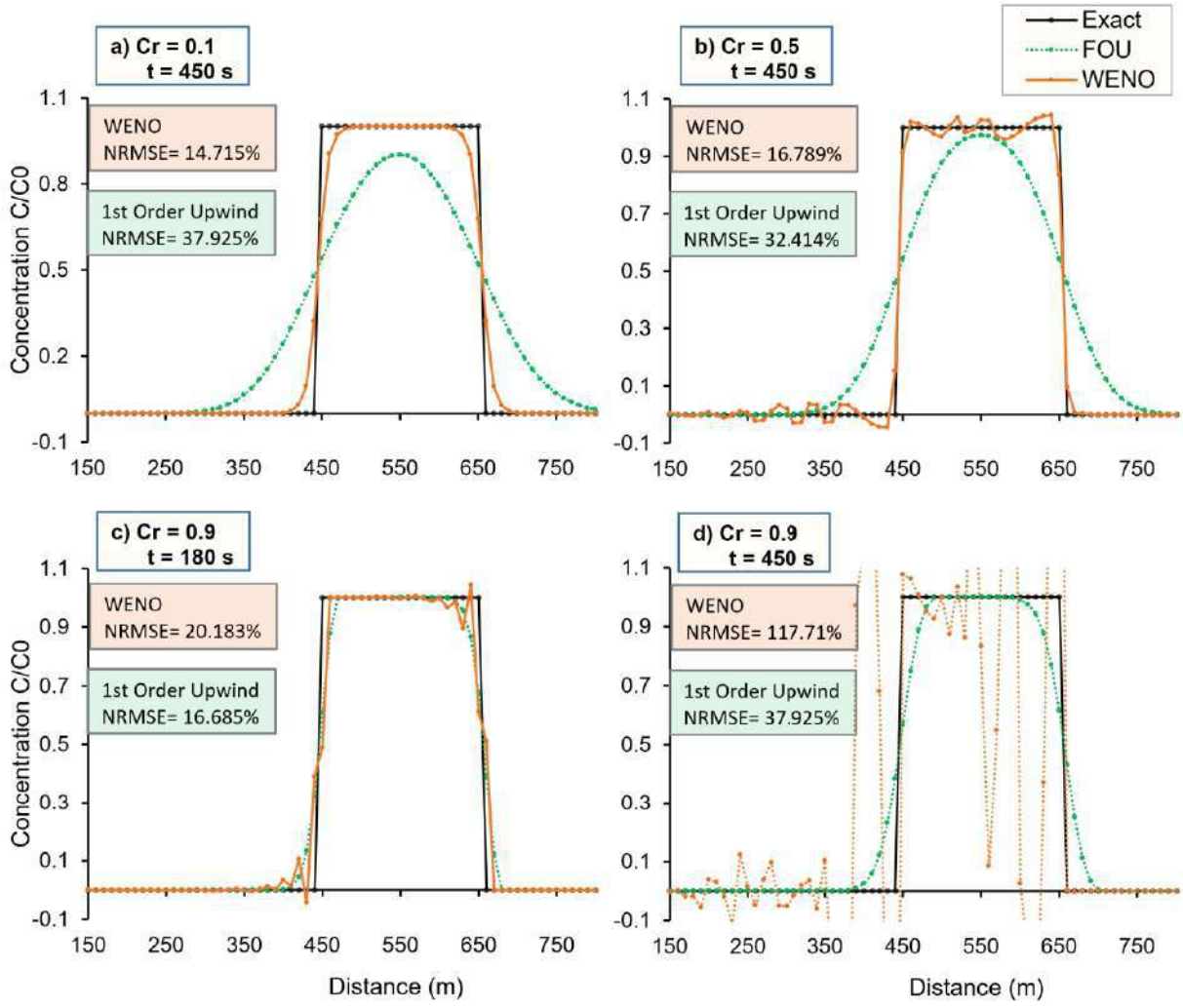

Figure 4.3 Example of a higher-order scheme producing unstable solutions for (a) c_r = 0.1, t = 450s (b) c_r = 0.5, t = 450s (c) c_r = 0.9, t = 180s (d) c_r = 0.9, t = 450s

are presented in table 4.2, table 4.3, and table 4.4 for c_r = 0.1, c_r = 0.5 and c_r = 0.9, respectively. The NV index values are also shown in the tables, which gives an idea about the diffusive (for negative NV index values) or compressive (for positive NV index values) nature of the schemes. The overall performance of all the schemes greatly increased with higher courant numbers (i.e., lower NRMSE values and NV index values closer to zero). The approximation to the exact solution was much closer for the triangular profile, where the slope was more uniform than the rectangular and the half-circular distributions.

Table 4.2 Results from the 1D numerical test cases (for $c_r = 0.1$)

Scheme Name	Courant Number = 0.1						Rank based on NRMSE
	Triangular Distribution		Rectangular Distribution		Half-circular Distribution		
	NRMSE	NV	NRMSE	NV	NRMSE	NV	
FOU	42.25	-44.40	37.93	-33.87	34.10	-35.12	20
QUICKEST	5.76	-1.56	19.80	-5.85	9.94	-2.08	10
QUICK-L	6.93	-1.92	19.66	-9.01	10.41	-2.87	12
MUSCL	6.96	-2.49	19.83	-9.13	10.37	-3.23	13
Superbee	2.98	0.80	12.89	-4.05	9.39	1.92	2
Arora-Roe	6.23	-1.95	19.17	-8.55	9.50	-2.79	9
QUICKEST-D	5.57	-1.73	19.17	-8.55	9.68	-2.71	7
2ndOU	17.06	-3.14	29.93	-7.41	19.51	-3.14	19
2ndOU-L	11.59	-7.13	24.50	-13.43	14.34	-7.13	17
4thOU	5.54	-0.11	20.30	-2.30	10.38	-0.48	11
4thOU-L	5.75	-0.75	16.75	-6.77	8.26	-1.67	6
5thOU	3.33	-0.25	15.83	-3.30	7.21	-0.78	3
5thOU-L	4.87	-0.63	15.69	-6.12	7.19	-1.33	5
WENO-L	9.98	5.12	14.70	-6.55	9.77	1.74	8
Superpower	8.87	-3.07	21.50	-9.33	10.97	-3.95	15
Hyperbee	9.09	-3.30	20.16	-10.20	10.11	-4.18	14
PHIB	13.35	11.39	14.11	-4.41	34.14	-35.02	18
Adaptive-D	4.82	0.20	15.57	-6.01	6.15	0.59	4
Adaptive	2.75	-0.22	15.76	-5.75	6.00	-0.80	1
TCDF	15.45	9.28	15.10	-6.24	10.96	2.93	16

The first-order upwinding scheme was observed to be the most diffusive and least accurate scheme, as it was expected, and hence it was placed within the last ranks for all three courant numbers. Adaptive stencil with and without the discriminator scheme exhibited overall superior performance in terms of both NRMSE and NV index values. For the upwinded polynomial transient interpolation modeling methods (i.e. 2nd, 4th and 5th order TIM schemes), the presence of limiter seemed to have some effect on the ranks, but not too drastic. Such similar schemes were considered as a single entity (i.e., where only the inclusion of a limiter or discriminator is the difference, and the basic principle remains the same). The best performing five schemes selected were

Table 4.3 Results from the 1D numerical test cases (for $c_r = 0.5$)

Scheme Name	Courant Number = 0.5						Rank based on NRMSE
	Triangular Distribution		Rectangular Distribution		Half-circular Distribution		
	NRMSE	NV	NRMSE	NV	NRMSE	NV	
FOU	30.69	-33.10	32.41	-25.44	25.53	-25.00	20
QUICKEST	4.93	-1.08	18.31	-5.12	8.88	-1.66	12
QUICK-L	6.56	-1.67	19.09	-8.54	10.25	-2.65	14
MUSCL	5.52	-1.39	17.79	-7.47	8.52	-2.22	10
Superbee	2.64	0.47	13.09	-4.00	10.02	2.60	4
Arora-Roe	5.52	-1.39	17.79	-7.47	8.52	-2.22	10
QUICKEST-D	5.02	-1.30	17.83	-7.46	8.67	-2.17	9
2ndOU	10.36	-1.07	27.04	-5.08	15.64	-1.64	17
2ndOU-L	8.69	-2.39	21.37	-10.38	11.78	-4.21	15
4thOU	4.17	-0.20	17.84	-3.02	8.39	-0.69	7
4thOU-L	4.40	-0.56	15.80	-6.17	7.67	-1.31	6
5thOU	2.99	-0.20	14.84	-3.02	6.64	-0.69	2
5thOU-L	4.36	-0.51	14.82	-5.58	6.67	-1.15	5
WENO-L	39.66	37.41	6.33	-2.44	24.02	12.11	18
Superpower	6.35	-1.59	18.00	-7.79	8.65	-2.38	13
Hyperbee	7.76	-2.03	13.82	-6.27	9.10	-3.26	8
PHIB	50.14	44.77	8.87	3.46	25.54	-24.81	19
Adaptive-D	2.47	-0.21	14.80	-5.95	5.62	-0.81	1
Adaptive	4.20	0.12	14.78	-5.60	5.66	0.08	3
TCDF	19.23	14.76	5.86	-2.22	19.65	8.63	16

the Adaptive stencil, Superbee, fifth-order upwinding with limiter (5thOU-L), QUICKEST, and MUSCL.

Overall, almost all the schemes performed better in the triangular distribution and $c_r = 0.9$ scenario and comparatively worse in the rectangular distribution and $c_r = 0.1$ scenario, among all nine numerical test cases. NRMSE values for the triangular distribution with $c_r = 0.9$, was calculated to be in the range of 1.93 to 3.44 for the five selected schemes, which suggests reasonably good accuracy, and the NV indices were within ±0.5 for these five schemes, indicating that these methods were neither too diffusive nor compressive. However, for the same scenario, NRMSE and NV index

Table 4.4 Results from the 1D numerical test cases (for $c_r = 0.9$)

Scheme Name	Courant Number = 0.9						Rank based on NRMSE
	Triangular Distribution		Rectangular Distribution		Half-circular Distribution		
	NRMSE	NV	NRMSE	NV	NRMSE	NV	
FOU	10.09	-10.37	21.41	-11.27	12.13	-8.06	18
QUICKEST	2.89	-0.32	14.23	-3.13	6.33	-0.78	10
QUICK-L	3.90	-0.66	14.89	-5.57	6.99	-1.44	14
MUSCL	3.44	-0.50	14.00	-5.05	6.22	-1.21	11
Superbee	2.41	0.08	10.90	-3.57	6.37	0.54	4
Arora-Roe	3.31	-0.43	13.80	-4.93	6.12	-1.11	9
QUICKEST-D	2.76	-0.39	13.80	-4.93	6.12	-1.11	8
2ndOU	5.21	-0.08	21.78	-1.43	10.27	-0.30	17
2ndOU-L	4.22	-0.39	15.41	-5.60	7.44	-1.38	15
4thOU	2.56	-0.13	13.32	-2.42	5.83	-0.51	7
4thOU-L	3.15	-0.25	12.71	-4.41	5.61	-0.86	6
5thOU	2.17	-0.09	12.16	-2.01	5.21	-0.40	3
5thOU-L	3.00	-0.21	12.12	-4.10	5.23	-0.73	5
WENO-L	13.07	8.56	1.30	-0.55	13.14	4.45	16
Superpower	3.97	-0.57	14.44	-5.63	6.63	-1.49	13
Hyperbee	4.08	-0.60	14.34	-5.66	6.43	-1.56	12
PHIB	115.18	164.46	45.50	24.93	12.09	-7.76	20
Adaptive-D	1.93	-0.10	11.16	-3.67	4.68	-0.55	1
Adaptive	2.97	-0.05	11.13	-3.73	4.66	-0.39	2
TCDF	82.08	57.75	38.09	-18.27	41.54	8.14	19

values for the FOU method were 10.09 and -10.37, respectively- which was much less accurate and more diffusive compared to the chosen higher-order schemes.

Again, for the rectangular distribution with $c_r = 0.1$ case, NRMSE range was from 12.89 to 19.83, and NV index values varied from -4.05 to -9.13 for the selected five schemes. In contrast, for the first-order upwinding method, the corresponding values of NRMSE and NV were 37.93 and -33.87, respectively. This further indicates towards the superior performance of the five selected higher-order schemes, irrespective of uniform or sudden slope changing scenario, and also irrespective of low, moderate or high courant numbers. The results of these five schemes for the various numerical test cases are summarized in the following subsections.

4.2.1.1. Triangular distribution profile

Figures 4.4 and 4.5 show the results of the triangular distribution from the selected five higher-order schemes at the end of the 450 seconds simulation, accompanied with the exact solution and first-order upwinding scheme (FOU) solution. In figure 4.4, it can be seen that for $c_r = 0.1$, Adaptive stencil scheme approximated the triangular distribution's local extrema most closely. The peak value of the exact solution stands at 1, and the Adaptive scheme yielded peak value of 0.9527, which can be considered near perfect. Other than at the peak of the distribution, elsewhere this scheme approached the analytical solution quite satisfactorily as well. This was followed quite closely by the Superbee scheme, which gave a peak value of 0.9472, and its NV index is slightly further from zero compared to Adaptive stencil-D scheme. As for the 5th order upwinded polynomial TIM method, the version with limiter was chosen, because without the limiters some oscillations were produced near the base of the triangle. When the limiter was used, solutions by this method was smooth near the base. The FOU method yielded a peak value of 0.5244 and a significantly diffused result.

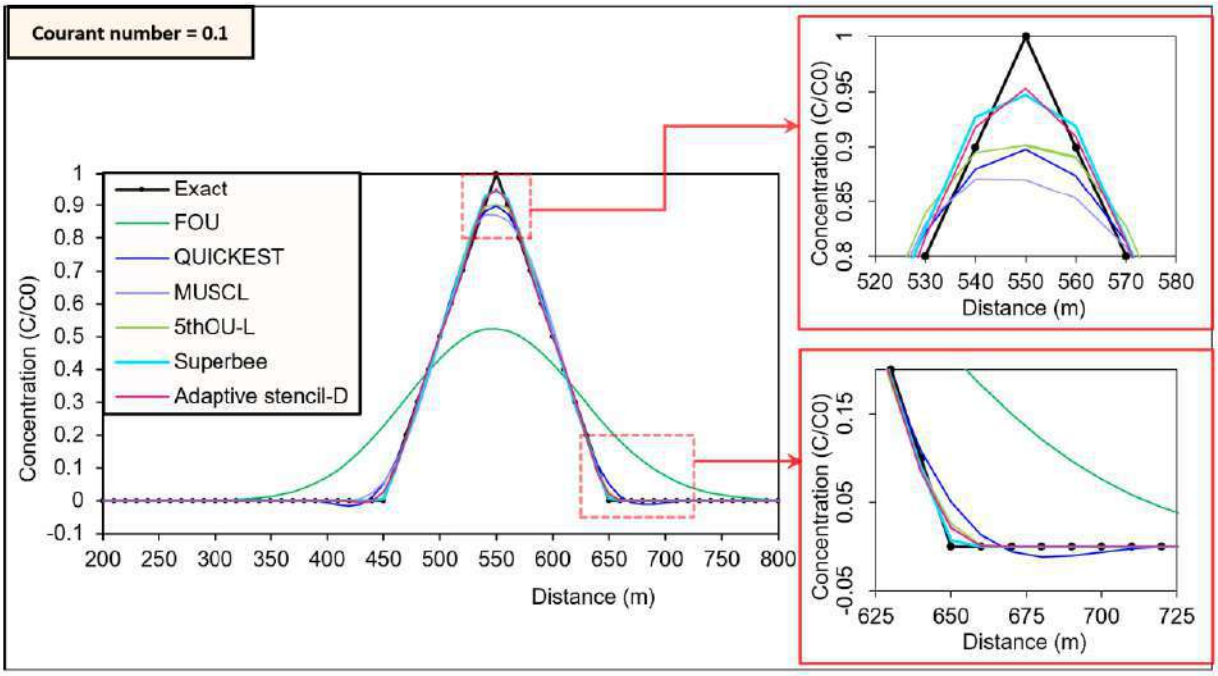

Figure 4.4 Triangular distribution results for $c_r = 0.1$

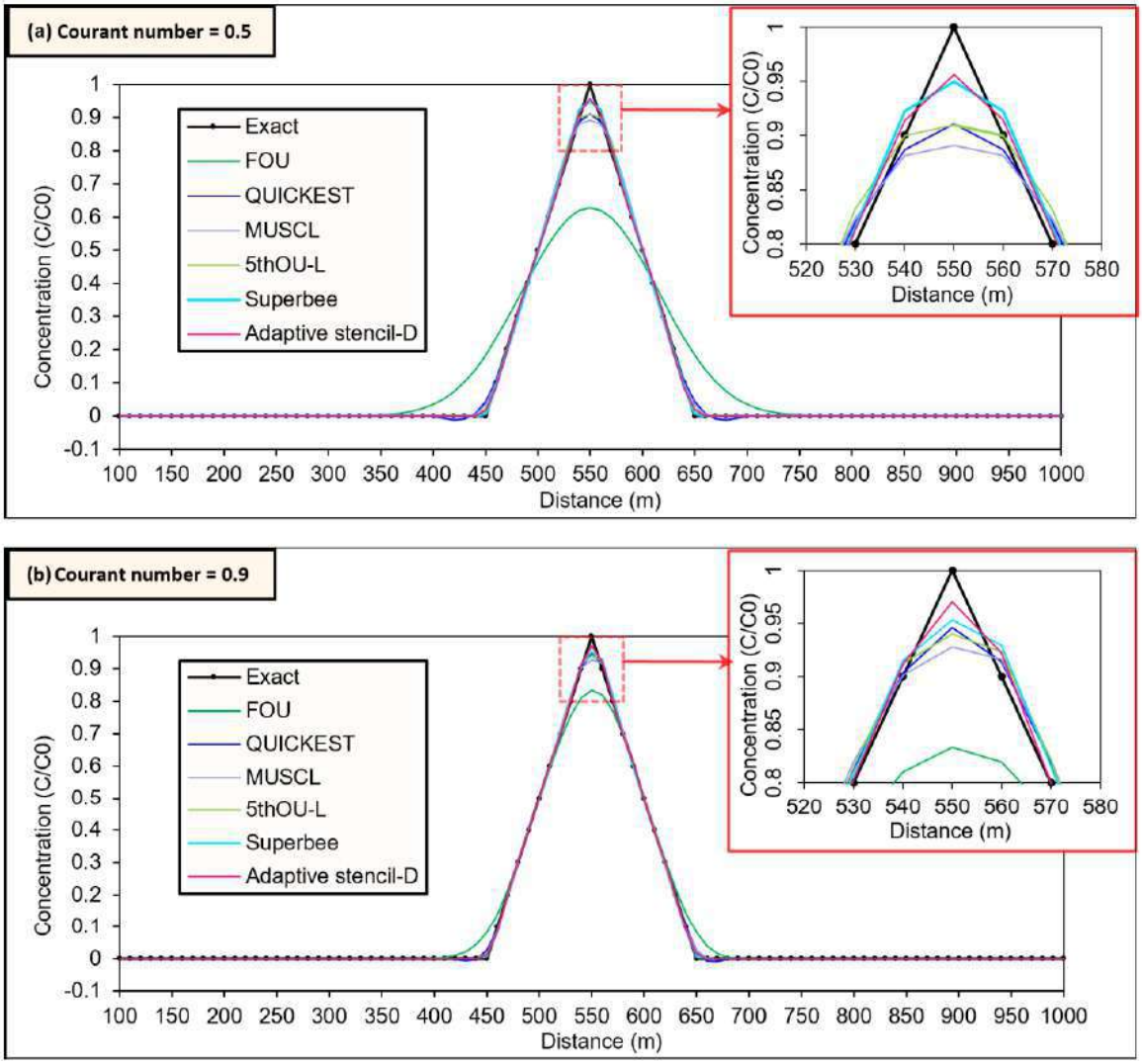

Figure 4.5 Triangular distribution results for (a) $c_r = 0.5$, (b) $c_r = 0.9$

For $c_r = 0.5$, the all higher-order schemes produced peak values within a range of 0.9-0.96. Whereas the FOU method's solution had a flattened top, with a maximum value of 0.63. It is notable that even as the courant number was increased to 0.9, all the higher-order methods improved, but only slightly compared to the $c_r = 0.1$ case, as they were already very close to the exact solution even for low courant numbers. However, the FOU scheme displayed significant improvement with the increasing courant number and achieved a peak of 0.83 in figure 4.5(b); in contrast, the apex values for all higher-order schemes were within 0.9280. All the higher-order solutions appeared to be much closer to one another as the courant number was increased to $c_r = 0.9$, although the resulting distributions were somewhat lop-sided towards the downstream direction.

4.2.1. 2. Rectangular distribution profile

Results of the rectangular distribution test case are shown in figures 4.6 and 4.7. The QUICKEST scheme quite noticeably produced spurious numerical oscillations here; although away from the points of discontinuities and near the crest and base it had approximated the exact solution well enough. The version of QUICKEST scheme shown here was used without any flux limiters. Since the rest of the higher-order schemes here all had some form of oscillation-suppressing limiters, they yielded smooth solutions. For all three courant number values, Superbee seemed to most closely resemble the exact solution. Again for $c_r = 0.9$, the Adaptive scheme approximated the sharp change of slope near discontinuities quite well. Even as the courant number was changed from low to high, yet all of the five higher-order schemes were found to be better performing than the FOU method for all courant numbers. For cr = 0.1, almost half the area of the FOU scheme's solution was out of bounds of the exact distribution; the NV value was -33.87%, exhibiting extremely dissipative trends. On the other hand, the higher-order methods were much less diffusive, and their NV indices ranged within -4 to -9%. Again, the performance of all the schemes improved for larger courant numbers; the NV index for the FOU scheme became -11.27%, and for the higher-order

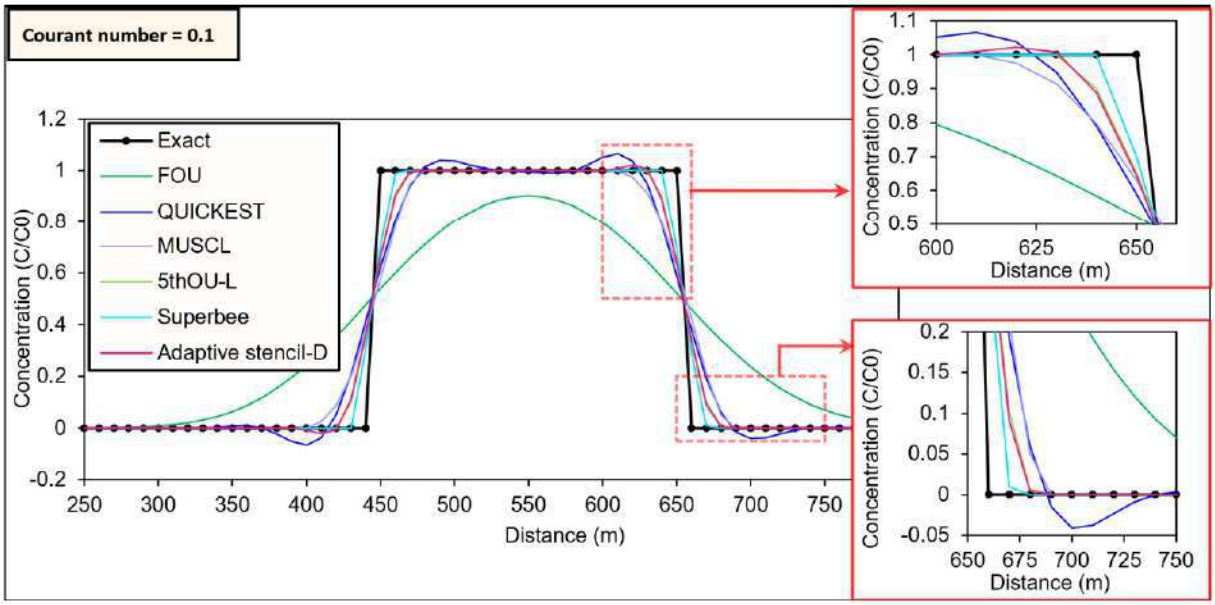

Figure 4.6 Rectangular distribution results for $c_r = 0.1$

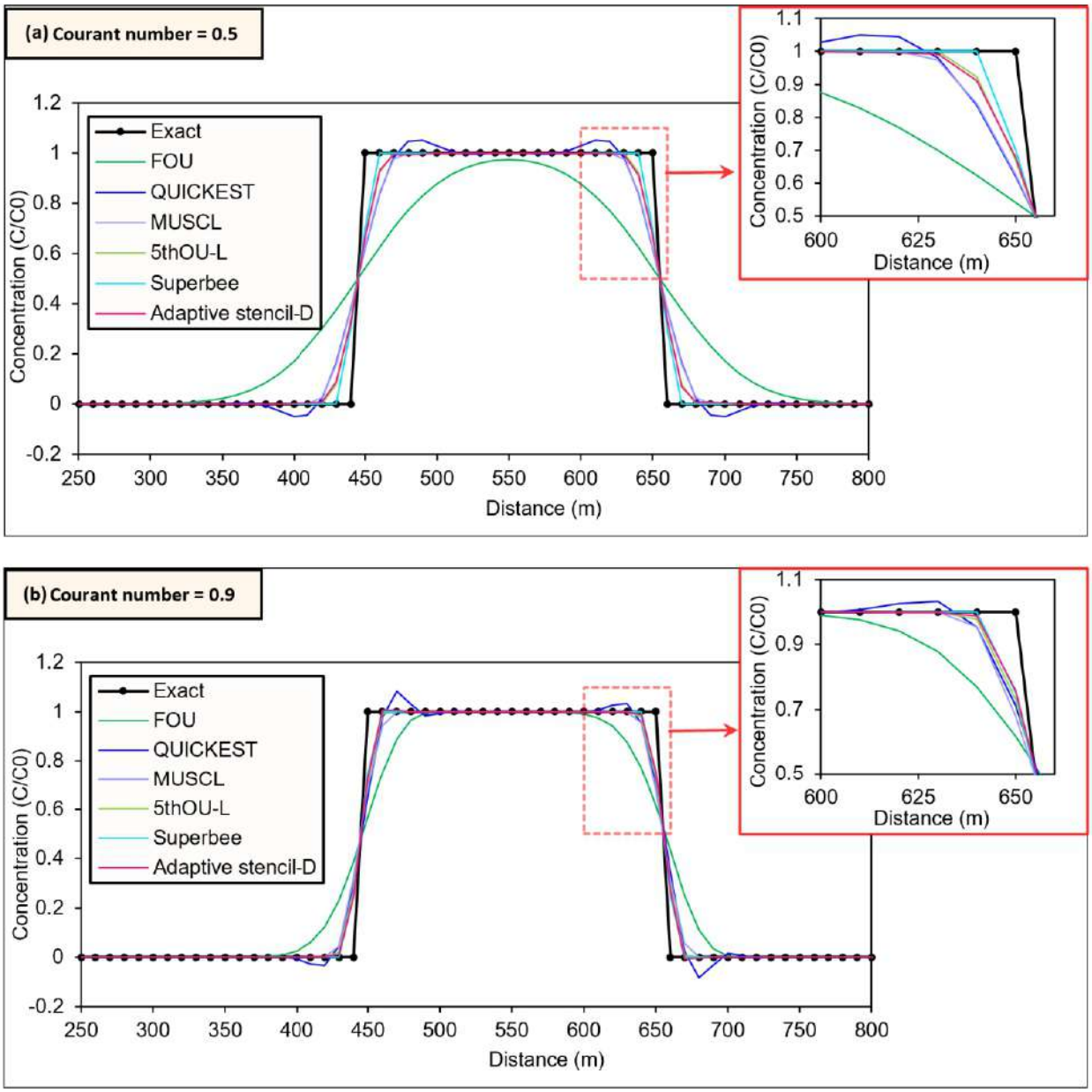

Figure 4.7 Rectangular distribution results for (a) $c_r = 0.5$, (b) $c_r = 0.9$

methods, indices were lowered to a - 3 to - 5% range. It should be noted here that the QUICKEST scheme without limiter version was deliberately shown chosen, to get an idea about how a non-limited scheme compares against other limited higher-order schemes. The presence of wiggles for the only non-limited method here, once again conveyed the necessity of introducing limiters when dealing with higher-order upwinding methods.

4.2.1.3. Half-circular distribution profile

Figures 4.8 and 4.9 show the results of the half-circular distribution test case at the end of the simulation. Except at the base of the half-circle where the point of discontinuity lies, in the rest of the distribution the higher-order schemes approached the analytical solution closely. However, the Superbee scheme produced significant numerical oscillations near the crest, even though in the previous two test cases its performance was far better. In fact, the NRMSE and NV values of Superbee solutions were the poorest among the chosen five schemes for courant number values 0.5 and 0.9, as can be seen in tables 4.3, and 4.4. The QUICKEST scheme also produced some overshoots, but they were near the sharp gradient at the base - where the line of zero concentration stars to trasnsition into the half-circle distribution. While the Adaptive scheme, 5thOU-L and MUSCL schemes yielded satisfactory enough approximation to the exact solution. In the previous two distributions, one of the drawbacks of the FOU scheme was observed as not being able to capture the maxima points of the solution adequately. Since the top of this particular tracer profile was flattened in the initial distribution itself, the error values for the first-order upwinding method were comparatively lower than the other two profiles.

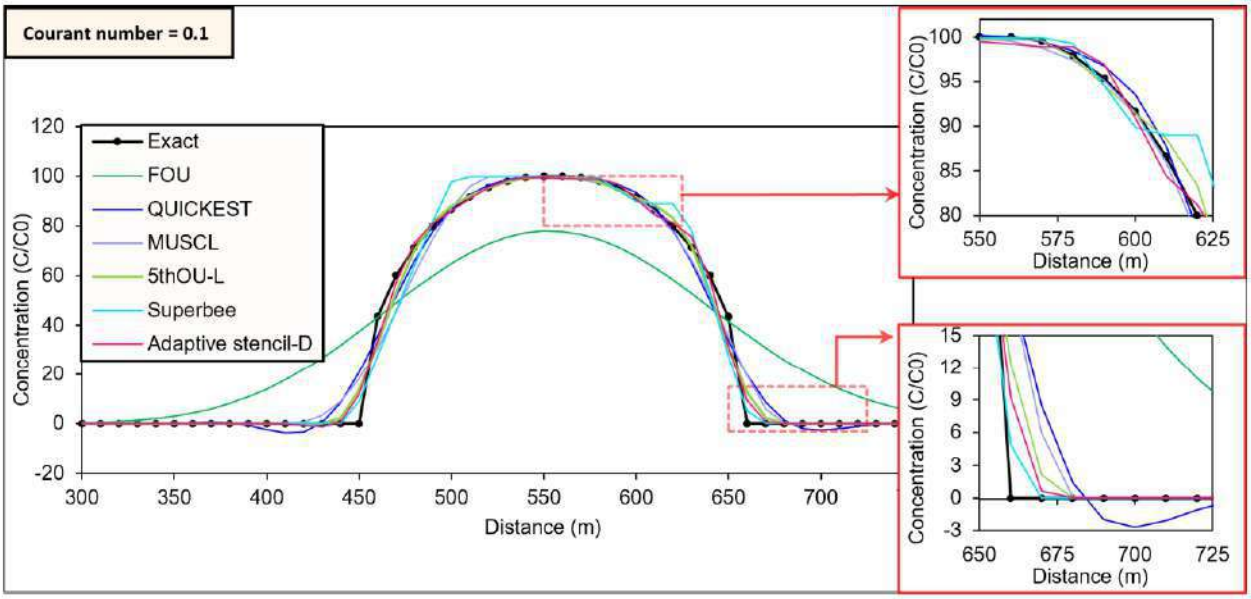

Figure 4.8 Half-circular distribution results for $c_r = 0.1$

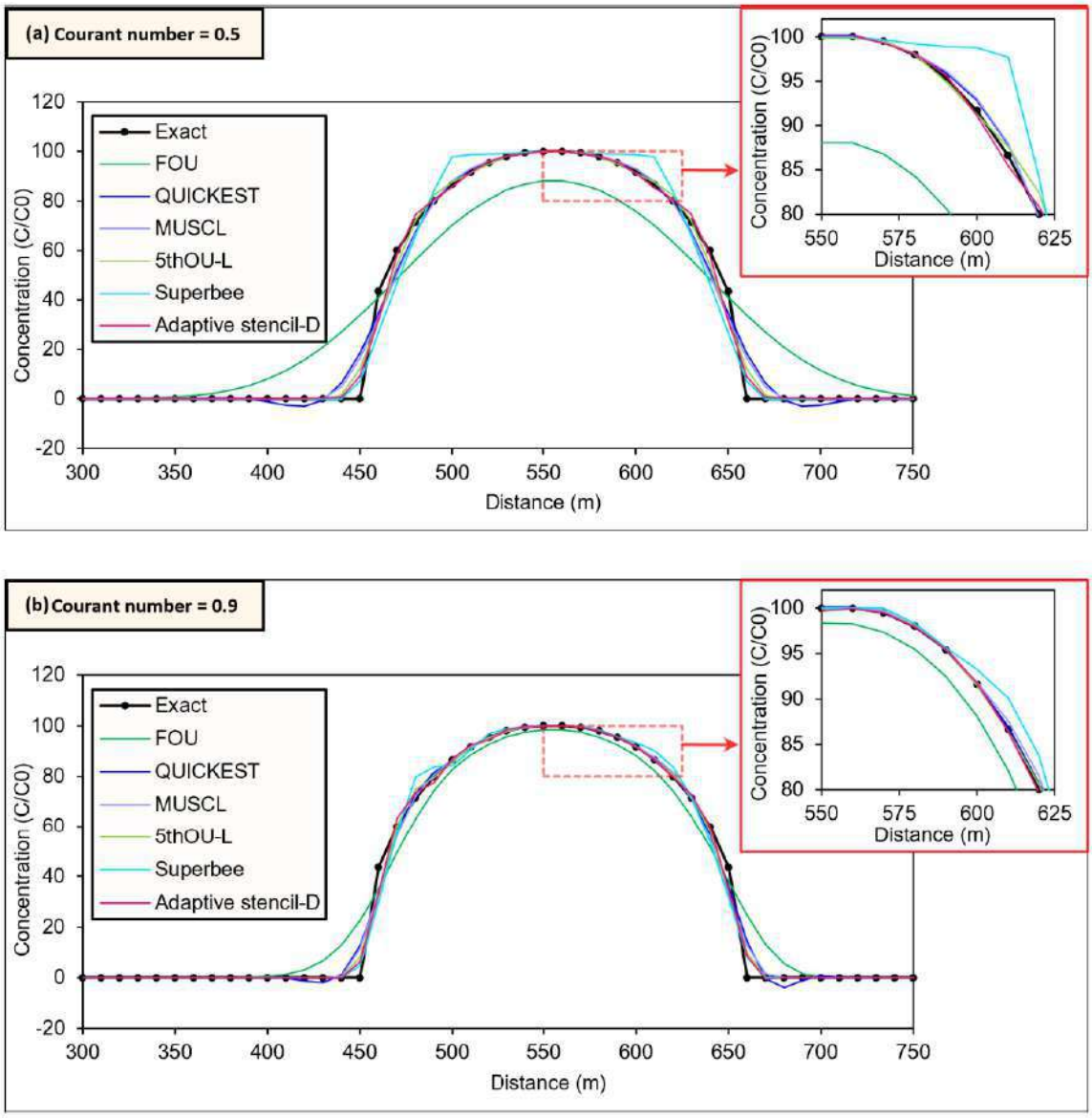

Figure 4.9 Half-circular distribution results for (a) $c_r = 0.5$, (b) $c_r = 0.9$

As a final observation of the 1D results, it can be concluded that while the selected five schemes were quite distinct from one another, still they performed much better than the FOU method. All five of these schemes were able to simulate the nine test cases within some desired level of performance irrespective of initial distribution profiles, and also irrespective of low, moderate or high courant numbers. A comparison of the error and diffusivity percentage for the FOU scheme and these five higher-order schemes is shown in figure 4.10 for c_r=0.1. Comparisons for the other two c_r values are given in Appendix figures B.1 and B.2.

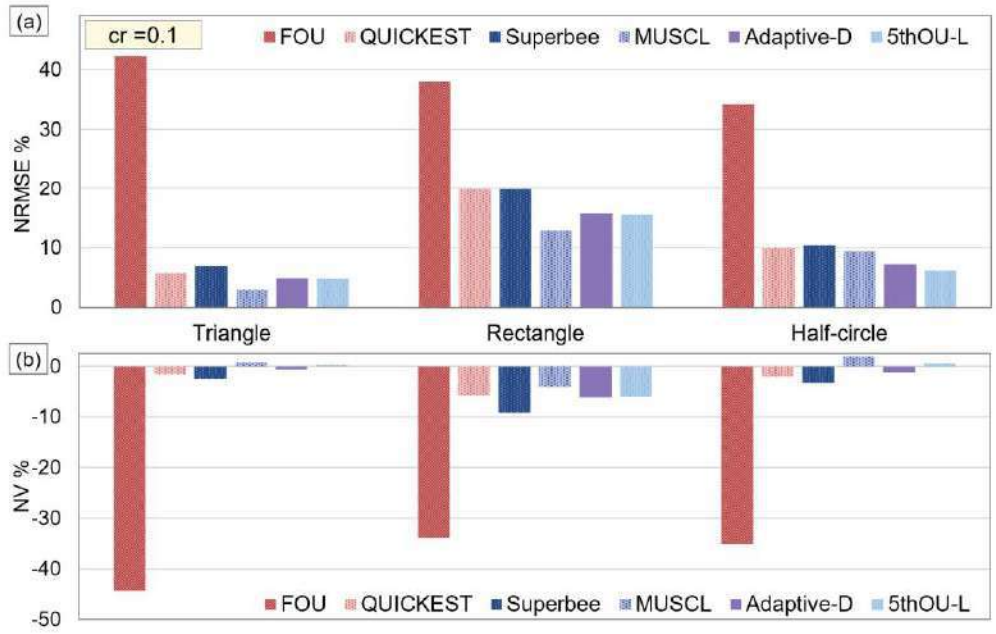

Figure 4.10 Comparison between FOU and selected higher-order methods for $c_r = 0.01$

4.2.2. Results for 2D advection

The five higher-order schemes were next used to simulate a two-dimensional advection of tracer concentration in a uniform velocity field, oblique to the horizontal direction at an angle of 45°. Velocities in both x- and y-direction were set as 1m/s

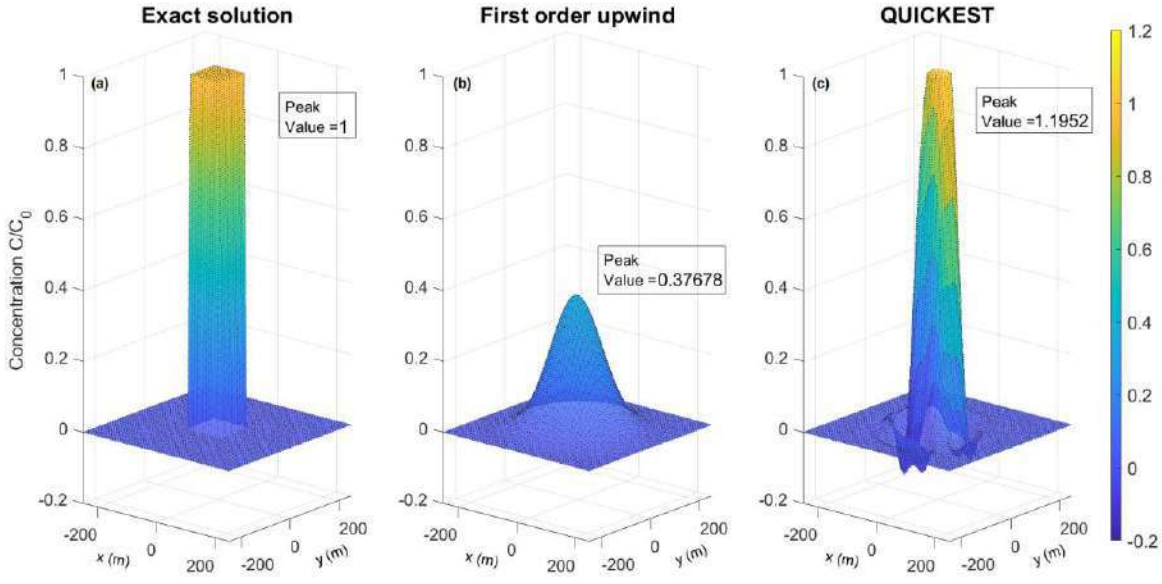

Figure 4.11 2D advection solutions (a) Exact (b) FOU (c) QUICKEST

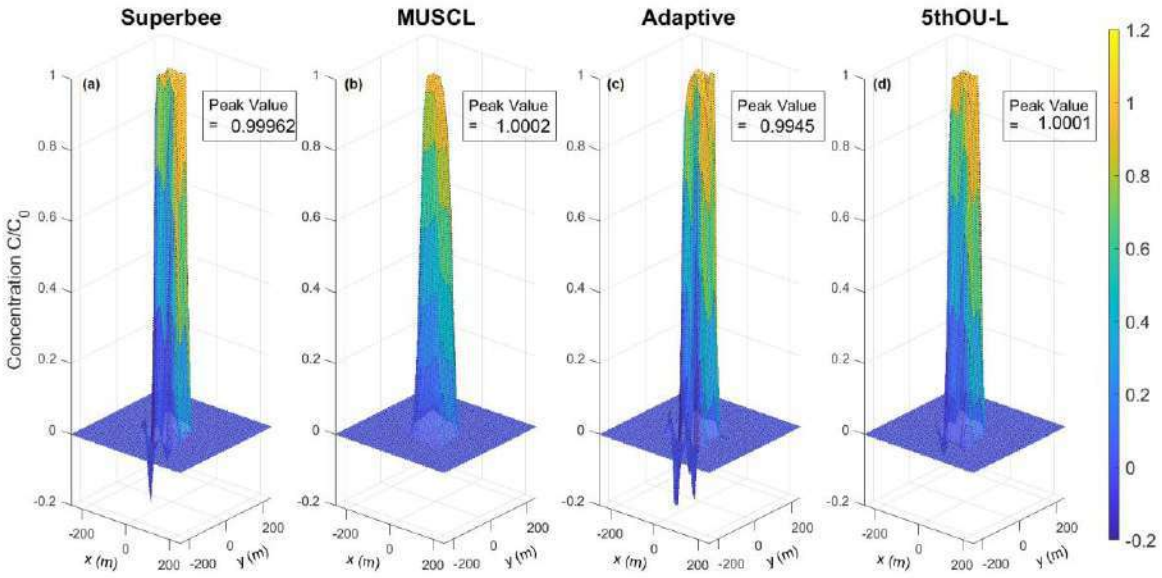

Figure 4.12 2D advection solutions (a) Superbee (b) MUSCL (c) Adaptive (d) 5thOU-L

throughout the grid. A rectangular distribution profile was chosen here for simulation, with a maxima value of 1. One of the observations from the 1D simulations was that irrespective of the initial distribution, diffusive schemes like (FOU) by default, yielded a flattened triangular shaped solution. So a rectangular shaped profile was selected for the 2D case to test the ability of the schemes to capture the sharp changes and maintain them with elapsing time. The results are displayed here for a courant number value of 0.1 and after 450s of simulation. Figures 4.11 and 4.12 show the solutions produced by all the methods. The FOU method displayed the worst performance in terms of accuracy here, only maintaining 37% of the initial peak at the end of the simulation. All of the higher-order schemes attained almost 99-100% of the maxima value. However, there

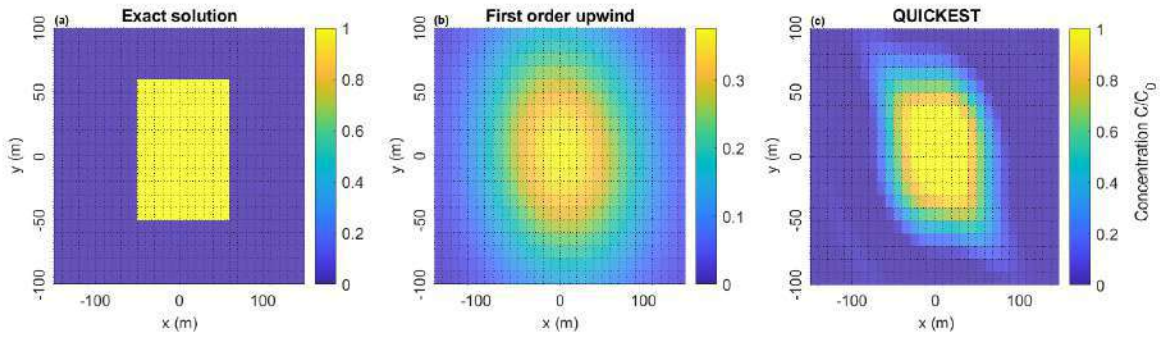

Figure 4.13 Plan view of 2D advection solutions (a) Exact (b) FOU (c) QUICKEST

were also some observations of overshoots for the QUICKEST method. Again in terms of stability, the FOU method seems to yield the most smooth solution compared to the higher-order methods. In contrast, QUICKEST, Adaptive, and Superbee solutions all have some presence of oscillations. The wiggles originated near the base of the rectangular distribution, where the slope changed sharply.

Again, figure 4.13 shows the plan view of the exact solution and the numerical solutions from the FOU and QUICKEST methods. It is evident from the result that the solution gets heavily dissipated and smeared for the FOU scheme, not maintaining the sharp edges of the exact solution. On the other hand, the QUICKEST solution does not spread so much across the grid and is comparatively more confined around the actual solution. Although the same dissipation level is not observed in the solution produced by the QUICKEST scheme, the resulting distribution seems somewhat warped. The other higher-order methods also result in similar slightly deformed plan views. So stability-wise, the FOU scheme can be considered superior to the other methods. But at the same time, the accuracy levels are much more satisfactory for the higher-order schemes. Table 4.5 gives some idea about the error and diffusivity of each of the methods observed in this 2D advection simulation. As can be seen, the NRMSE value is almost halved on average for the higher-order schemes compared to the FOU method. At the same time, the FOU scheme exhibits too much diffusivity in the 2D case as the dissipation occurs simultaneously in two directions. Whereas this limitation is considerably overcome in the higher-order methods, and the NV indices are much smaller.

Table 4.5 Results from the 2D Numerical advection test case

Scheme	**NRMSE%**	**NV%**
FOU	75.123	-80.971
QUICKEST	40.709	-15.96
Superbee	35.137	-10.826
MUSCL	39.808	-29.718
ADAPTIVE	38.453	-12.813
5THOU	35.69	-18.728

4.3. 2D coupled DA-RANS model results

The updated 2D DA-RANS model was verified with the help of two experimental test cases from literature – one being the the flow development experiment in a rectangular channel carried out by Raju et al. (2000), and the other one was a test case from Van Mierlo and de Ruiter's (1988) series of experiments for the flow field in a trench with dunes. It was also validated for the case of trascritical flow with the experimental data of Sivakumaran et at. (1983). Based on the flow over dunes test case, a larger and longer hypothetical case was developed to test the accuracy and efficiency of the higher-order schemes for increasing grid spacing. In addition to the five previously selected higher-order methods, second-order upwinding also performed considerably well in open channel flow simulations.

4.3.1. Flow development in a rectangular channel

A glass-walled flume of 15 m length, 0.75 m width and 0.5 m depth was used in this experiment of Raju et al. (2000). For the depth averaged computation, an inflow discharge of 0.0252 $m^3/s/m$ was specified at the inflow boundary. For downstream boundary, a water depth of 0.082 m was specified at the outlet. A uniform velocity profile was specified at the upstream boundary for the RANS model. A bed roughness of 0.007 was used, and a hydrostatic pressure distribution was assumed in this case. A total of 4515 nodes were used for a spacing of 0.05 m in the horizontal direction and 15 nodes in the vertical direction. The vertical node spacing was kept smaller near the bed and increased towards the water surface.

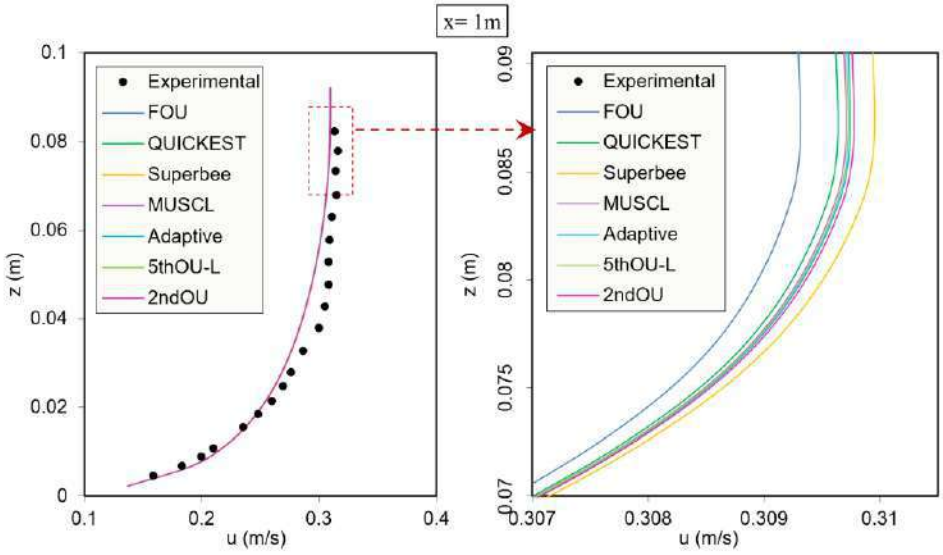

Figure 4.14 Vertical profile of longitudinal velocity for flow development in a rectangular channel

The vertical distribution of longitudinal *u* velocity at section x=1m, is shown in figure 4.14 as an example. The numerical results are presented alongside the experimental results. Only one iteration (N=1) was simulated to compare the results from the different schemes. However, the experimental setup proved to be too small to show any significant difference between the various convection methods implemented here. Overall, all the numerical results seem to underpredict the experimental results at the upper portion of the velocity profiles. Again, in an enlarged view of the profiles, the higher-order schemes appear to be closer to the experimental data, compared to the FOU method, which is the farthest. Similar results were observed for the lower portion of the velocity distribution, and in other sections as well.

4.3.2. Flow over dunes

In this experiment of Van Mierlo and de Ruiter's (1988), the flume bed was covered with sand plastered concrete having an effective roughness of 0.0025 m and effective size of 0.0016 m. The flume width in this test case was 1.5 m with a slope of 0.00094 m/m. Fixed dunes were then placed in the flume to create the trench. The dunes were of 0.08 m height and 1.6 m in length. Each of the dunes consisted of a lee side slope was 0.5 m/m, followed by a horizontal bed of 0.1 m, then a stoss side of three slopes of 0.031, 0.087 and 0.031 m/m with 0.25 m, 0.75 m and 0.26 m in length and finally ending with a horizontal bed of 0.08 m.

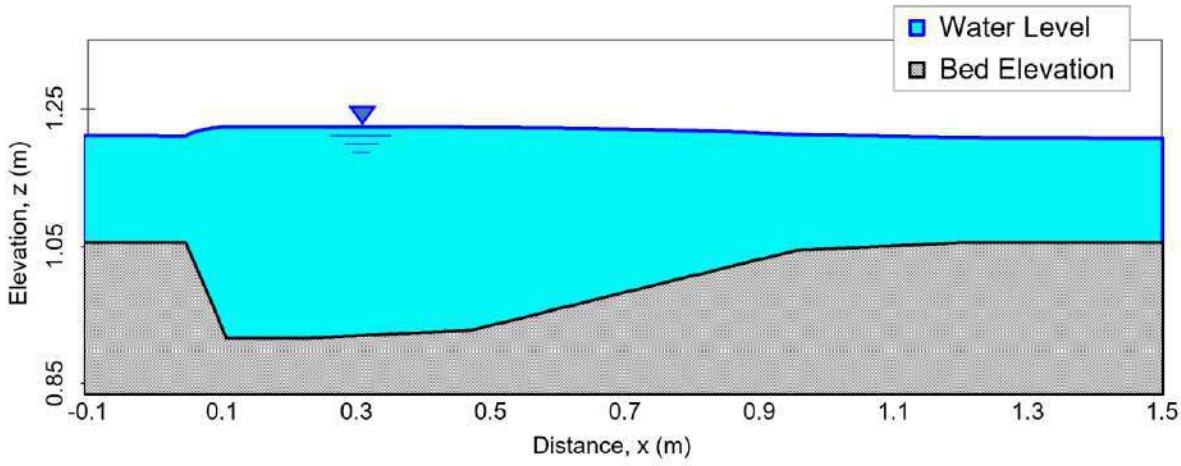

Figure 4.15 Simulated water level for flow over dunes

For verification of the current model, results of the experiment T5 of the report were used. As bathymetry of the numerical simulation, three consecutive dunes with 1 m horizontal bed in both upstream and downstream directions was generated. For upstream and downstream boundary conditions inflow discharge of 0.11 $m^3/s/m$ and a downstream depth of 0.21 m were used respectively. A horizontal spacing of 0.02 m and 30 nodes in the vertical direction were used with smaller spacing near the bed. A mesh independence analysis was also done, for spacing of 0.01 m and 40 vertical nodes, and the relative differences were found to be negligible.

The results were observed for the first iteration of the model (N=1). Figures 4.15 and 4.16 show the simulated water level and the vertical distribution profiles of the longitudinal velocity u, in different sections. All the schemes were able to predict the profiles at most sections reasonably well, except at the lee side of the dunes. This zone proves to be one of the most complicated cases to simulate since recirculation of the flow occurs. Although at the beginning of this recirculation zone, the model results are in good agreement with experimental results (at x = 0.06 m), the strength of the recirculation is underpredicted further downstream in the lee side slope. Again, in the stoss side of the dunes, the model predicted the velocity profiles quite accurately. However, this test case also provided very slight variation in the different schemes that were used, as very small horizontal spacing (0.01 ~ 0.02 m) was used, and it could not be increased without losing bathymetric information.

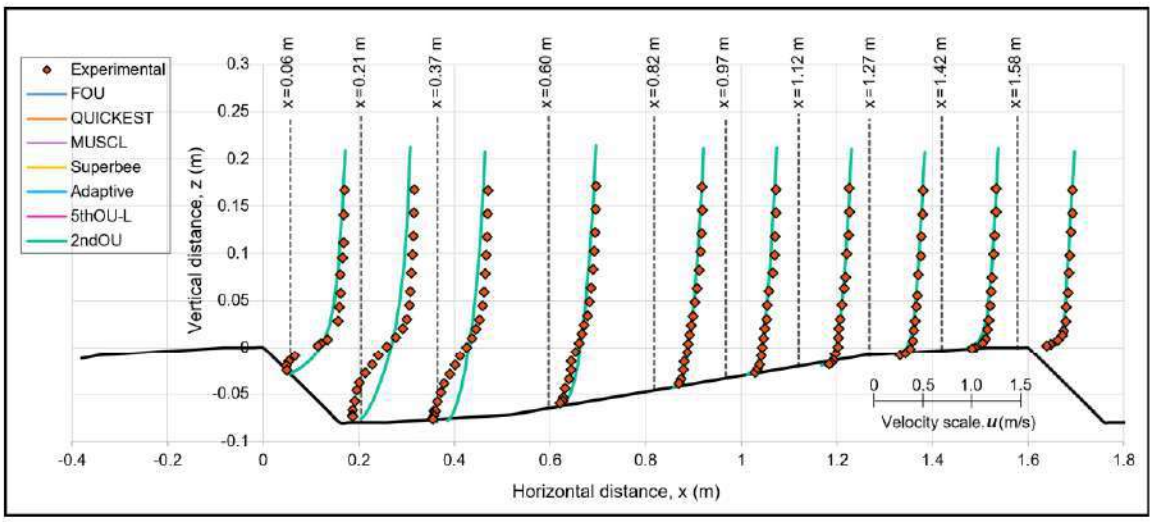

Figure 4.16 Vertical distribution profiles of longitudinal velocity for flow over dunes

4.3.3. Flow over a symmetric hump

To verify the model's performance for trascritical flow, the experimental test case of Sivakumaran et at. (1983) over a symmetric hump was used. The dimensions of the flume used in this experiment was 9.15 m × 0.3 m × 0.65 m (L×W× H). And the symmetrical hump that was provided had a length of the hump was 1.2 m and in the vertical direction it had a normal distribution with a height of 0.2 m at the center. The non-hydrostatic pressure is very significant in this case of transcritical flow where the flow transitions from a subcritical to a supercritical state. This was an important validation for the coupled DA-RANS model with higher-order schemes, to observe its ability to handle flow condition near exact criticality over the hump. Because in the upstream there is subcritical flow, the inflow boundary was set at 0.11 $m^3/s/m$ to simulate the test case. Again the in the downstream the flow condition was supercritical, and so no boundary condition was required. For the RANS model, a logarithmic velocity profile is specified at the upstream boundary. Horizontal spacing of 0.02 m and 15 nodes in the vertical direction were used in the RANS model simulation.

The simulated water level is shown in figure 4.17, and satisfactory performance is observed from the model when compared to the experimental data. The total pressure at the bottom of the channel found from the updated RANS model is compared with the available field results in figure 4.18. The model was able to predict the bed pressure

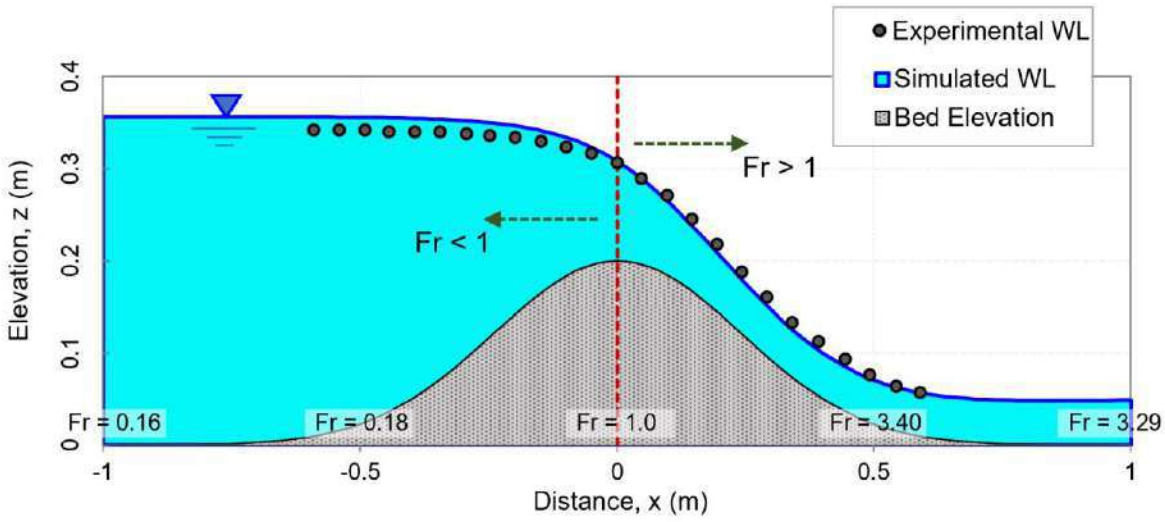

Figure 4.17 Simulated water level for flow over symmetric hump

pressure with a very good agreement between the experimental and numerical results. The hydrostatic pressure from the depth-averaged model only reflects the total water depth at the bed, which deviates considerably from the experimental data, particularly over the hump crest and immediately downstream of it. The RANS-NH model used the pressure Poisson equation and the z-momentum equation for the nodes at the channel bottom to obtain the non-hydrostatic part as well, assuming zero pressure at the water surface. The flow experiences critical depth directly over the hump, and pressure becomes significantly non-hydrostatic around the crest. The effect of NHP continues downstream for some length. From figure 4.18, it can be seen that over the crest the NHP is negative and immediately downstream of the hump crest, it becomes positive again. The non-hydrostatic pressure was estimated quite correctly and as a result the total pressure at bed were very close to the test data. Again, upstream from the hump crest, the non-hydrostatic pressure was not that significant, and the total pressure was almost same as the water level.

However, since the test case was very small in dimensions, the different schemes did not provide considerable variation in results. For horizontal spacing 0.02 m, the results became grid independent and the coarser grid resolution could not be used, as that would result in loss of the actual bathymetry data. All the higher-order schemes were able to predict the total bed pressure profile reasonably well, and were almost indistinguishable from one other.

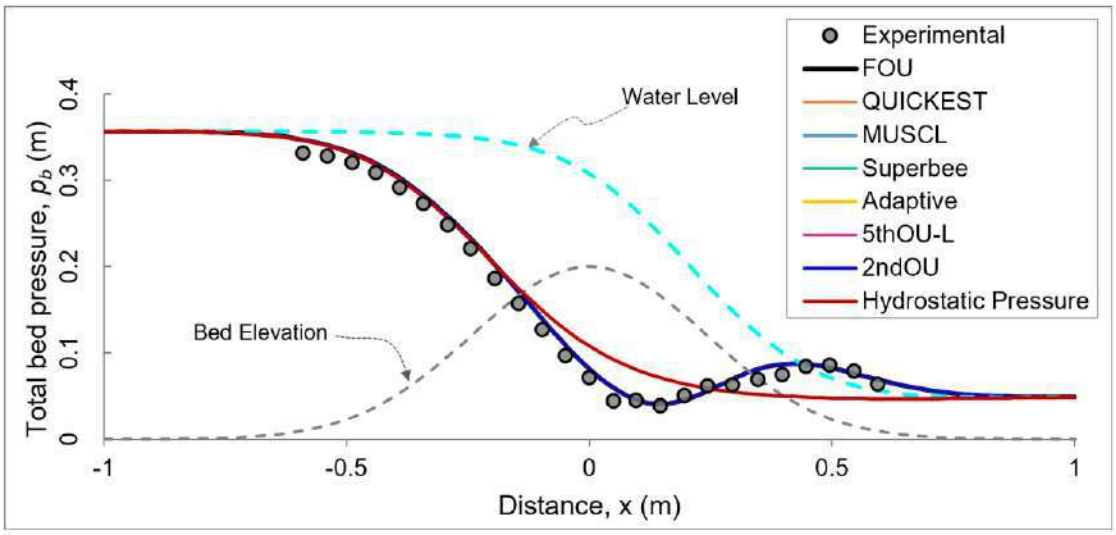

Figure 4.18 Total pressure at the channel bed of symmetric hump

4.3.4. Large scale test case

As seen in the previous two simulations, the experimental cases were found to be inadequate for efficiency analysis, as the grid coarseness could not be increased significantly. And because of that, substantial variation could not be observed between the different schemes implemented in the RANS model. Experiments carried out in laboratories were on a small scale and were limited in size and extent (most features being < 0.1 m in dimension). Larger values of space discretization Δx, would result in bathymetric features in the physical model being lost. Such numerical simulations would not be representative of the laboratory experiments. So after verification of the model with the help of experimental results, next, the model was used to simulate a hypothetical scenario of long reaches with different numerical grid coarseness in the longitudinal flow direction. The bed elevation used in this test case is shown in figure 4.19. The smallest feature of this condition was at least 20 m. And so this allowed for greater space discretization Δx values like 1 m, 2 m , 5 m, 10 m etc., and comparative performance of the advective schemes with varying grid spacing could be observed.

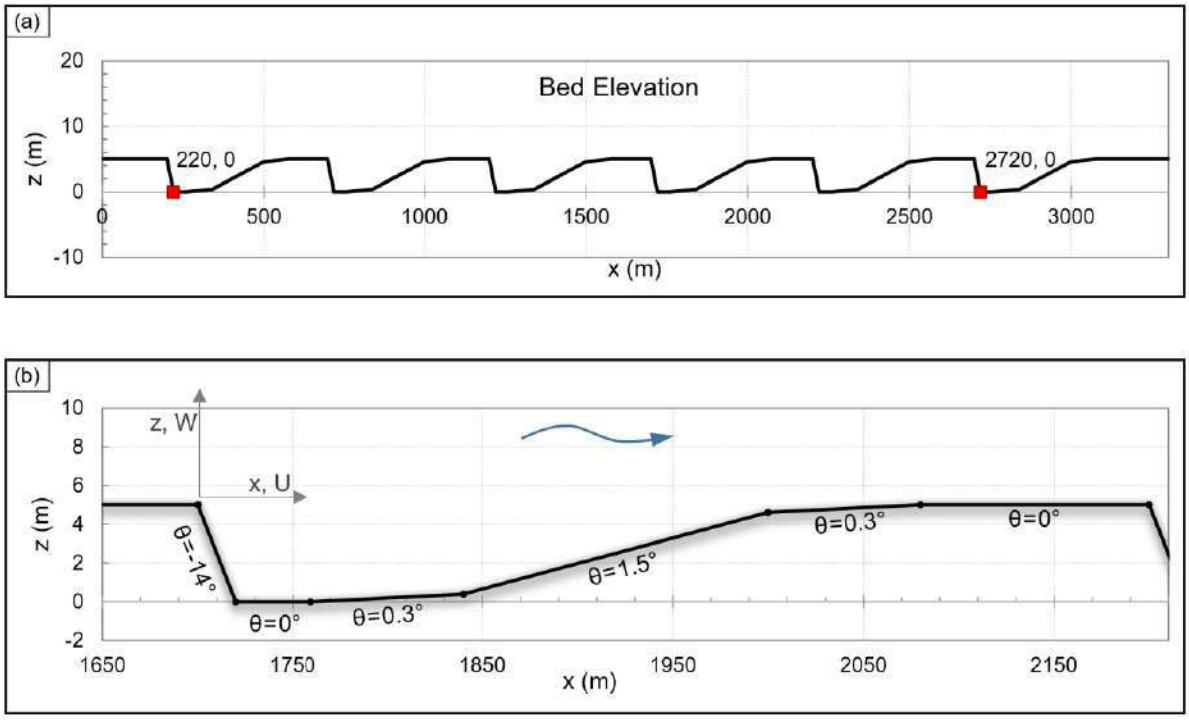

Figure 4.19 Bed elevation used for large scale test case

As observed in the simulation of the original experiment of flow over dunes in figure 4.16, the model displayed good performance in predicting the velocity profiles in the converging section of the dune, but could not reproduce the recirculation zone very well. The flow was evidently more complex in the recirculation zone, and particularly right after the downward slope, at x = 0.21 m, the simulated profile deviated most from the experimental values. So later investigations in this study focused on this recirculation zone, at x=220 m and 2720 m, as highlighted in figure 4.19(a), to see if the higher-order convective methods could perform better than first-order upwinding.

For Δx = 1 m, visually, all the schemes produced almost identical velocity profiles at the end of the lee side slope, x=220 m, as can be seen in figure 4.20(a). Considering the very long reach taken in this test case (nearly 3500 m), results at this grid size of 1 m had become mesh independent. The average of these profiles was taken as a standard of comparison for greater grid spacing. As no field data were available for this hypothetical case, the grid-independent model results were taken as a benchmark for error analysis. The results for spacing of 2 m were also very close to one another, although slight variation could be noticed in an enlarged view of figure 4.20(b). The deviation from the grid-independent profile is shown in figure 4.22(a), and the error values are quite low.

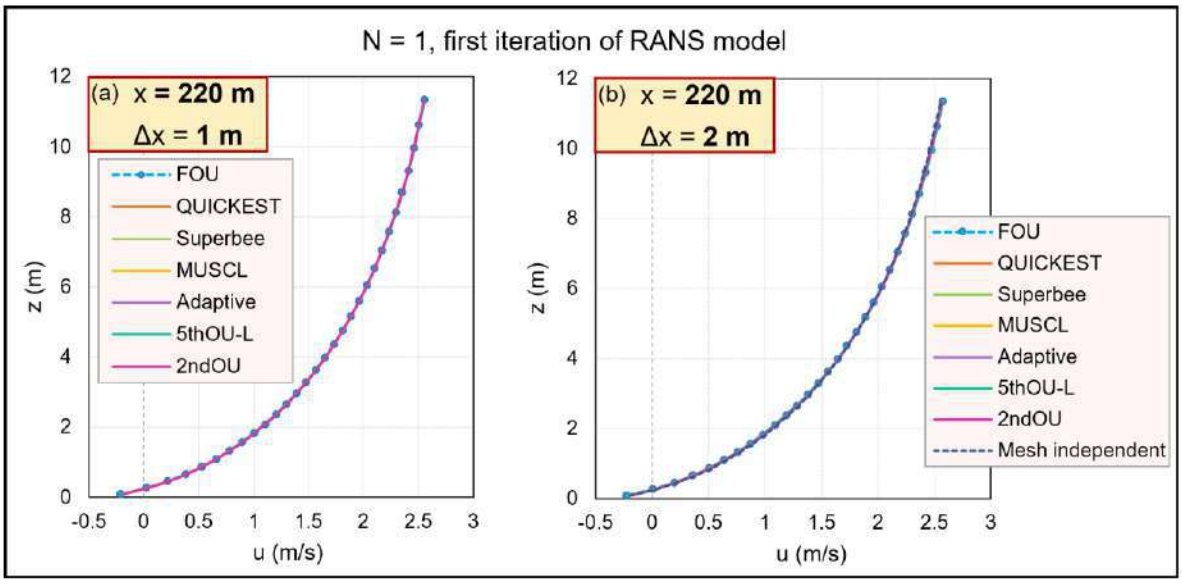

Figure 4.20 Velocity profiles at x = 220 m, for (a) Δx = 1 m (b) Δx = 2 m

The deviation from the grid-independent results becomes more apparent for as spacing is increased to $\Delta x = 5$ m, shown in figure 4.21. With larger discretization value, the profiles seem to diffuse more, and the slopes become flatter, compared to finer the grid sizes. However, all of the higher-order schemes produced results that were relatively closer to the mesh-independent results; on the other hand, the velocity profile from the FOU method was the one farthest away. The model was also used to simulate this test case for a spacing of 10 m, but the resulting velocity distributions were too diffusive, and the results are included in Appendix A and B.

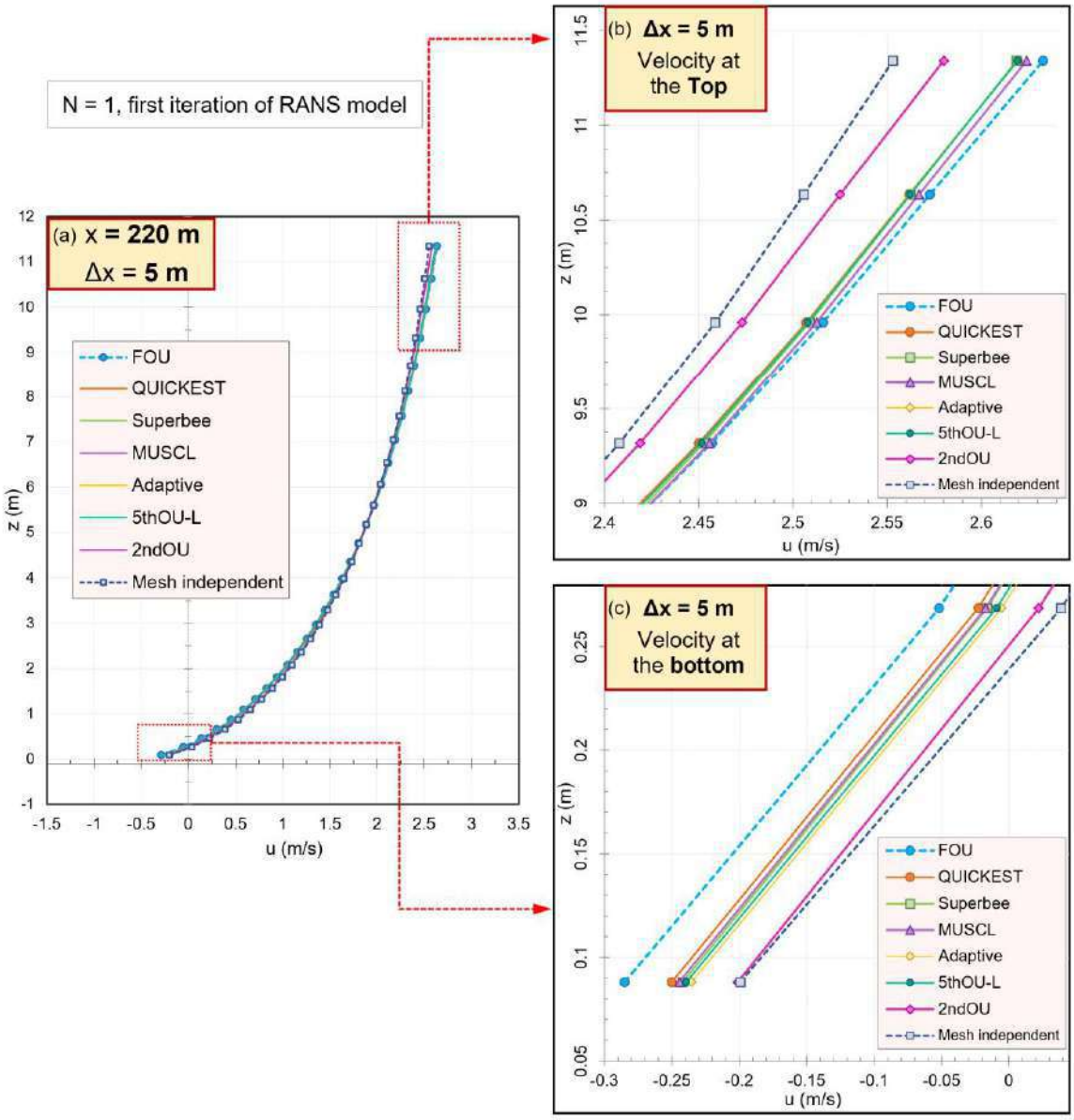

Figure 4.21 Velocity profiles at x = 220 m, for $\Delta x = 5$ m (a) complete (b) top (c) bottom portion

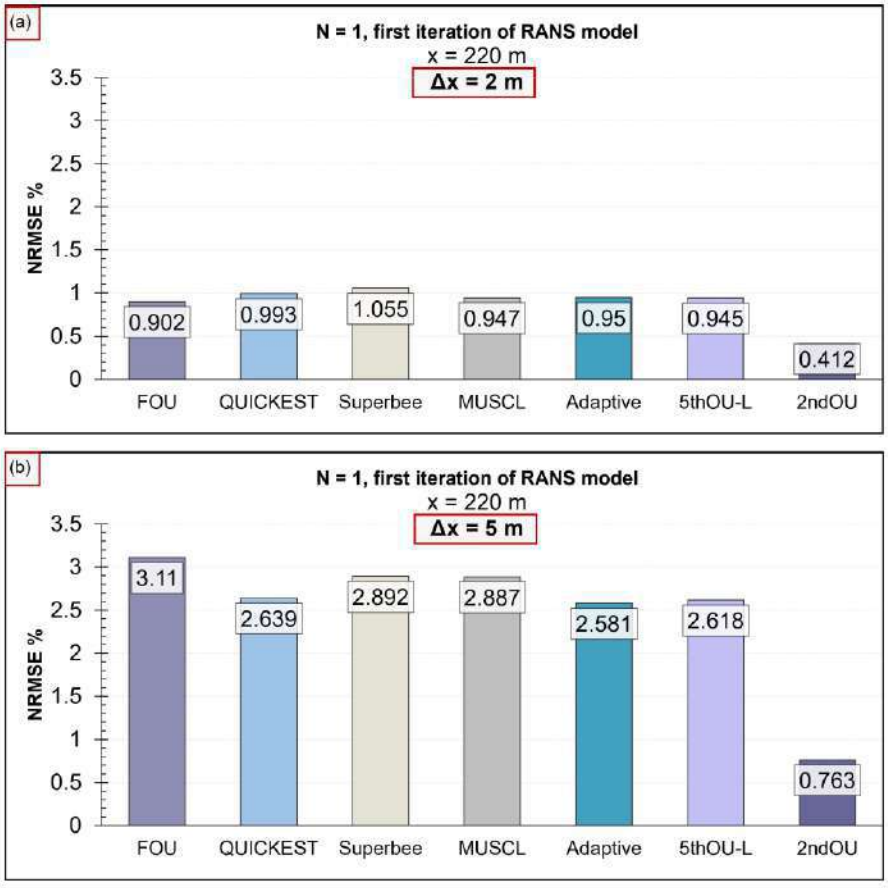

Figure 4.22 Comparison between FOU and selected higher-order methods in iteration N=1, for increased grid spacing (a) $\Delta x = 2$ m (b) $\Delta x = 5$ m

The deviations from the grid-independent profile were quantified and presented in figure 4.22. These estimated error values are helpful in assessing the improvement in the RANS model performance with the new integration of higher-order schemes compared to the original model. For grid size of 2 m, it was observed in figure 4.20(b) that all the profiles were quite close to the mesh independent result. Figure 4.22(a) reflects the same, as the NRMSE values are very small and almost similar for most schemes. As the grid size was made coarser, the errors increased as well for all the schemes. For $\Delta x = 5$ m, it can be observed from figure 4.22(b), the errors for the higher-order schemes were all lower than the corresponding errors for the FOU method. Error percentages for higher-order methods were all below 3. The second-order upwinding method performed particularly well under this test condition; its NRMSE value was only about one-fourth of (only 25%) that of the FOU method in figure 4.22(b). For the other higher-order methods, on average, there was about ~10% improvement in the simulation with 5 m spacing.

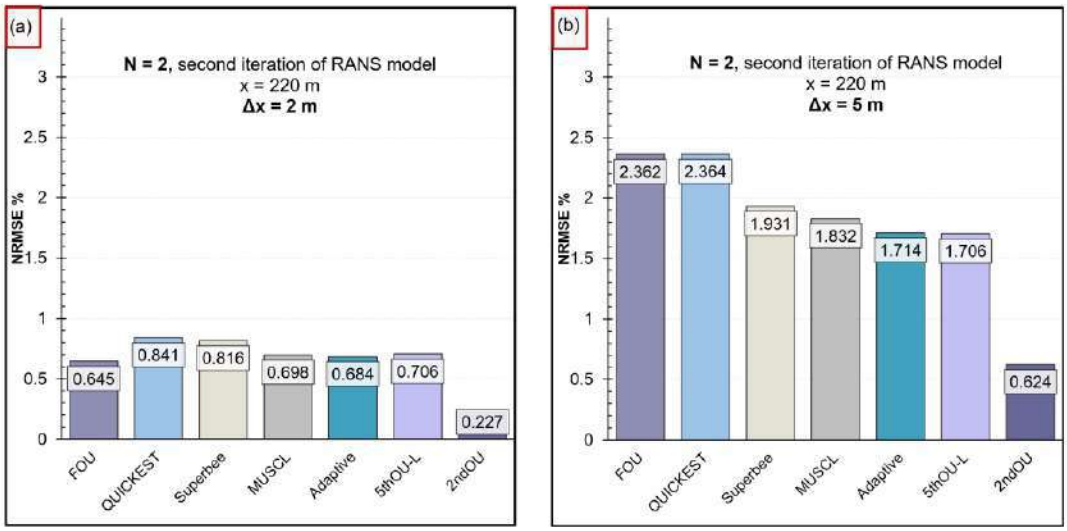

Figure 4.23 Comparison between FOU and selected higher-order methods in iteration N=2, for increased grid spacing (a) Δx = 2 m (b) Δx = 5 m

The results from the N=1 of the coupled model were next used as feedback for the second iteration (N=2), and the error values seemed to generally lower compared to the first iteration (figure 4.23). One observation from both N=1 and N=2 was that when the grid spacing is sufficiently small, the FOU method could be the more efficient choice, as the deviations for higher-order methods were slightly greater. However, when the discretization is made larger, the higher-order schemes were clearly producing

Table 4.6 Ranking of the selected higher-order schemes for the coupled 2D model

Scheme Name	NRMSE (%)		Rank based on least error produced
	N = 1	N = 2	
FOU	3.110	2.362	8
QUICKEST	2.639	2.364	7
QUICKEST-L	2.899	1.796	4
Superbee	2.892	1.931	6
MUSCL	2.887	1.832	5
Adaptive	2.581	1.714	2
5thOU-L	2.618	1.706	3
2ndOU	0.763	0.624	1

less errors, as shown in figure 4.23(b). The second-order upwinding method resulted in the least deviation from the grid-independent profile for N=2 as well. The QUICKEST scheme was the only one that surpassed FOU in terms of NRMSE, but this was only because this version was used without any flux limiters. This was done deliberately to observe the effects of limiter functions in higher-order schemes for OCF models, and the absence of limiters seems to have worsened the deviation compared to first-order upwinding. The QUICKEST-L scheme (with limiter) resulted in a NRMSE value of 1.796. The rest of the higher-order methods resulted in 20-30% better results than the FOU scheme. A ranking of the performance of the schemes based on the error percentage is shown in table 4.6 for the 5 m grid spacing. Similar results were observed for x=2720 m, location. Results for this location are presented in Appendix A and B.

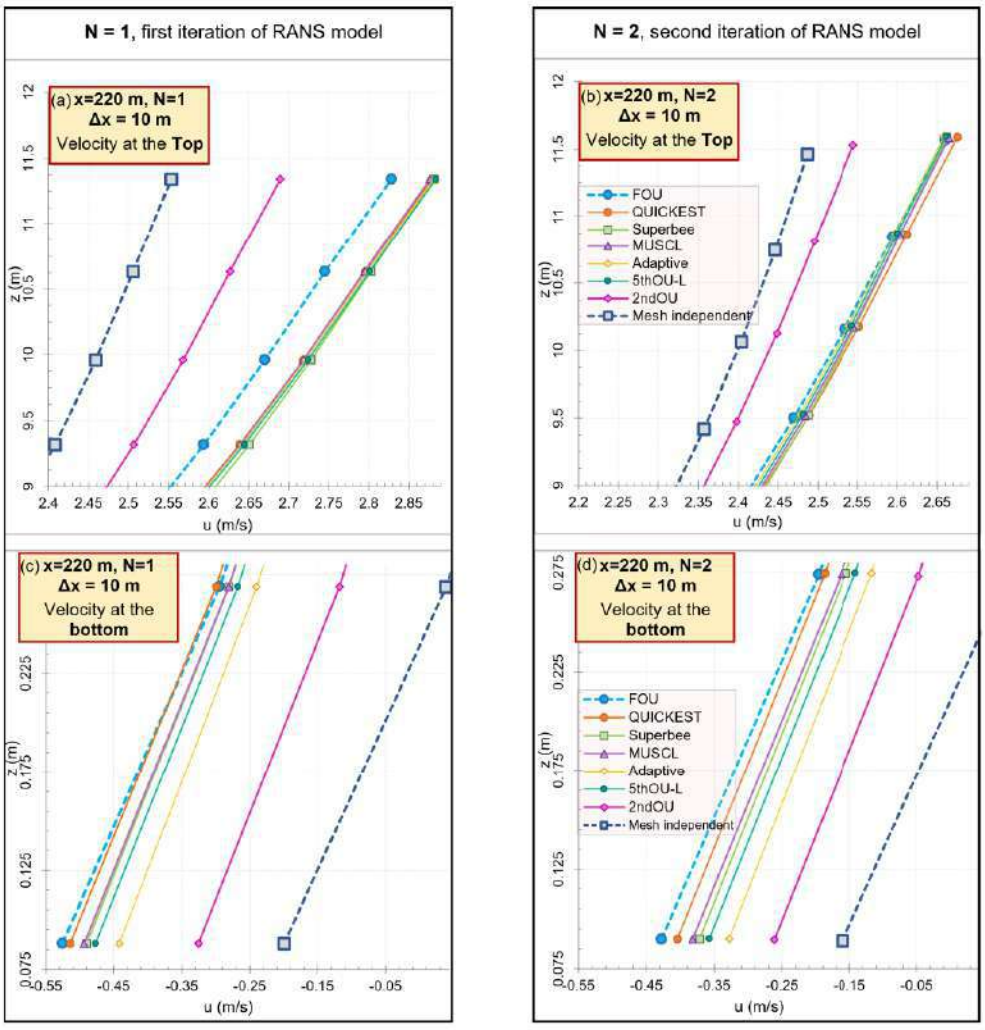

Figure 4.24 Velocity profiles at for Δx = 10 m, at the top (a) N=1 (b) N=2; at the bottom (c) N=1 (d) N=2

Although for the test case where discretization value of $\Delta x = 10$ m was used, the resulting velocity profiles experienced a lot of diffusion overall, but in the near-bed region of the flow, the higher-order schemes still out-performed the FOU method. In figure 4.24, enlarged view of the top and bottom velocity profiles are shown for grid spacing of 10 m, both for the first and second iteration of the coupled DA-RANS model. It can be seen that for coarser grid, most higher-order schemes experience worse dissipation compared to the FOU method. But in the lower parts of the velocity profile, all higher-order schemes are closer to the grid-independent results, and first-order upwinding profile is the one farthest away. Based on these outcomes, it can be inferred that higher-order differencing methods are better-equipped to simulate near-bed properties of the flow.

Figure 4.25 shows the velocity distributions specifically for the lower portions of the water depth for a spacing of 5 m. The near-bed velocity profiles are not as dissipated, as observed for 10 m discretization (figure 4.24), and approximated the mesh independent solution very closely. The NRMSE values are also included in figure 4.25, and the higher-order schemes yield comparatively lower errors. The second-order upwinding method again performed the best in this 2D long reach scenario. The bed velocity along the whole channel bed longitudinally is shown in figure 4.26. Since for $\Delta x = 5$ m, the accuracy of the model did not suffer as much diffusion and yet reduced the computational time by 5 times than the grid-independent result, a comparison between first- and second-order upwinding is presented here.

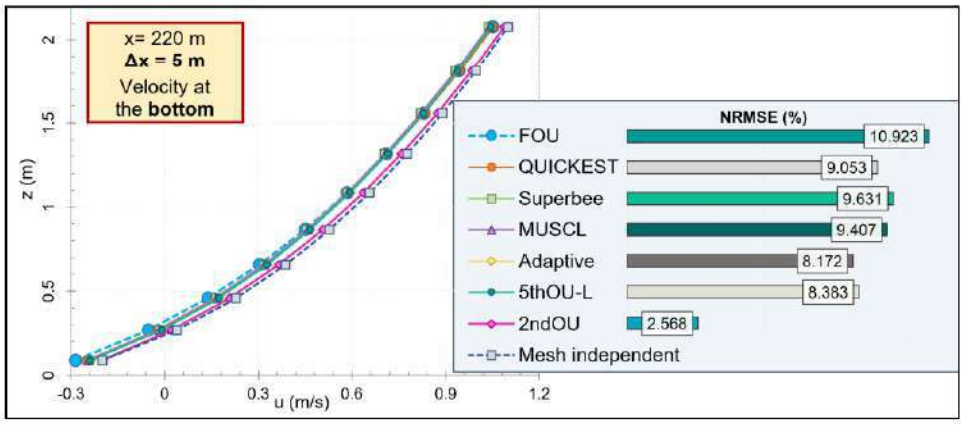

Figure 4.25 Near-bed velocity profiles for $\Delta x = 5$ m

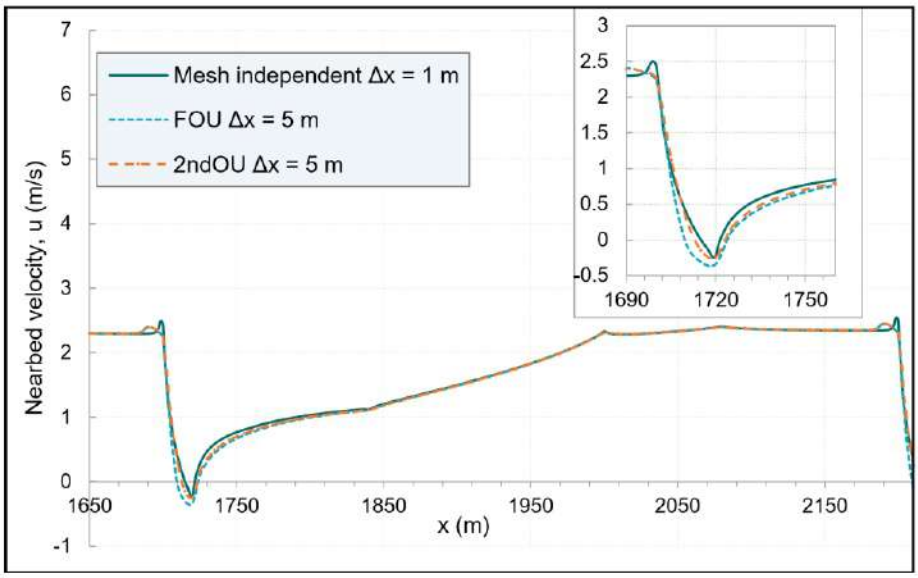

Figure 4.26 Near-bed velocity along the channel bed (longitudinal direction)

Computational efforts required by the coupled model also varied a great deal, as grid coarseness was changed. The number of iterations required for the 2D model to achieve identical convergence conditions for different grid sizes is presented in tables 4.7 and 4.8. Here, n_{its} = number of iterations required for the model to converge

Table 4.7 Convergence of coupled 2D model in N=1, for varying grid coarseness

N=1	Convergence steps (n_{its})				
	DA model	RANS model			
		Δx = 1 m	**Δx = 2 m**	**Δx = 5 m**	**Δx = 10 m**
FOU	84103	624	294	108	51
QUICKEST		625	295	111	51
Superbee		625	295	109	52
MUSCL		625	295	109	52
Adaptive		625	295	109	52
5thOU		696	299	109	52
2ndOU		625	295	109	52

*Note: here, n_{its} = Number of iterations required for the model to converge (residual $\leq 10^{-4}$)

Table 4.8 Convergence of coupled 2D model in N=2, for varying grid coarseness

N=2	Convergence steps (n_{its})							
	Δx = 1 m		**Δx = 2 m**		**Δx = 5 m**		**Δx = 10 m**	
	DA	RANS	DA	RANS	DA	RANS	DA	RANS
FOU	55315	230	30394	103	7166	39	4925	25
QUICKEST	55335	230	30407	101	11687	35	5742	28
Superbee	37365	228	30408	100	12025	38	4911	29
MUSCL	55335	228	30406	101	7502	39	5746	28
Adaptive	55332	300	30407	112	7181	38	3695	29
5thOU	55336	227	30407	101	7180	38	3695	29
2ndOU	55336	233	30412	103	7512	35	3923	29

*Note: here, n_{its} = Number of iterations required for the model to converge (residual ≤ 10^{-4})

(residual ≤ 10^{-4}). Initially, the DA model results were taken for Δx = 1 m in the first iteration of the model (N=1), for all schemes, and the model converged in 84103 steps. The RANS model achieved convergence in 625, 295, 109 and 52 steps on average, for 1 m, 2 m, 5 m and 10 m grid size respectively. This reduction of computational efforts with increasing grid sizes is displayed in figure 4.27(a).

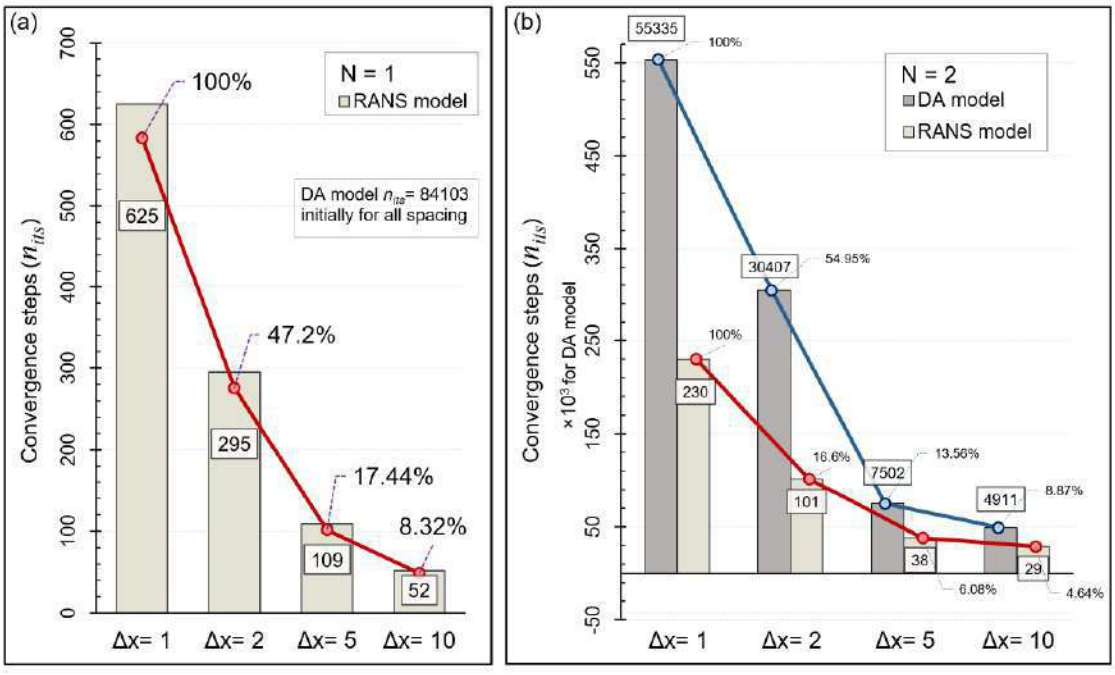

Figure 4.27 Comparison of iteration steps to convergence for different grid sizes

Although the steps reduction is the greatest for 10 m spacing (almost 92% lower than the grid-independent simulation at $\Delta x = 1$ m), the accuracy of the model for this test condition was found to be very diffusive and not very accurate. On the other hand, $\Delta x = 5$ m in the RANS model produced results for the higher-order schemes that not only deviated very little from the grid-independent results but also reduced the computational efforts by about 83%. The second-order upwinding method, in particular, had an error percentage of only 0.6 ~ 0.7 for 5 m spacing, and at the same time this larger discretization reduced the convergence steps to 17.44% of the original mesh independent simulation.

Again, to attain the same level of accuracy from the original RANS model with first-order upwinding, it would not be possible to increase grid size beyond 1 m and the saved computational efforts would be nil in that case. In N=2, convergence steps in both DA and RANS models reduced with gradually coarsening the numerical grid, as observed in figure 4.27(b). From these findings, it can be inferred that the higher-order schemes would yield much better results in terms of both accuracy and computational efficiency up to some optimal value of grid spacing. Although the CPU efforts would still continue to drop beyond this optimum discretization, the numerical diffusion becomes too large, thus negatively affecting the accuracy of the simulation.

Overall, among all the higher-order advective schemes, the second-order upwinding method appeared to be the most suitable for the test cases simulated using the coupled 2D DA-RANS model. It produced the least NRMSE values, and the error did not grow that significantly, even as the grid coarseness was increased. Another larger hypothetical test case was simulated for the FOU and 2ndOU methods for further investigation, and the resulting velocity profiles were compared for $\Delta x = 5$ m and 10 m (Appendix figure B.8). The profiles for 5 m spacing from both schemes were very close to one another. The convergence steps n_{its}, reduced by more than 50% as the spacing was changed from 5 m to 10 m. The 2ndOU scheme at $\Delta x = 10$ m approximated the results of the finer resolution considerably well; whereas the FOU method clearly deviated much further away as the grid was more coarsely discretized. The second-order upwinding was able to maintain its accuracy even at greater Δx values, and the same time did so by saving computational efforts substantially.

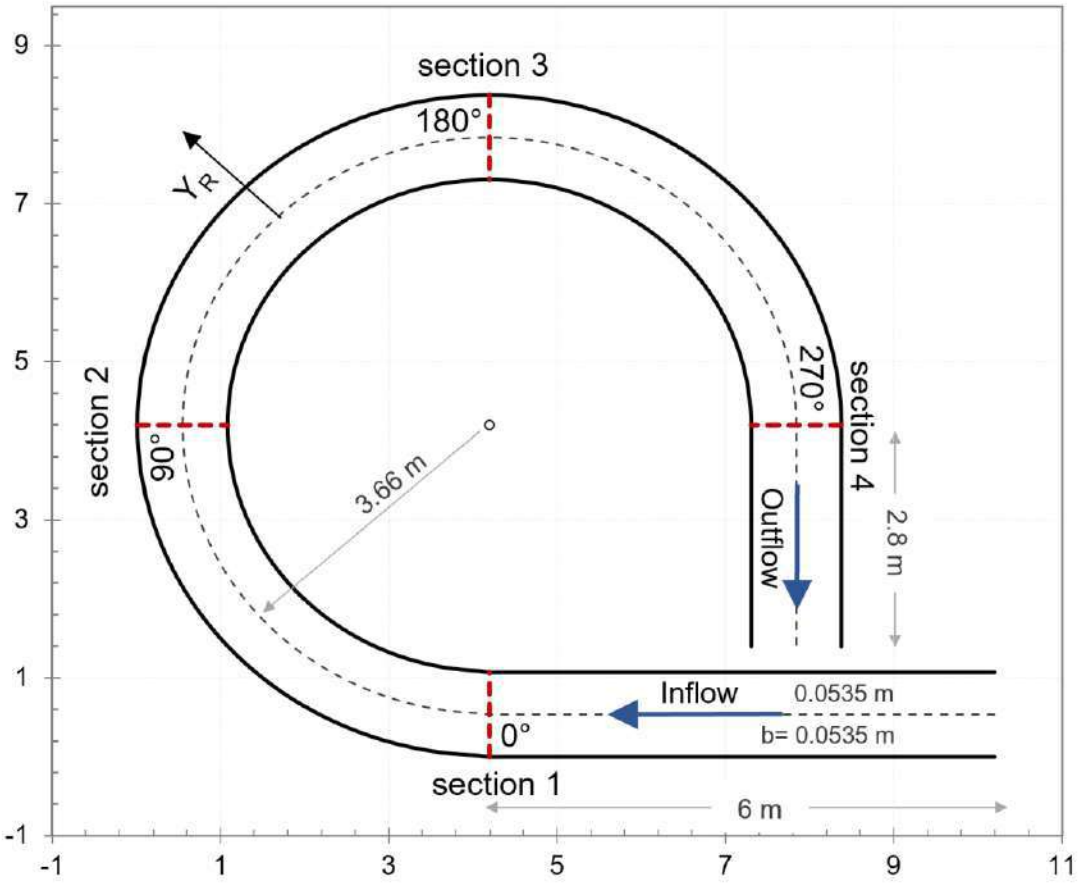

Figure 4.28 Top view of layout for flow in curved channel

4.4. 3D coupled DA-RANS model results

Once the higher-order schemes were found to produce sufficiently stable and accurate results in the 2D flow simulations, they were then implemented into the more complex three-dimensional open channel flow model. The newly updated coupled 3D DA-RANS model was used to simulate two different experimental flow conditions – Steffler's (1984) turbulent flow in a curved rectangular channel and the three-dimensional version of Van Mierlo and de Ruiter's (1988) experiment of flow over dunes. The simulated velocity profiles were compared with experimental results for model verification. Test cases of sufficiently large dimensions were simulated to compare the accuracy and computational efficiency between the different higher-order advection schemes used.

4.4.1. Flow in a curved channel

In this test case, closely following the experiment of Steffler (1984), a 270° bend with a 3.66 m radius of the centerline was used. The curvature of the bend was moderate, $R_c/2b \approx 3.4$. The flume was 1.07 m wide, with 0.21 m depth, a 6 m long straight inlet and a 2.8 m long outlet sections. The layout of the experimental setup is shown in figure 4.28. The bed slope in the flume was set at a value of 0.00083, and a 0.0013 m roughness height was used. After sensitivity analysis was done for several meshes, finally a mesh of 180×21×15 was selected for verification. This resulted in a total of 3780 nodes for the DA model and 56700 nodes for the RANS model. Boundary conditions used were an inflow of 0.0224 m^3/s discharge and a constant depth of 0.061 m at the exit. The complete bed elevation is included in Appendix B.

The computed longitudinal velocity (u_L) and transverse velocity (u_T) profiles from the coupled model at N=3 are shown in figures 4.29 and 4.30 respectively. The profiles are in good agreement with the experimental result in the middle of the channel. In the regions near the sides, the simulated velocities show some deviation from the experimental profile.

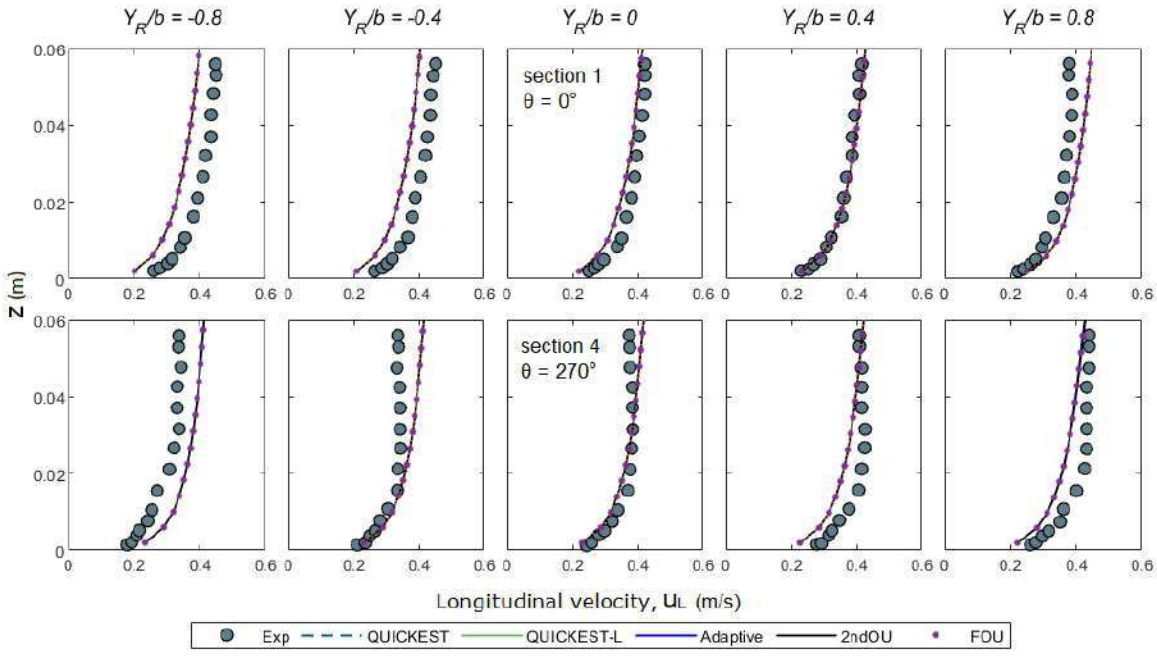

Figure 4.29 Longitudinal velocity at sections 1 and 4 for the curved channel test case

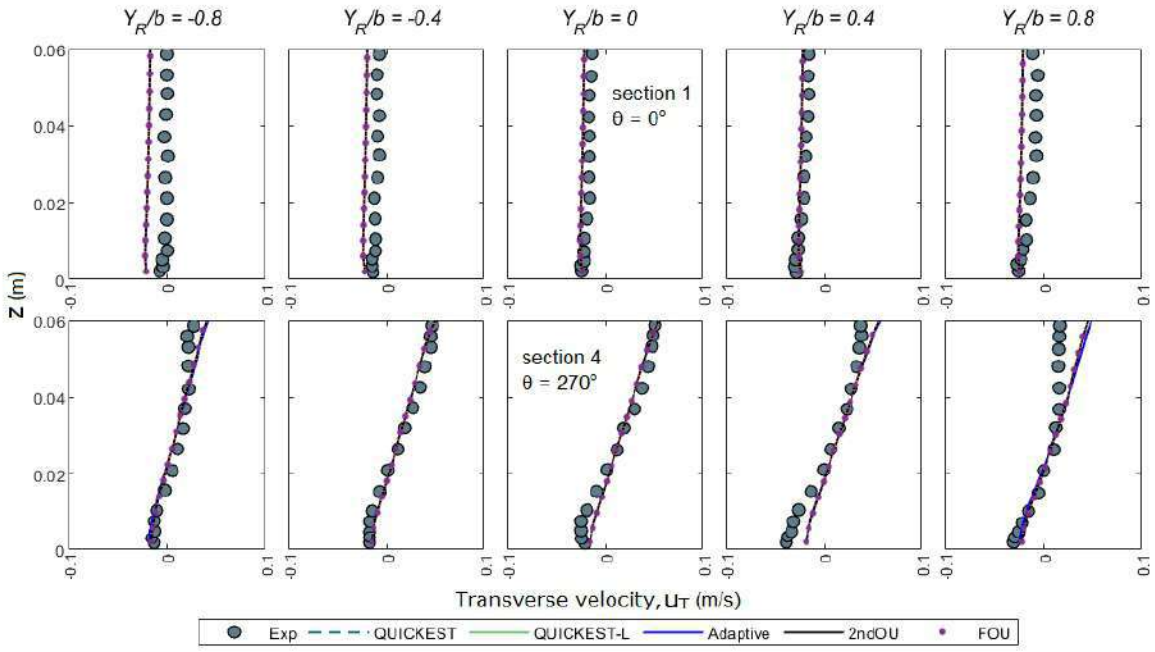

Figure 4.30 Transverse velocity at sections 1 and 4 for the curved channel test case

A closer look at the velocity profiles showed that the simulated velocity from the higher-order schemes were nearer to the experimental values, even if by a slight margin. The performances of the Adaptive stencil and 2ndOU method were found to be superior in the pure advection and two-dimensional cases respectively. These two schemes were used in this 3D simulation. Again, the Adaptive stencil is quite similar to the QUICKEST scheme in regions with minimal gradient changes. The stencil switches to seventh/ninth order Leonard's TIM discretization where discontinuities are present and if applicable; in other locations, the third order QUICKEST scheme is used. However, implementing such high order of discretization may appear to be overly complex in some cases. Again, as observed previously, only using the QUICKEST scheme without limiter introduces oscillations to the solution. The QUIKCKEST-L scheme provides a much better choice, since the accuracy improves as the limiter is activated, and the scheme is easier to implement than the Adaptive stencil. QUICKEST-L method also appear to be closer to the experimental data in the enlarged velocity profile in figure 4.31 than the 2ndOU scheme. The results from this test case, though substantially verified the performance of the updated 3D coupled DA-RANS model,

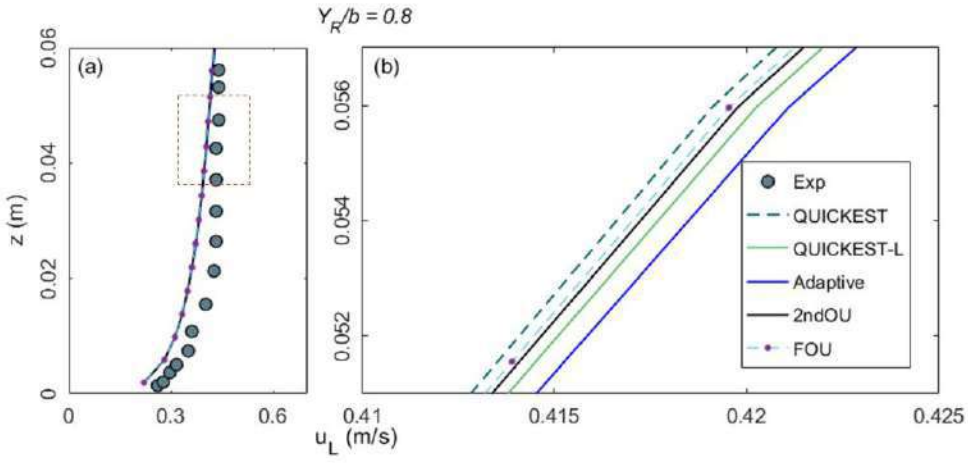

Figure 4.31 Longitudinal velocity at section 4 for $Y_R/b = 0.8$ (a) complete profile (b) enlarged view

could not provide prominent differences between the schemes as the experimental setup itself was very limited in dimension and as such discretization values had to be kept very small as well.

4.4.2. Flow field in a trench

A three-dimensional version of Van Mierlo and de Ruiter's (1988) series of experiments for the flow field in a trench with dunes is used for this test case. Previously the 2D plane flow simulation for this condition was observed in section 4.3.2. Similar boundary conditions, longitudinal spacing and vertical node numbers used for the 3D simulation. In the transverse direction 0.15 m spacing was chosen, resulting in a grid size of 341×11×30. In the transverse direction, the velocity is very minimal since the flow direction is without any bends or curves in this scenario. The longitudinal profiles on the other hand, vary considerably from the 2D model at corresponding sections. Figure 4.32 show the vertical distribution profile of the longitudinal velocity at the section, x=0.6 m. Especially near the bottom, the FOU method deviates the most from the experimental profile. The Adaptive and QUICKEST-L schemes produce almost graphically indistinguishable results. And although still better than FOU, the deviation from 2ndOU was greater, despite being the most accurate one in the 2D cases.

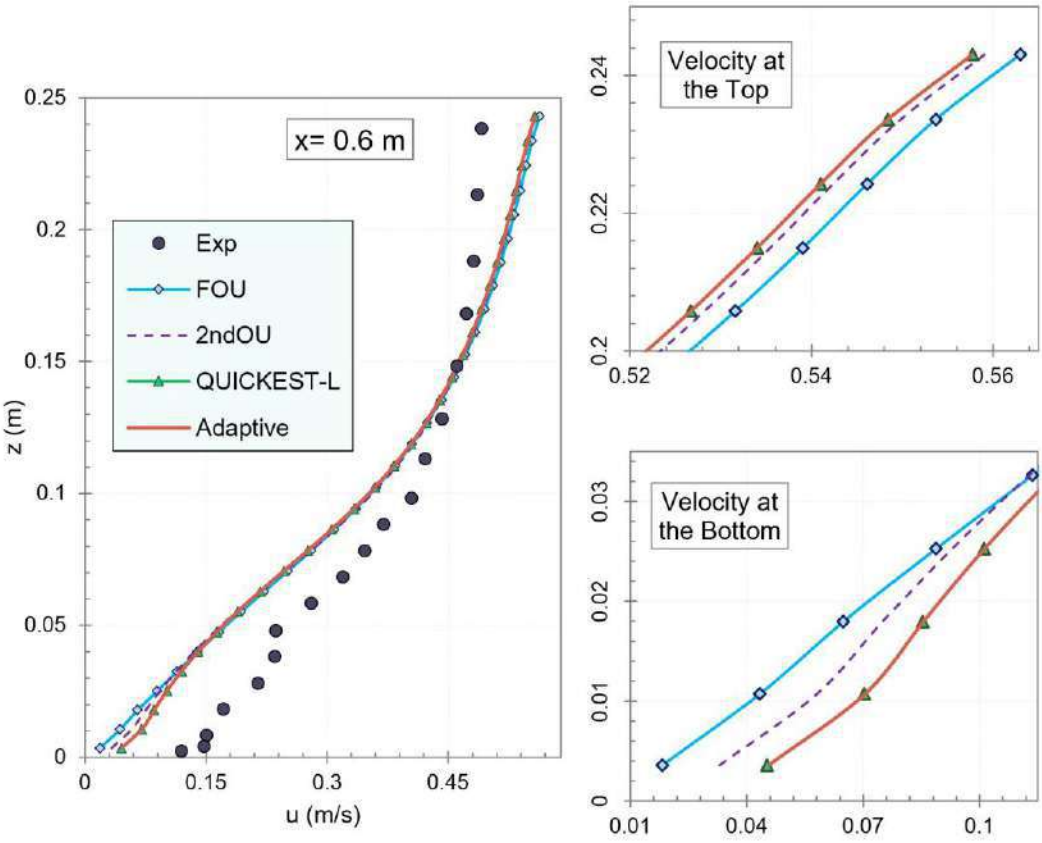

Figure 4.32 Vertical distribution profile of longitudinal velocity for Flow field in a trench

4.4.3. 3D test case of long reaches

As experienced in the two-dimensional experimental cases, in the 3D case similarly the experimental setup and its features were so small itself that the spacing could not be increased significantly without losing the setup's bathymetric information. Long reaches were designed (on the basis of the flow field in trench scenario), were larger values of space discretization Δx and Δy could be used. This allowed for the model to be tested for varying grid coarseness. Since no field data were available for the hypothetical cases, the grid-independent model results were taken as a benchmark for error analysis. A comparative analysis was then done between the increased savings in computational time and the associated reductions in the accuracy of flow variables

with gradual coarsening of the numerical grid. From the results of the experimental test case simulations, it was found that QUICKEST with limiter with its third order accuracy was the more optimum choice among the all the other higher-order schemes tested in the 3D model. The rest of the comparisons were made between FOU and QUICKEST-L schemes in the large-scale test cases for mesh spacing of 1 m, 2 m, 5 m, and 10 m. Two such long reaches were designed for testing the higher-order schemes.

4.4.3.1. Horizontal reach

This reach was very similar to the 2D flow over dunes test case. An additional width of 5 m was considered here in the transverse direction (bed elevation shown in Appendix figure B11). The discharge along the channel was kept in the horizontal direction only, and for that reason the variation along the transverse was very negligible. The longitudinal velocity distribution for this test case can be seen in figures 4.33 and 4.34. The smallest grid size used here was 1 m, and both for FOU and QUICKEST-L, the results were visually almost indistinguishable. The average of the two distributions for grid size of 1 m, was taken as benchmark value and the error analysis was done with respect to it.

The NRMSE percentages for different grid coarseness is shown in figure 4.35. As spacing was doubled to $\Delta x (= \Delta y) = 2$ m, the profiles were still very close, however for the FOU scheme there were some deviations in the bottom portion of the velocity distribution. Nevertheless, the NRMSE value for both the schemes were quite small, and roughly in the range 0.5 ~ 1. The average convergence step, n_{its} was almost halved (from 3051 to 1463) as the coarseness was doubled, as can be seen in figure 4.33 (details shown in Appendix table A.3). The difference between first-order and higher-order methods become more prominent for 5 m grid coarseness. The QUICKEST-L scheme performed considerably better than FOU scheme, and this was evident both from the graphical representation of the velocity profiles, as well as the NRMSE values. While the profile for higher-order scheme deviated by a very small margin for spacing $\Delta x (= \Delta y) = 5$ m, the first-order method resulted in a significantly large deviation from the grid-independent profile. Especially in the near-bed region the higher-order method

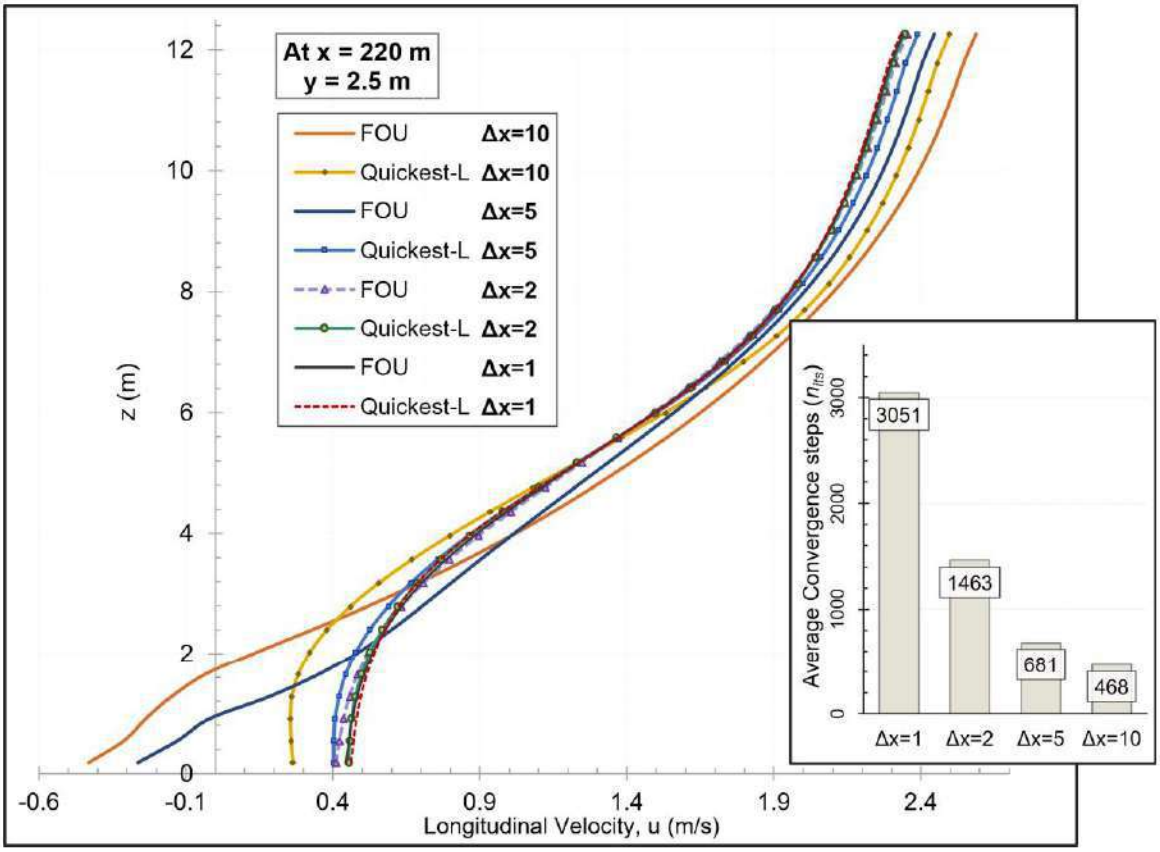

Figure 4.33 Longitudinal velocity distribution for 3D horizontal long reach test case

*Note: here, Δy = Δx in each corresponding condition

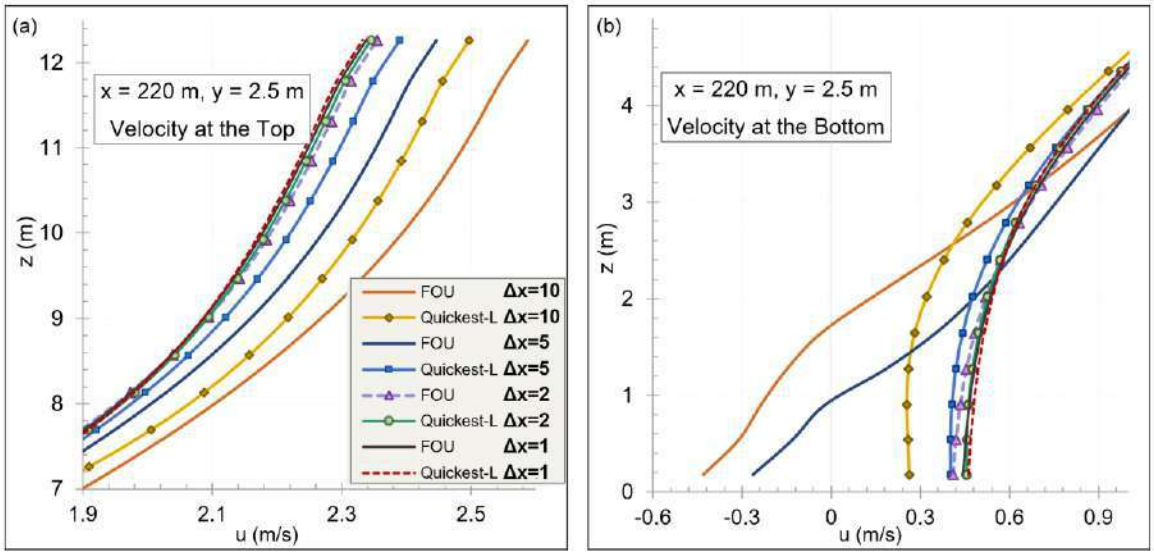

Figure 4.34 Longitudinal velocity at (a) top (b) bottom, for 3D horizontal long reach

*Note: here, Δy = Δx in each corresponding condition

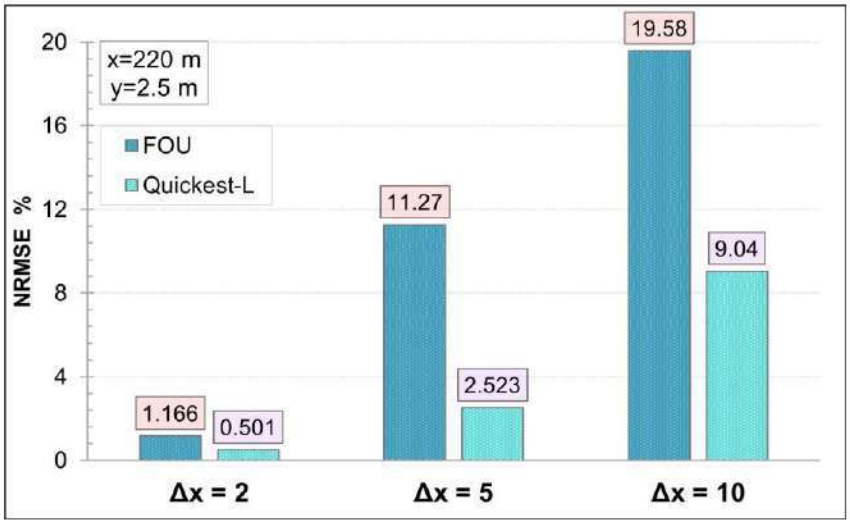

Figure 4.35 Error comparison for 3D horizontal long reach

*Note: here, Δy = Δx in each corresponding condition

substantially out-performed the FOU scheme. Overall, the NRMSE value for QUICKEST-L was 2.52, whereas for the first-order method it was 11.27. This indicated an improvement of almost 80% from the original model's performance by incorporating higher-order advective discretization. At the same time the required computational efforts lowered by almost 5 times (n_{its} = 681).

Table 4.9 Ranking of the selected higher-order schemes for the 3D coupled model (horizontal reach)

Scheme Name	NRMSE (%)		Rank based on least error produced
	Longitudinal direction		
	Δx = 5 m	Δx = 10 m	
FOU	11.71	21.82	5
QUICKEST	3.895	11.774	3
QUICKEST-L	3.39	12.56	1
Adaptive	3.104	12.576	2
2ndOU	4.482	25.529	4

Similar results were observed for 10 m discretization, although the error increased considerably compared to the smaller grid sizes: 9.04 and 19.58 for higher and first-order methods respectively. The improvement of performance was around ~50% in this case. While the errors were quite high for both schemes, the QUICKEST with limiter scheme did not deviate as much as the FOU scheme in the near-bed region, even for such a large grid discretization. The horizontal reach test case was also tested for some of the other higher-order methods, and their comparison of errors are shown in table 4.9 along with ranking of their performance.

4.4.3.2. Inclined reach

In the previous horizontal long channel test conditions, the flow was dominant in one direction only (along the horizontal), and variation of flow variables along the transverse direction was very minor. To observe the updated model in the transverse direction as well, a second test case was designed. The channel bed is inclined at an

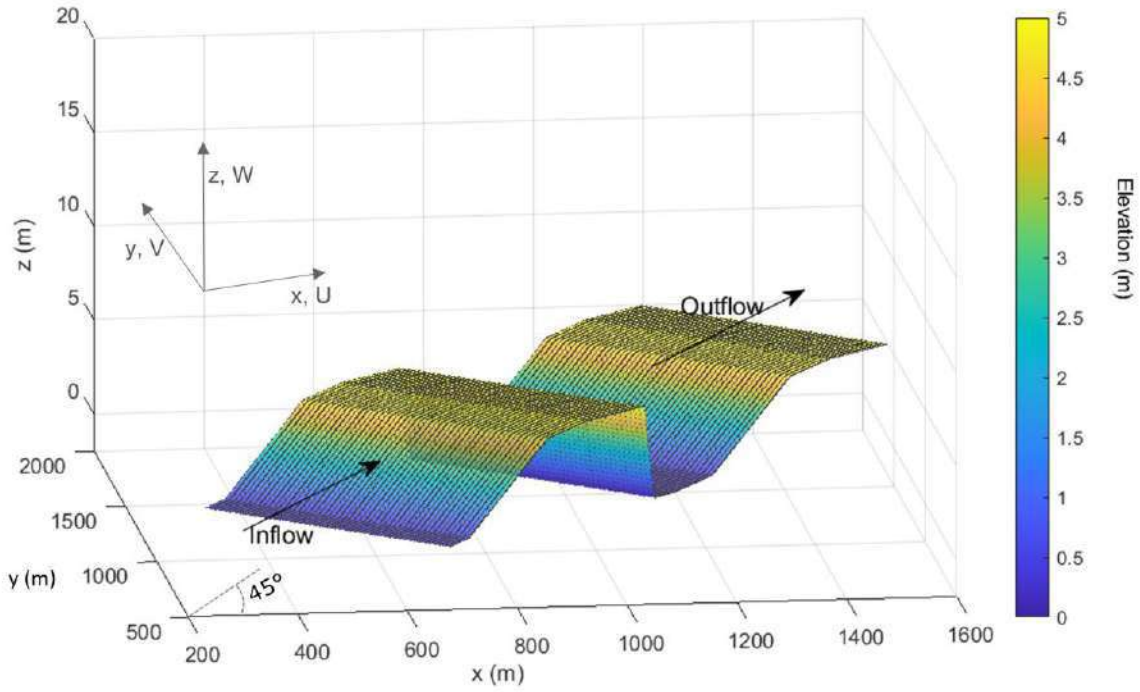

Figure 4.36 Bed elevation for 3D inclined (45°) reach

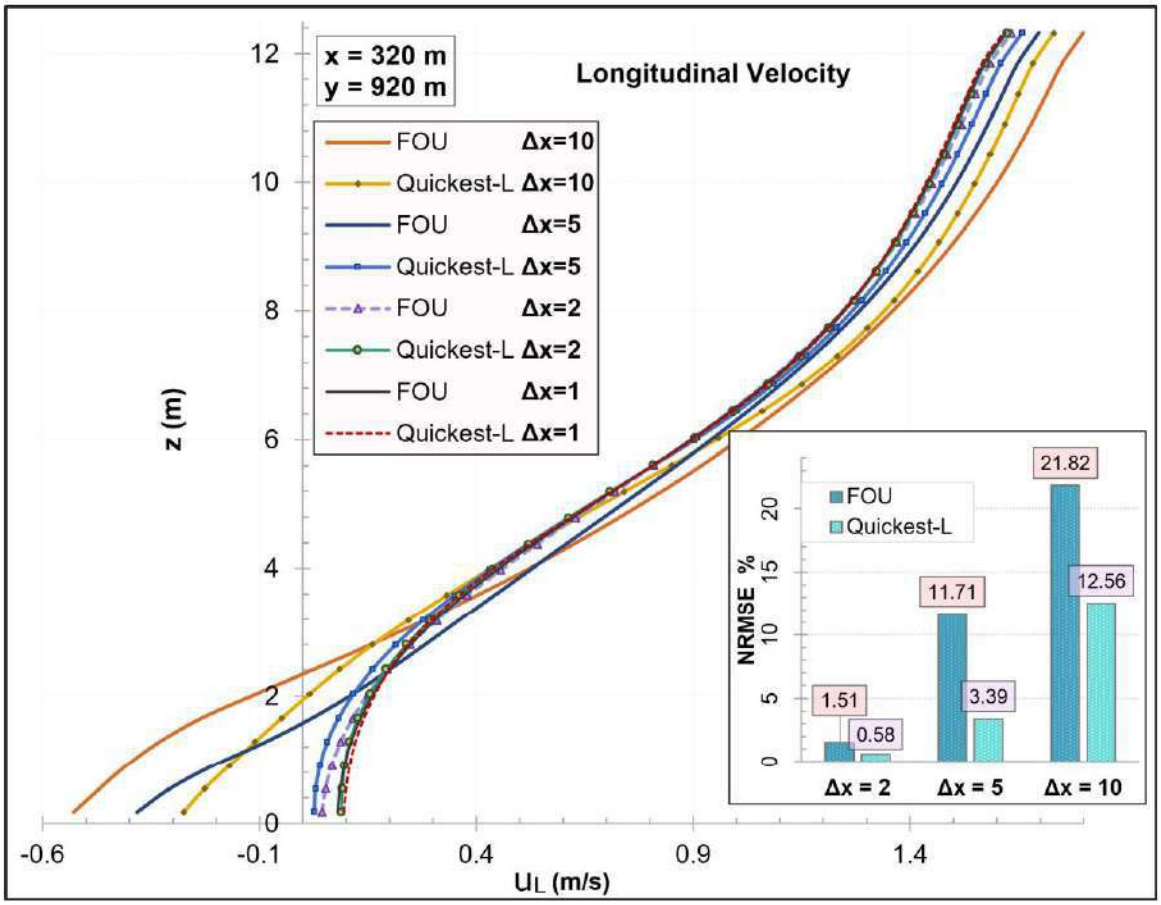

Figure 4.37 Longitudinal velocity distribution for 3D inclined reach

**Note*: here, $\Delta y = \Delta x$ in each corresponding condition

angle of 45° to the horizontal. The bed elevation is shown in figure 4.36. Apart from that the basis for this test case was the flow field in a trench experiment of Van Mierlo and de Ruiter's (1988), but in an enlarged scale. Although the width of the channel was still much smaller than the length, results from this test case showed variation in both directions in terms of flow variables.

The longitudinal velocity distribution for a section in the recirculation zone (just after the lee side slope), is shown in figure 4.37. The NRMSE values for both higher-order and first-order scheme for each of the different grid spacing is also shown in the figure. For 1 m discretization, the profiles are almost identical, and the average of these were

taken as the grid-independent result. Compared to this, the results for 2 m grid coarseness did not deviate that much; the error values were within 1.5 for both higher-order and first-order methods. For an increased spacing of 5 m, the error became larger, but still the QUICKEST-L scheme performed considerably better (~70%) than the FOU scheme; the NRMSE were 3.39 and 11.71 respectively. Graphically this was also evident from figure 4.37, as the higher-order velocity profile was much closer to the grid-independent one. However, as the coarseness was increased to Δx (= Δy) = 10 m, both schemes suffered a lot of diffusion. Although in the previous horizontal bed test case, the QUICKEST-L scheme approximated the grid-independent profile more closely in this case both methods deviated greatly in the near-bed region. The extent of deviation was greater for the first-order upwinding than the higher-order method.

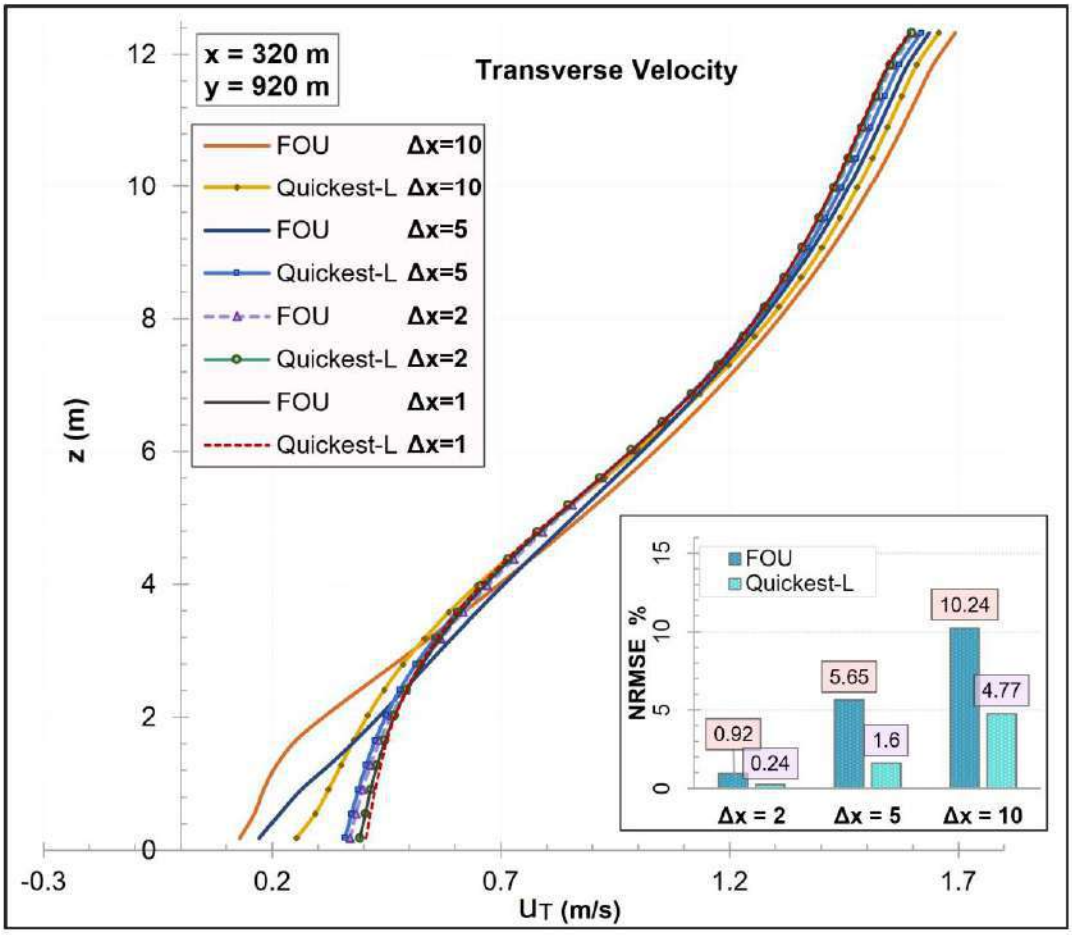

Figure 4.38 Transverse velocity distribution for 3D inclined reach

**Note*: here, $\Delta y = \Delta x$ in each corresponding condition

Table 4.10 Convergence and elapsed time of coupled 3D model for varying grid coarseness in inclined (45°) long reach test case

Discretization (m)	Average Convergence steps (n_{its})			Elapsed time (s)		
	FOU	QUICKEST-L	Average	FOU	QUICKEST-L	Average
Δx=1	2232	2196	2214	6558.75	6407.29	6483.02
Δx=2	1131	1070	1101	1124.63	1236.6	1180.615
Δx=5	449	462	456	137.02	122.58	129.8
Δx=10	399	400	400	58.51	80.18	69.345

**Note*: here, Δy = Δx in each corresponding condition

As the bed was inclined in the test case, substantial variation was observed in the transverse direction (across the channel). The results for the transverse direction followed similar patterns as the longitudinal direction, though the magnitude of the NRMSE values were smaller. Figure 4.38 shows the transverse velocity profile at a section for both FOU and QUICKEST-L methods, and also for the different grid coarseness used. The error values are showed in the figure as well. For all discretization values, the higher-order method performed better than the FOU scheme. A comparison of computational effort between the two schemes is also shown in table 4.10, in terms of convergence steps and elapsed time.

The results of this test case demonstrate the superior performance of the higher-order QUICKEST-L scheme compared to the first-order upwinding. The higher-order scheme at Δx= 5 m was able to achieve almost the same level of accuracy of as FOU method at Δx= 2 m. But the required convergence steps reduced by more than 50% as the grid coarseness was increased, and the elapsed time reduction was almost ten-fold. The computational efforts required did not decrease proportionally for greater spacing of 10 m; however, the higher-order method's error percentages were still significantly lower than the first-order method. The test case was also simulated with four other higher-order schemes, and a comparison of NRMSE produced and their ranking on the basis of error is shown in table 4.11. QUICKEST with limiter scheme was observed to produce least cumulative errors, which was followed closely by the Adaptive scheme,

Table 4.11 Ranking of the selected higher-order schemes for the 3D coupled model (inclined reach)

Scheme Name	NRMSE (%)				Rank based on least error produced
	Longitudinal direction		Transverse direction		
	Δx = 5 m	Δx = 10 m	Δx = 5 m	Δx = 10 m	
FOU	11.71	21.82	5.65	10.24	5
QUICKEST	3.895	11.774	2.238	5.033	3
QUICKEST-L	3.39	12.56	1.6	4.77	1
Adaptive	3.104	12.576	1.456	5.377	2
2ndOU	4.482	25.529	2.695	16.377	4

and the QUICKEST scheme (without limiter). Although the 2ndOU method proved to be quite accurate in the 5 m grid spacing, as the coarseness was increased to 10 m, its performance became worsened. However, all higher-order schemes ranked above the first-order method, which produced significant errors in both grid sizes. Overall, it can be inferred that the updated coupled 3D DA-RANS model improved both in terms of accuracy and computational efficiency, compared to the original original one, as higher-order advective discretization was implemented in the model.

4.4.4. 3D open channel flow modeling of Padma River at Naria

A real-life open channel flow scenario was next simulated using the upgraded 3D RANS model, and as study area, the erosion-prone part of Padma river near Naria Upazila of Shariatpur was selected. The computational grid was created, fitted to the study region's specific boundary. The outer four boundary lines were first extracted, and then the grid was generated by maintaining a 25 m spacing transversely in the narrow part across the channel, as shown in figure 4.39. The collected bathymetry data was then meshed with the grid, and the resulting bathymetry contour is given in figure 4.40. As can be observed from the bed elevations, the depth of the channel varies extremely irregularly in this region. In a vast portion, the elevation is close to zero (and greater than zero in some elevated places), but then again depths as high as 40 ~ 50 m are present. So vertical discretization was particularly challenging for this study area,

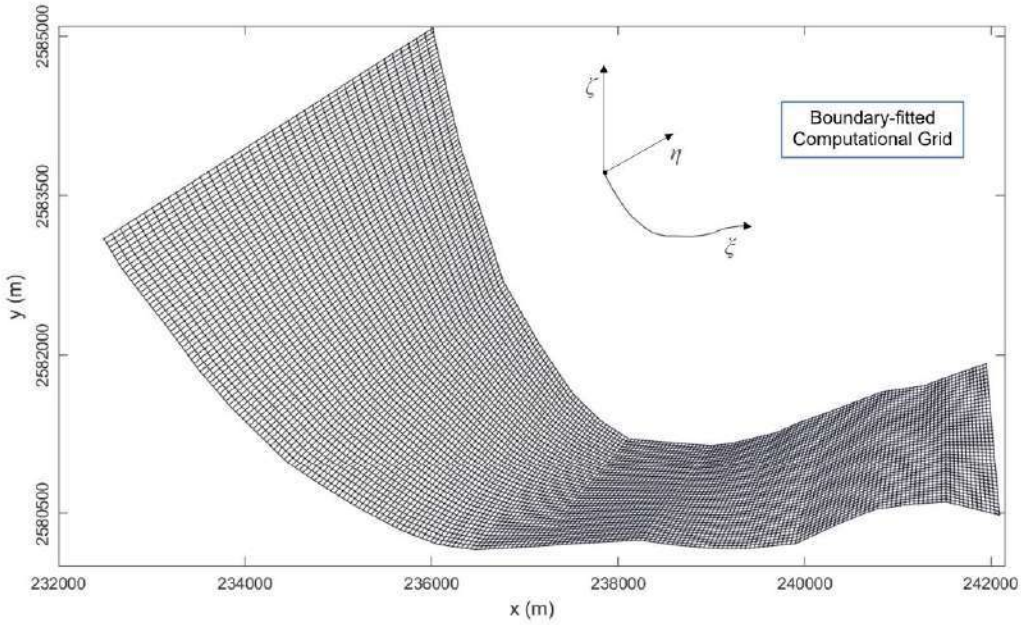

Figure 4.39 Boundary-fitted grid coordinate system for Naria

since both extremely high and low values need to be adequately and efficiently resolved numerically. After several trials, 30 nodes were found to be the most optimum, which would extend from the bed to the water surface level, at each grid point once the model is simulated.

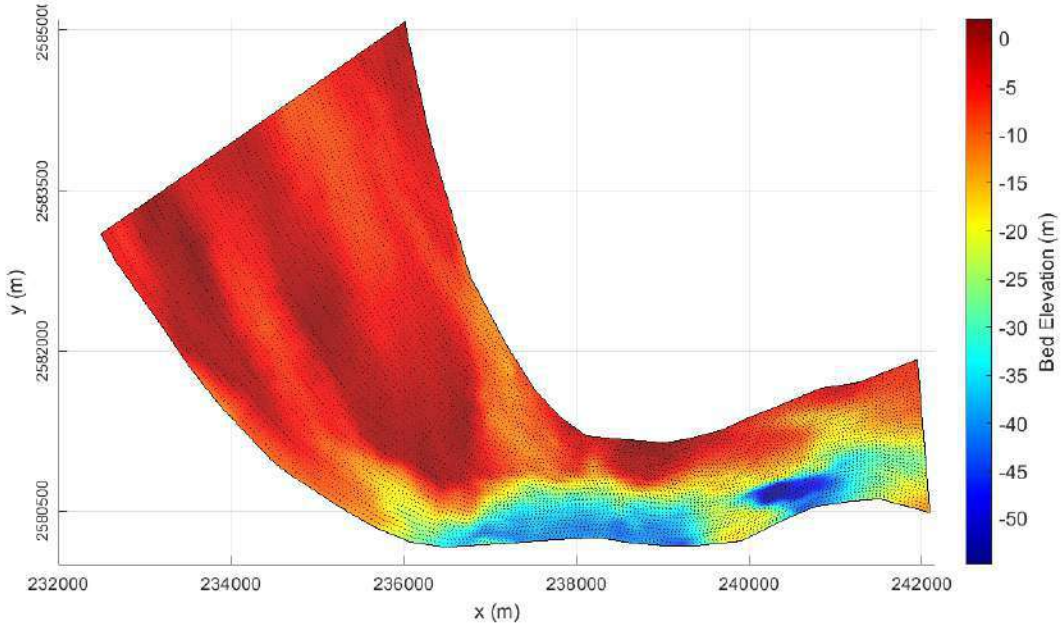

Figure 4.40 Bathymetry of the study area (elevation in m PWD)

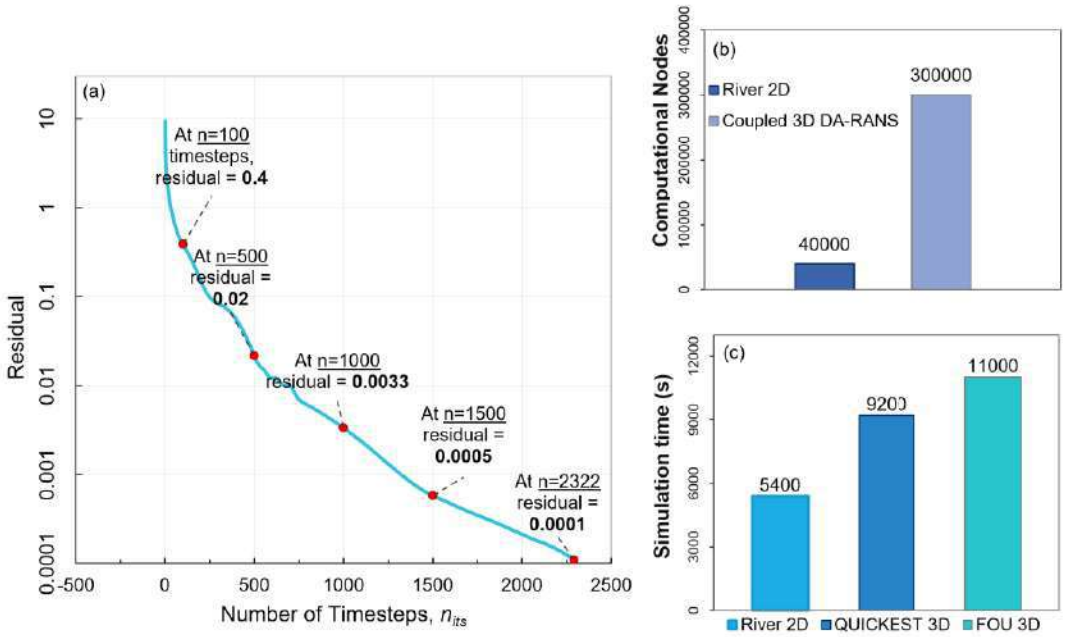

Figure 4.41 Gradual Convergence of the 3D model with QUICKEST-L scheme; Comparison of (b) computational nodes (c) simulation time

The model was simulated with a boundary condition of 1,00,000 cumec discharge in the upstream, and a downstream depth of 5.65 m. Although the measured peak flow was 1,27,000 cumec in the upstream, much of the peak flow goes over the dry bars (almost 15~20%), and so the upstream boundary was adjusted by reducing it by some factor. A roughness height, k_s= 0.06 was used throughout the grid (equivalent to ~0.025 manning's n). The depth-average velocity and water surface level obtained from the River2D (version 0.90), for the same boundary and bathymetry, were used as initial conditions in the 3D RANS model shown in figures B.13 of the Appendix). The final 3D mesh contained almost 300000 nodes, from the mesh 221×42×30. The model residual was set at 10^{-4} from the previous iteration, and a courant number of 0.9 was used. As a continuation of the previous sections, the QUICKEST-L scheme was the chosen higher-order scheme to use in the upgraded RANS model. Finally, after 2322 timesteps, and 9200 seconds, the model attained the desired level of accuracy and converged. The residual limit 10^{-4} was quite small, considering the complex simulation conditions of flow at Naria. Within only 500 iterations, the model was able to lower the residual to 0.02, as shown in figure 4.41. And after n = 800, it was 0.005- which can be considered quite adequate itself in open channel flow cases. The model was also simulated with the FOU method, and both methods' simulation time is compared side by side in figure 4.41. The QUICKEST-L method appeared to converge much faster

(by around 15%) than the first-order upwinding method. However, in terms of the flow variables, the difference was much more subtle, and the QUICKEST-L method introduced only minor improvements over FOU. At the same time, the two-dimensional simulation in River2D software under identical boundary and bathymetry conditions, consisted of ~40000 computational nodes, and its convergence took round 5400 seconds. It is noteworthy that although the coupled 3D DA-RANS model had almost 8 times the computational nodes of the 2D model, still the model simulation time increased only by 2 times. The high efficiency of the coupled 3D model is observed through this simulation. Again a more detailed representation of the flow field was obtained from the 3D model than the 2D model. Comparison of key flow variables are shown between the 2D and 3D results below.

Velocity

Significant difference between the 2D and 3D model was observed in terms of velocity. The 2D model could only provide depth-averaged velocity at each point, whereas from the 3D model vertical variation in velocity profile was successfully achieved. Figure 4.42 shows a comparison between velocity contours obtained from River2D and the coupled 3D model. In the 2D velocity contour, it can be seen that in most places, the average velocity was in the range of 2~3 m/s, and in a very localized area it reached as high as 4.95 m/s. Whereas in the 3D model the velocity near the bed was comparatively quite low (close to 0 m/s in most places, averaging around 1 m/s and only in limited regions exceeding 2 m/s), and near the surface it was close to 3 m/s on average. In the same localized zone where 2D model showed high DA velocity, the 3D model yielded a near-surface velocity of 5.75 m/s, and in the rest of the locations the average surface velocity was comparatively lower.

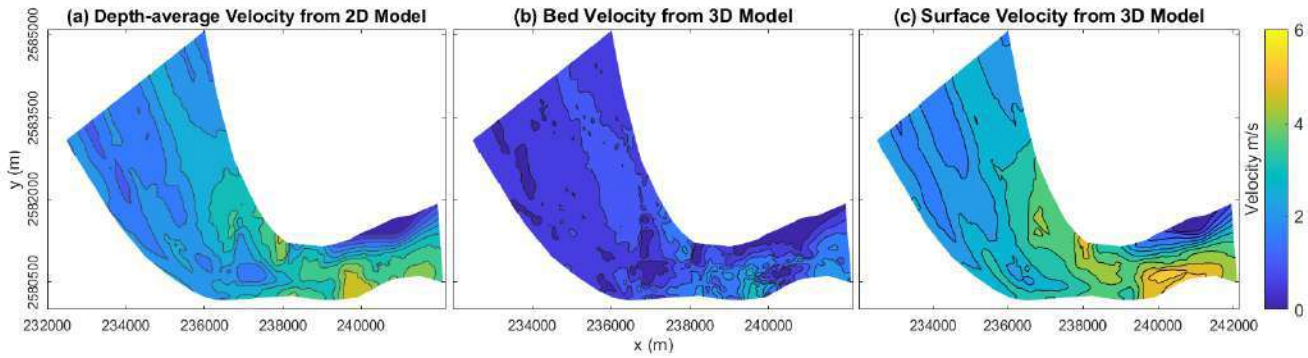

Figure 4.42 Comparison between (a) DA velocity from 2D model, (b) Nearbed velocity from 3D model (c) Surface velocity from 3D model

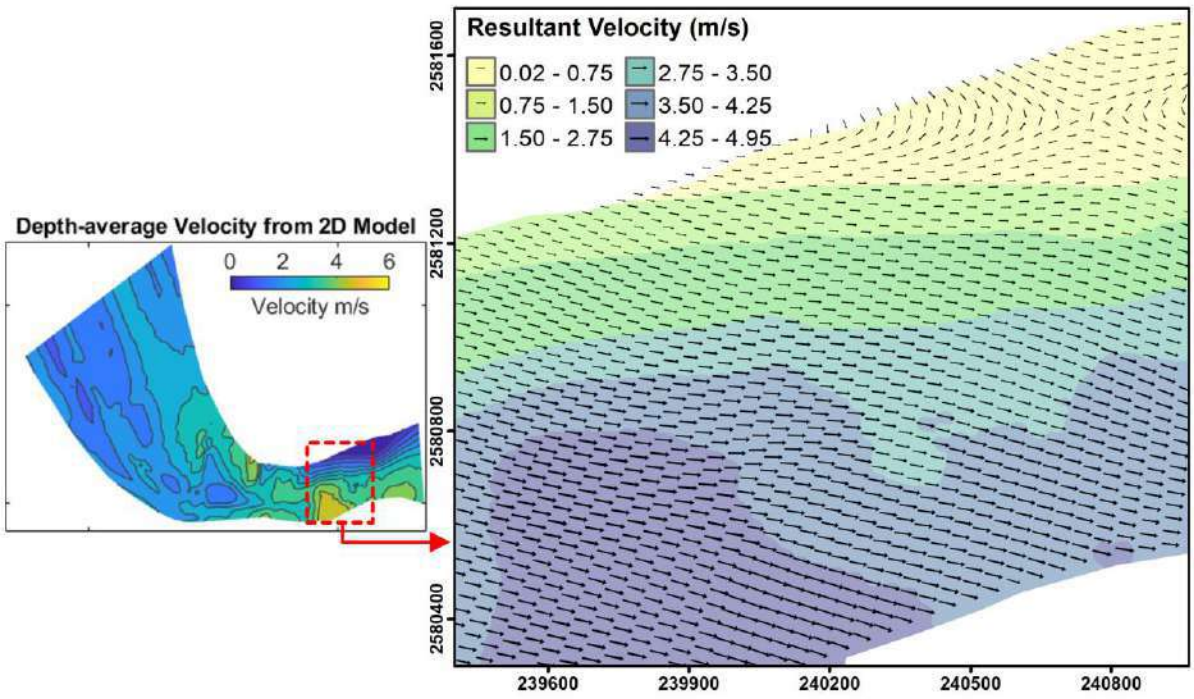

Figure 4.43 (a) DA velocity from 2D model, (b) Enlarged view of critical portion with velocity vectors

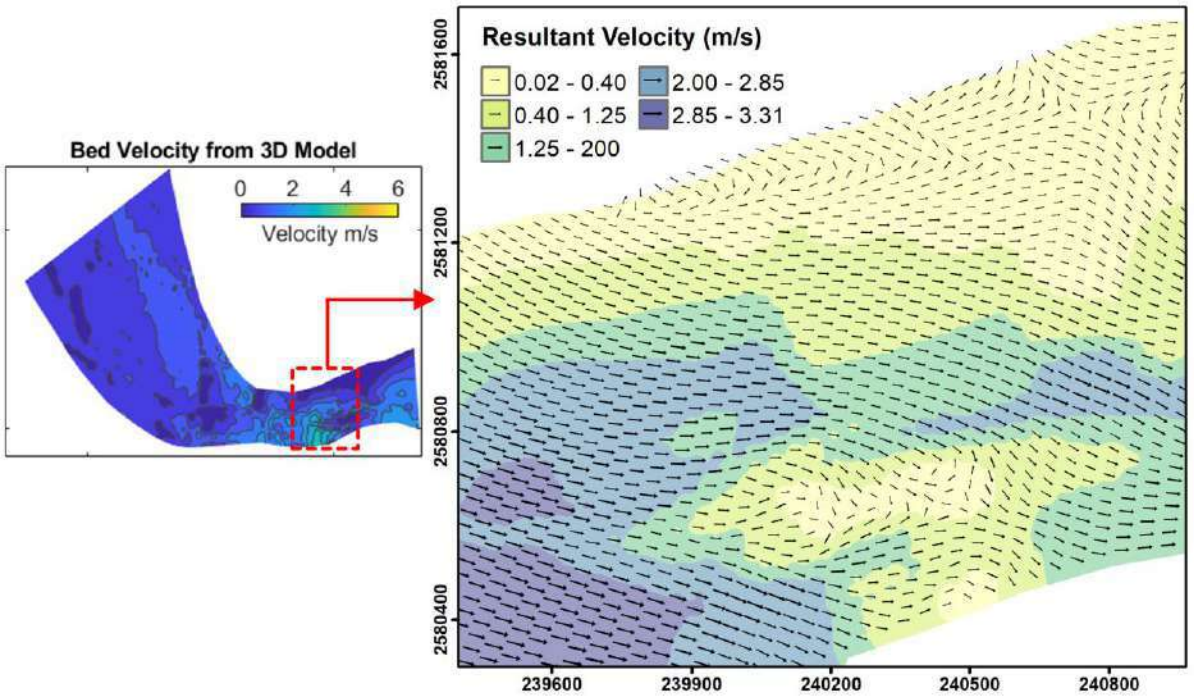

Figure 4.44 (a) Nearbed velocity from 3D model, (b) Enlarged view of critical portion with velocity vectors

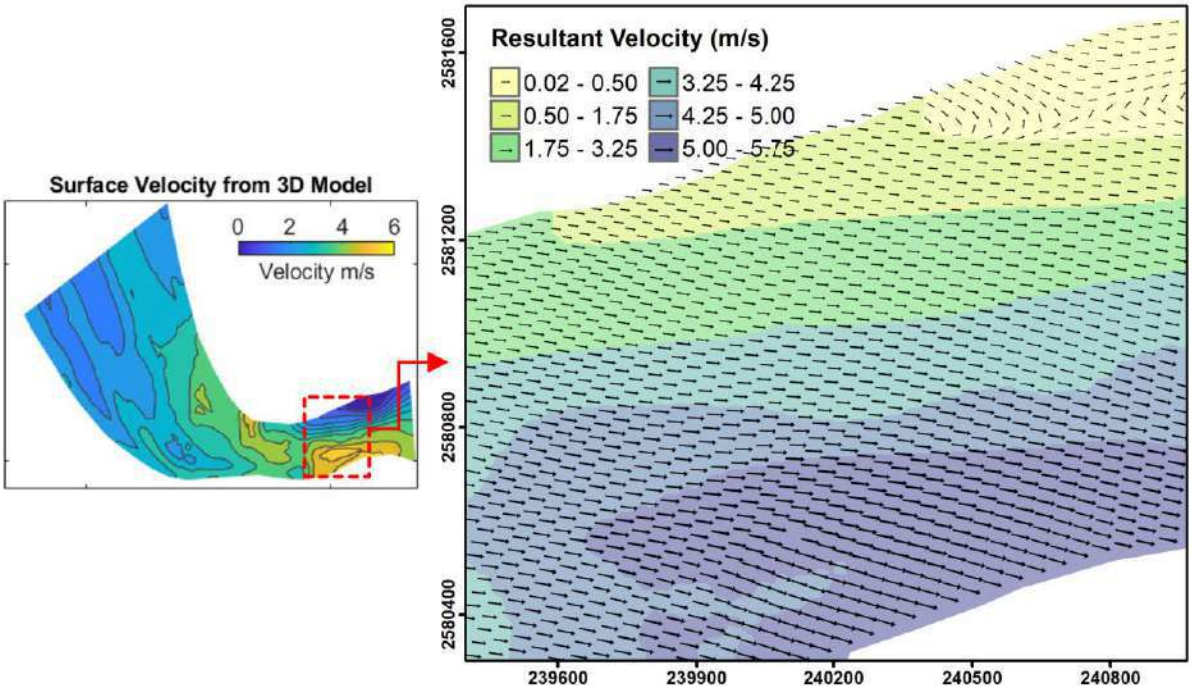

Figure 4.45 (a) Surface velocity from 3D model , (b) Enlarged view of critical portion with velocity vectors

In all cases, the high velocity values were observed in the portion of the channel where the width abruptly narrowed. Both models could correctly capture this increased velocity phenomenon, even though the magnitude differed substantially. Figure 4.43 to 4.45 show the velocity vector field of the same location. The depth-averaged velocity directions of 2D model closely resembled that of the surface velocity in 3D model. However, the 3D model was able to further capture the circualtions/vortices created near the bed, and this could not be obtained from the 2D model. Comparing figure 4.44 to the bed elevation of the study region, it can be inferred that in the deepest part of the channel is where the vortices are generated. Near the surface however such circulation of flow was not that much apparent.

From the 3D model, vertically varying velocity profiles were obtained at each grid points. On the other hand, for the 2D model, the velocity was uniform throught the depth of the water column. As an example, velocity distribution in the vertical direction at a point near the right bank of the channel is shown in figure 4.46. At the channel

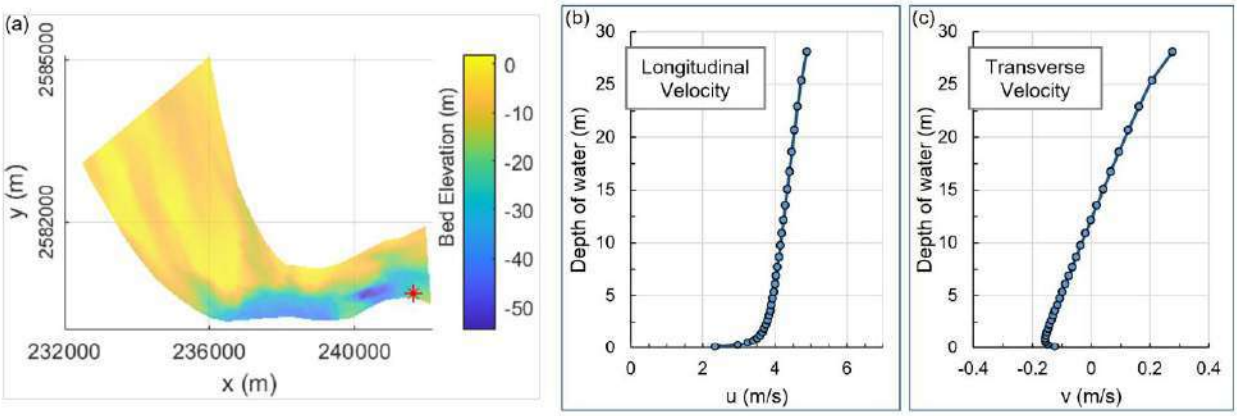

Figure 4.46 Vertical velocity distributions found from the 3D model (example shown at one point only)

bottom, the longitudinal velocity profile has a very high velocity gradient, and then increased gradually from 4 m/s to 4.8 m/s from the channel bottom to the top of the water surface. In the transverse direction, velocity also increased with depth, but there was some recirculation or negative velocity near the bed of the channel. The magnitude of the transverse velocity was much smaller, and within -0.2 to 0.25 m/s. Vertical velocity distribution at multiple points with varying water depth, along a cross-section of the reach is also shown in figure B.14 of the Appendix. The magnitude of the longitudinal velocity there varies from 0 to 5.25 m/s; this provides some insight as to why the bottom velocity at nearby points with higher elevation is considerably greater than zero. The transverse velocity's magnitude there is greater than the point shown in figure 4.46, but it experiences similar direction changes laterally.

Bed Shear Stress

The two models produced differing results in terms of shear stress as well. Contour plots of shear in the channel for 2D and 3D models are shown in figure 4.47. The average shear in the channel from the 2D model ranged between 20~30 N/m^2, with the maximum stress being 75.51 N/m^2. The shear stress from the 3D model varied in a much wider range, experiencing very small to very high stress values. The maximum bed stress found in the 3D case (with advection QUICKEST-L scheme) was 129.84 N/m^2, almost double that of the 2D model. Again from the 3D model with first-order

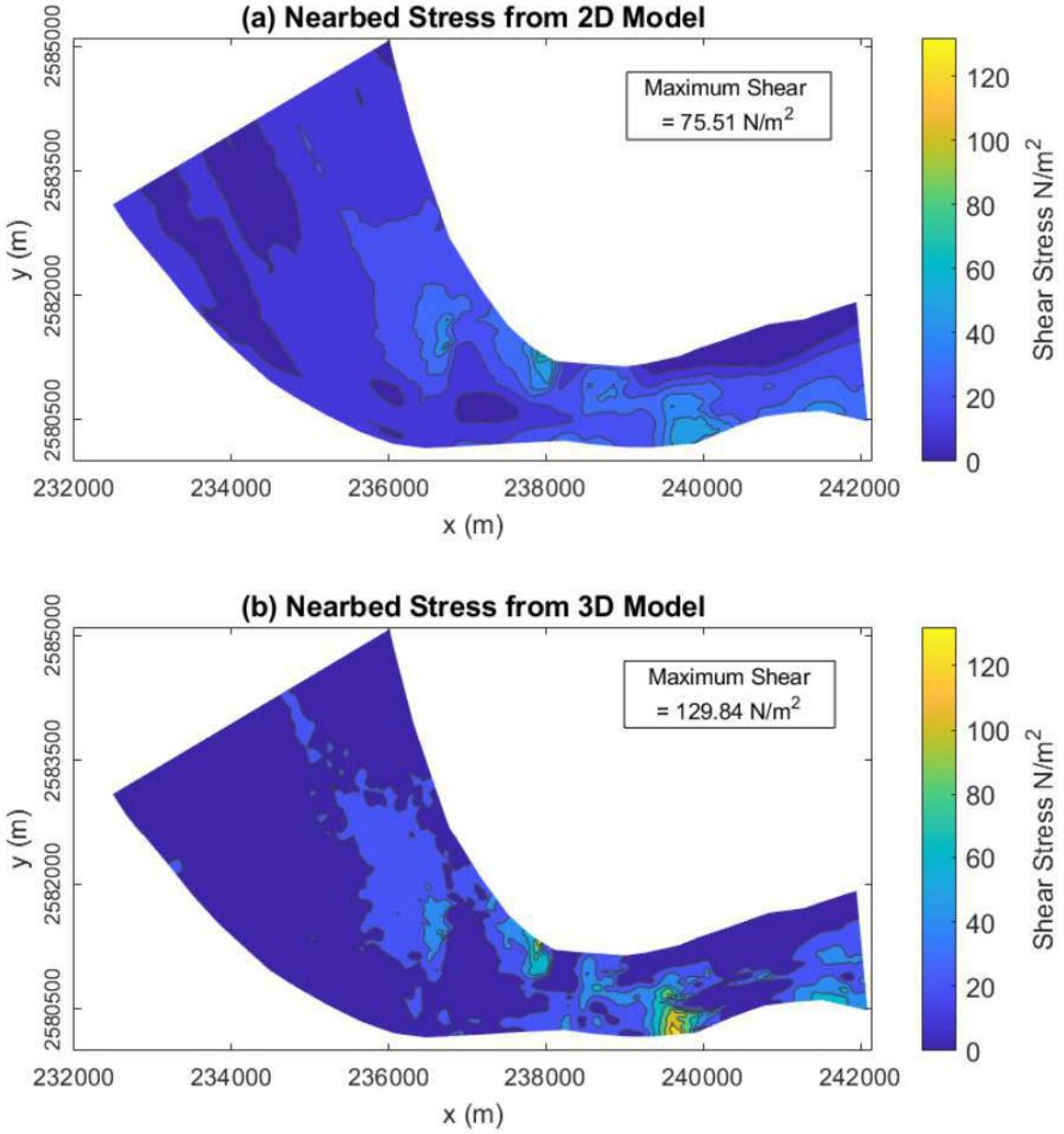

Figure 4.47 Bed shear stress from (a) 2D model, (b) 3D model

upwinding, the maximum shear was 129.66 N/m^2, slightly underpredicted than the QUICKEST-L method. So, the higher-order upwinding was able to introduce some minor improvements to the original model.

A visual comparison between the two models' result clearly shows that the 2D model underpredicted the stress experienced near the erosion-prone riverbanks. The 3D QUICKEST-L model was able to provide more detailed levels of information about the flow parameters.

Table 4.12 Comparison between the different higher-order schemes used in 3D modeling of Padma River at Naria

Scheme	Convergence steps (n_{its})	Simulation time (s)	**Simulated maximum bed shear stress (N/m^2)**
First-Order Upwind	2223	11005.96	129.6615
Second-Order Upwind	2255	10498.91	129.8366
Adaptive	2500	8734.265	131.4181
QUICKEST	2347	8167.902	131.5452
QUICKEST-Limiter	2322	9288.298	129.8465

The coupled 3D model was also simulated for some of the other selected higher-order schemes, and the comparison between the different method are shown in table 4.12, in terms of computational efforts, and also maximum bed shear stress. Local hydrodynamics and morphological changes heavily depend on the shear stress

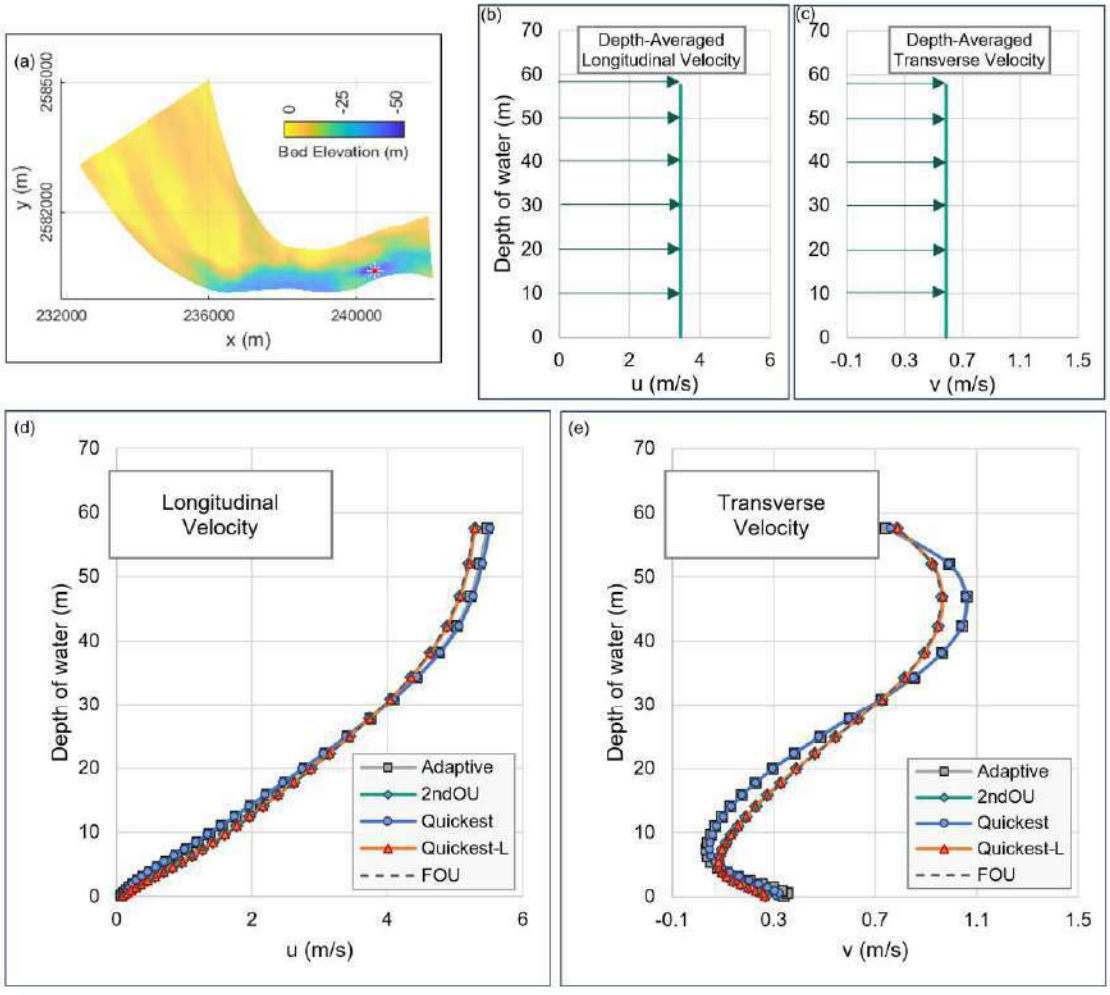

Figure 4.48 Comparison between the different higher-order schemes in simulating vertical velocity distribution profile

generated at the channel bottom. Bed shear is of particular importance in the context of this study, since the banks of this reach are experiencing significant erosion. From the results, it was observed that when the limiter option is turned off in the third-order QUICKEST scheme, it is able to simulate a higher value of shear stress. The same was observed for the Adaptive method, which switches off the limiter in regions of maxima values. However, the second-order upwind method did not result in a substantial improvement over the first-order method. Changes in vertical velocity distribution were also observed for the different schemes. Vertical velocity profiles in both the longitudinal and transverse directions for one of the deepest nodes (~60 m depth) are shown in figure 4.48. The QUICKEST scheme (without limiter) and the Adaptive scheme produced the most varying profiles, compared to the uniform velocity profiles obtained from the depth-averaged 2D model. The first- and second-order upwinding methods and the limited QUICKEST schemes were relatively closer to the DA uniform velocity profiles. Again, the Adaptive and Quickest schemes were able to capture zones of high bed shear, that were not present in the other methods' results. Variation in bed shear stress found from the different schemes are shown in Appendix figures B.15 and B.16.

CHAPTER 5

CONCLUSIONS AND RECOMMENDATIONS

The present study attempted to improve an existing three-dimensional computational fluid dynamic (CFD) model based on the Reynolds averaged Navier-Stokes (RANS) equations, by implementing higher-order discretization of the advection terms. Among the great numbers of numerical schemes that have been developed in the last few decades for better approximation of the convective terms in CFD, thirty such well-recognized higher-order upwinding methods were first tested in a more simplified setting of one and two-dimensional advection only. The schemes' performance was assessed in terms of accuracy and diffusivity, and the best performing schemes were then finally tested for accuracy and computational efficiency in the coupled depth-averaged (DA) and Reynolds averaged Navier-Stokes (RANS) 2D and 3D models of Zobeyer (2012) developed for real-life open channel flow cases.

5.1. Conclusions

From the results of this study the following conclusions can be made

- Initially when the thirty higher-order schemes were used to simulate 1D pure advection, each of the schemes exhibited different levels of stability and accuracy. Adaptive scheme, fifth-order upwinding, SUPERBEE, QUICKEST, MUSCL were some of the methods that yielded considerably better results (85-97% peak accuracy). Accuracy of the results greatly increased with higher courant numbers and NRMSE values for the triangular distribution with cr = 0.9, was calculated to be in the range of 1.93 to 3.44 for the five schemes, which suggests reasonably good accuracy, and the NV indices were within ±0.5 for these five schemes, indicating that these five methods were neither too diffusive nor compressive. However, for the same scenario, NRMSE and NV index values for the FOU method were 10.09 and -10.37, respectively- which was much less accurate and more diffusive compared to the chosen higher-order schemes.

- The higher-order schemes performed significantly better in the simulation of 2D advection as well in terms of preserving the peak accuracy of the tracer distribution. All of the higher-order schemes attained almost 99-100% of the maxima value, in contrast to the first-order upwinding preserving only 37% peak accuracy. However, in terms of stability, the first-order upwinding method seems to yield the most smooth solution compared to the higher-order methods. In contrast, QUICKEST, Adaptive, and Superbee solutions all have some presence of oscillations, even though overall error values were lower for the higher-order methods.

- The higher-order advection schemes were then incorporated into the 2D DA-RANS model and the model was verified against some experimental data. Test cases of long reaches with different numerical grid coarseness in the longitudinal flow direction were simulated, where the grid-independent result was taken as benchmark for comparison. The higher-order schemes resulted in 20-30% better results than the FOU scheme on average in the second iteration of the RANS model. The second-order upwinding method performed especially well in the 2D coupled model and its NRMSE value was only about 75% less than that of the first-order method in the large scale test case. This was followed by the Adaptive, 5^{th} order upwind with limiter and QUICKEST with limiter schemes, which resulted in an improvement of around 30% over the original model with first-order upwinding. Particularly in the lower parts of the velocity profiles and in the bed stress profiles, the higher-order schemes appeared to be closer to the grid-independent results, and first-order upwinding profile was the one farthest away. From these outcomes, it can be inferred that higher-order methods are better equipped to simulate near-bed properties of the flow.

- The higher-order schemes were then extended to the more complex 3D flow once they were found to produce sufficiently stable and accurate results in the 2D flow simulations. After verification of the model against experimental results, sufficiently large test cases were simulated with varying space discretization Δx and Δy. In both the longitudinal and transverse directions, the higher-order, QUICKEST with limiter scheme approximated the grid-independent solution more closely than the FOU method by a significant margin. The Adaptive scheme, QUICKEST scheme (without limiter) and the 2ndOU method also surpassed the first-order method in

terms of accuracy and were ranked higher based on the least amount of error produced.

- The upgraded 3D model was also used to simulate a real case open channel flow scenario of Padma River near Naria Upazila. The 3D model was able to provide a greater level of information regarding the vertical variation of velocity compared to results obtained from a River2D numerical model. On the other hand, the difference between first-order and higher-order RANS model, in terms of the flow variables was much more subtle, and the chosen higher-order method introduced only minor improvements over FOU. However, the required time for convergence was much lower for the higher-order scheme (~9200 seconds 300000 nodes) than the first-order upwinding (11000 seconds). Again, in terms of bed stress, the 2D model significantly underpredicted the near-bed shear (maximum value of 75 N/m^2), whereas from the 3D model the maximum shear was found to be 129 N/m^2 in the erosion-prone right bank area of the river. In total, performance of four of the higher-order schemes were investigated in the updated 3D model in this study: the second-order upwind method, Adaptive method, and the QUICKEST scheme (both with and without limiters). All of these higher-order schemes performed comparatively better than the first-order method in terms of simulation time and resulted in greater variation from the uniform depth-averaged 2D model results.

5.2. Recommendations

Recommendations for further extension of the present work are discussed in this section. Several issues that were not addressed in this research but can be done in the future:

- Although the model showed overall good performance in predicting velocity profiles, there remains scope for improvement in reproducing the recirculation zone. In the recirculation zone, the flow is more complex, and a better turbulence model can be helpful in predicting the length of the recirculation accurately. Here only zero equation turbulence models were used in the RANS model. Future studies could further upgrade the model by using the one or two equation turbulence models.

- The coupled model is developed for steady flow computation. The model can be adapted for unsteady flow calculations where the coupling between the DA and the RANS model will take place at each time step.
- Sediment transport modeling capabilities could be added to the existing model for solving total-load sediment transport with an advection-diffusion solver and algorithms that support of morphological processes.
- In future extensions of the model, other techniques, particularly the finite element technique, can be used as it provides flexibility to model the complex natural geometry. As such the 3D model can be developed using the framework of the River2D model.

REFERENCES

Alfonsi, G. (2009). Reynolds-averaged Navier–Stokes equations for turbulence modeling. Applied Mechanics Reviews, 62(4).

Anees, M. T., Abdullah, K., Nawawi, M. N. M., Ab Rahman, N. N. N., Piah, A. R. M., Zakaria, N.A., Syakir, M.I., and Omar, A.M. (2016). Numerical modeling techniques for flood analysis. Journal of African earth sciences, 124, 478-486.

Arora, M., and Roe, P.L. (1997). A well-behaved TVD limiter for high-resolution calculations of unsteady flow. Journal of Computational Physics, 132(1), 3-11.

Biron, P. M., Haltigin, T. W., Hardy, R. J., and Lapointe, M. F. (2007). Assessing different methods of generating a three-dimensional numerical model mesh for a complex stream bed topography. International Journal of Computational Fluid Dynamics, 21(1), 37-47.

Botte, G. G., Ritter, J. A., and White, R. E. (2000). Comparison of finite difference and control volume methods for solving differential equations. Computers & Chemical Engineering, 24(12), 2633-2654.

Buelow, P.E.O., Venkateswaran, S., and Merkle, C.L. (1994). Effect of grid aspect ratio on convergence. AIAA J., 32 (12), 2401-2409.

Čada, M., and Torrilhon, M. (2009). Compact third-order limiter functions for finite volume methods. Journal of Computational Physics, 228(11), 4118-4145.

Caballeria, M., Coco, G., Falqués, A., and Huntley, D. A. (2002). Self-organization mechanisms for the formation of nearshore crescentic and transverse sand bars. Journal of Fluid Mechanics, 465, 379-410.

Cardenas, M. B., and Zlotnik, V. A. (2003). Three-dimensional model of modern channel bend deposits. Water Resources Research, 39(6).

Chanson, H. (2004). Hydraulics of open channel flow. Elsevier.

Chao, X., Jia, Y., Shields Jr, F. D., Wang, S. S., and Cooper, C. M. (2007). Numerical modeling of water quality and sediment related processes. Ecological modelling, 201(3), 385-397.

Chaudhry, M. H. (2007). Open-channel flow. Springer Science & Business Media.

Dargahi, B. (2004). Three-dimensional flow modeling and sediment transport in the river Klaralven. Earth Surf. Process. Landforms, 29, 821-852.

Daubert, A., and Graffe, O. (1967). Some aspects of nearly horizontal flows in two dimensions in plan and non-permanent application to estuaries. La Houille Blanche, 8, 847-860.

De Saint-Venant, B. (1871). Theorie du movement non permanent des eausx, avec application aux crues de rivieras et a l'introduction des merces dans leur lit. Comptes Rendus de l'Academic des Science, 73, 147-154, 237-240.

Doering, C. R., and Gibbon, J. D. (1995). Applied analysis of the Navier-Stokes equations, 12. Cambridge university press.

Fischer-Antze, T., Stoesser, T., Bates, P., and Olsen, N. R. B. (2001). 3D numerical modelling of open-channel flow with submerged vegetation. Journal of Hydraulic Research, 39(3), 303-310.

French, R. H. (1985). Open-channel hydraulics. New York: McGraw-Hill.

Garcia-Navarro, P., Alcrudo, F., and Saviron, J.M. (1992). 1-D open channel flow simulation using TVD-McCormack scheme. J. Hydraul. Eng., 118(10), 1359-1372.

Godunov, S., and Bohachevsky, I. (1959). Finite difference method for numerical computation of discontinuous solutions of the equations of fluid dynamics. Matematičeskij sbornik, 47(3), 271-306.

Hardy, R. J., Lane, S. N., Lawless, M. R., Best, J. L., Elliott, L., and Ingham, D. B. (2005). Development and testing of a numerical code for treatment of complex river channel topography in three-dimensional CFD models with structured grids. Journal of Hydraulic Research, 43(5), 468-480.

Harten, A. (1983). High resolution schemes for hyperbolic conservation laws. Journal of computational physics, 135(2), 260-278.

Hayase, T., Humphrey, J.A.C., and Greif, R. (1992). A consistently formulated QUICK scheme for fast and stable convergence using finite-volume iterative calculation procedures. Journal of Computational Physics, 98(1), 108-118.

Heller, V. (2011). Scale effects in physical hydraulic engineering models. Journal of Hydraulic Research, 49(3), 293-306.

Hicks, F.E. (1990). Finite element modeling of open channel flow. Ph.D. thesis. Department of Civil Engineering, University of Alberta.

Hirt, C.W., and Nichols, A. (1981). Volume of fluid (VOF) methods for the dynamics of free boundaries. J. Comput. Phys., 39, 201-225.

Hindmarsh, A. C., Gresho, P. M., and Griffiths, D. F. (1984). The stability of explicit Euler time-integration for certain finite difference approximations of the multi-dimensional advection–diffusion equation. International journal for numerical methods in fluids, 4(9), 853-897.

Horritt, M. S., and Bates, P. D. (2002). Evaluation of 1D and 2D numerical models for predicting river flood inundation. Journal of hydrology, 268(1-4), 87-99.

Ingham, D. B., and Ma, L. (2005). Fundamental equations for CFD river flow simulations. Computational fluid dynamics. Applications in environmental hydraulics. Wiley, Chichester, England, 534.

Kemm, F. (2011). A comparative study of TVD-limiters—well-known limiters and an introduction of new ones. International Journal for Numerical Methods in Fluids, 67(4), 404-440.

Kuan, K.B., and Lin, C.A. (2000). Adaptive QUICK-based scheme to approximate convective transport. AIAA journal, 38(12), 2233-2237.

Lai, C. (1986). Numerical modeling of unsteady open-channel flow. Advances in hydroscience, Elsevier, 14, 161-333.

Lai, W., and Khan, A. A. (2018). Numerical solution of the Saint-Venant equations by an efficient hybrid finite-volume/finite-difference method. Journal of Hydrodynamics, 30(2), 189-202.

Lane, S. N., Hardy, R. J., Ferguson, R. I., and Parsons, D. R. (2005). A framework for model verification and validation of CFD schemes in natural open channel flows. Computational fluid dynamics: Applications in environmental hydraulics, 169-192.

Lax, P. D., and Wendroff, B. (1960). Systems of Conservation Laws. Comm. Pure Appl. Math., 13.

Lee, J. W., Teubner, M. D., Nixon, J. B., and Gill, P. M. (2006). A 3-D non-hydrostatic pressure model for small amplitude free surface flows. International Journal for Numerical Methods in Fluids, 50(6), 649-672.

Leonard, B. P. (1979). A stable and accurate convective modelling procedure based on quadratic upstream interpolation. Computer methods in applied mechanics and engineering, 19(1), 59-98.

Leonard, B.P. (1988). Simple high-accuracy resolution program for convective modelling of discontinuities. International Journal for Numerical Methods in Fluids, 8(10), 1291-1318.

Leonard, B. P. (1991). The ULTIMATE conservative difference scheme applied to unsteady one-dimensional advection. Computer methods in applied mechanics and engineering, 88(1), 17-74.

Leonard, B.P., and Niknafs, H. S. (1991). Sharp monotonic resolution of discontinuities without clipping of narrow extrema. Computers and Fluids, 19(1), 141-154.

Leonard, B.P. (1995). Order of accuracy of QUICK and related convection-diffusion schemes. Applied Mathematical Modelling, 19(11), 640-653.

Leonard, B.P., Lock, A.P., and Macvean, M.K., (1996). Conservative explicit unrestricted-timestep multidimensional constancy-preserving advection schemes. Mon. Weather Rev. 124 (11), 2588.

Lien, F.S., and Leschziner, M.A. (1994). Upstream monotonic interpolation for scalar transport with application to complex turbulent flows. International Journal for Numerical Methods in Fluids, 19(6), 527-548.

Lien, H. C., Hsieh, T. Y., Yang, J. C., and Yeh, K. C. (1999). Bend-flow simulation using 2D depth-averaged model. Journal of Hydraulic Engineering, 125(10), 1097-1108.

Lin, C.H., and Lin, C.A. (1997). Simple high-order bounded convection scheme to model discontinuities. AIAA journal, 35(3), 563-565.

Lin, L., and Liu, Z. (2019). TVDal: Total variation diminishing scheme with alternating limiters to balance numerical compression and diffusion. Ocean Modelling, 134, 42-50.

Louaked, M., and Hanich, L. (1998). TVD schemes for shallow water equations. J. Hydraul. Res., 36(3), 363-378.

MacCormack, R.W. (1969). The effect of viscosity in hypervelocity impact catering. AIAA Paper, 66-354.

Nagata, N., Hosoda, T., Nakato, T., and Muramoto, Y. (2005). Three-dimensional numerical model for flow and bed deformation around river hydraulic structures. Journal of Hydraulic Engineering, 131(12), 1074-1087.

Namin, M. M., Lin, B., and Falconer, R. A. (2001). An implicit numerical algorithm for solving non-hydrostatic free-surface flow problems. International Journal for Numerical Methods in Fluids, 35(3), 341-356.

Neill, S. P., Hashemi, M. R., and Elliott, A. J. (2007). An enhanced depth-averaged tidal model for morphological studies in the presence of rotary currents. Continental shelf research, 27(1), 82-102.

Nguyen, T. H. T., Ahn, J., and Park, S. W. (2018). Numerical and physical investigation of the performance of turbulence modeling schemes around a scour hole downstream of a fixed bed protection. Water, 10(2), 103.

Nicholas, A. P. (2001). Computational fluid dynamics modelling of boundary roughness in gravel-bed rivers: an investigation of the effects of random variability in bed elevation. Earth Surface Processes and Landforms, 26(4), 345-362.

Noor, F., Chowdhury, S., Islam, M. A., Kafi, M. A. H., and Jahan, S (2021). Effectiveness of river training works through mathematical modelling: a case study of bank erosion at Naria upazila. Proceedings of The Third International Conference on Planning, Architecture & Civil Engineering.

Pinder, G. F., and Sauer, S. P. (1971). Numerical simulation of flood wave modification due to bank storage effects. Water Resources Research, 7(1), 63-70.

Qian, Q., Stefan, H.G., and Voller, V.R. (2007). A physically based flux limiter for QUICK calculations of advective scalar transport. International Journal for Numerical Methods in Fluids, 55(9), 899-915.

Qin, X., Motley, M., LeVeque, R., Gonzalez, F., and Mueller, K. (2018). A comparison of a two-dimensional depth-averaged flow model and a three-dimensional RANS model for predicting tsunami inundation and fluid forces. Natural Hazards and Earth System Sciences, 18(9), 2489-2506.

Roe, P.L. (1985). Some contributions to the modelling of discontinuous flows. Large-scale Computations in Fluid Mechanics, 163-193.

Raju, K. R., Asawa, G. L., and Mishra, H. K. (2000). Flow-establishment length in rectangular channels and ducts. Journal of Hydraulic Engineering, 126(7), 533-539.

RRI (2019). Physical model study for Padma River dredging management in Jajira and Naria upazilla under Shariatpur district, Annual Report, River Research Institute.

Salih, A., and Ghosh Moulic, S. (2009). Some numerical studies of interface advection properties of level set method. Sadhana, 34(2), 271-298.

Shahriari, S., Schneider, J., and Zenz, G. (2020). Selected applications of an open-source three-dimensional computational fluid dynamic code in hydraulic engineering. Österreichische Wasser-und Abfallwirtschaft, 72(7), 291-307.

Shen, Y., and Diplas, P. (2008). Application of two-and three-dimensional computational fluid dynamics models to complex ecological stream flows. Journal of Hydrology, 348(1-2), 195-214.

Sinha, S. K., Sotiropoulos, F., and Odgaard, J. (1998). Three-dimensional numerical model for flow through natural rivers. J. Hydraul. Eng., 124 (1), 13-24.

Sivakumaran, N. S., Tingsanchali, T., and Hosking, R. J. (1983). Steady shallow flow over curved beds. Journal of fluid mechanics, 128, 469-487.

Stansby, P. K., and Zhou, J. G. (1998). Shallow-water flow solver with non-hydrostatic pressure: 2D vertical plane problems. International Journal for Numerical Methods in Fluids, 28(3), 541-563.

Steffler, P. M. (1984). Turbulent flow in a curved rectangular channel. PhD thesis, University of Alberta, Edmonton, Canada.

Steffler, P.M., and Jin, Y. (1993). Depth-averaged and moment equations for moderately shallow free surface flow. J. Hydraul. Res., 31(1), 5-17.

Steffler, P., and Blackburn, J. (2002). River2D: Two-dimensional depth-averaged model of river hydrodynamics and fish habitat- Introduction to depth averaged modeling and user's manual. University of Alberta, Canada.

Szymkiewicz, R. (1993). Solution of the inverse problem for the Saint Venant equations. Journal of Hydrology, 147(1-4), 105-120.

Tamamidis, P., and Assanis, D.N. (1993). Evaluation of various high-order-accuracy schemes with and without flux limiters. International Journal for Numerical Methods in Fluids, 16(10), 931-948.

Temam, R. (2001). Navier-Stokes equations: theory and numerical analysis, 343. American Mathematical Soc.

Van Leer, B. (1979). Towards the ultimate conservative difference scheme. V. A second-order sequel to Godunov's method. Journal of computational Physics, 32(1), 101-136.

Van Mierlo, M. C. L. M., and De Ruiter, J. C. C. (1988). Rivers: Turbulence Measurements Above Artificial Dunes: Report on Measurements. Delft Hydraulics.

Van Rijn, L. C. (1990). Principles of fluid flow and surface waves in rivers, estuaries, seas and oceans, 12. The Netherlands: Aqua Publications.

Versteeg, H. K., and Malalasekera, W. (2007). An introduction to computational fluid dynamics: the finite volume method. Pearson education.

Wang, J.S., Ni, H.G., and He, Y.S. (2000). Finite-difference TVD scheme for computation of dam-break problems. J. Hydraul. Eng., 126(4), 253-262.

Weiyan, T. (1992). Shallow water hydrodynamics. Elsevier Oceanography Series 55, Elsevier, Amsterdam.

Wu, H., and Zhu, J. (2010). Advection scheme with 3rd high-order spatial interpolation at the middle temporal level and its application to saltwater intrusion in the Changjiang Estuary. Ocean Modelling, 33(1-2), 33-51.

Yang, H.Q., and Przekwas, A.J. (1992). A comparative study of advanced shock-capturing shcemes applied to Burgers' equation. J. Comput.Phys. 102 (1), 139–159.

Zhang, D., Jiang, C., Liang, D., and Cheng, L. (2015). A review on TVD schemes and a refined flux-limiter for steady-state calculations. Journal of Computational Physics, 302, 114-154.

Zobeyer, A. H. (2012). Depth averaged and RANS modeling of open channel flow. PhD thesis, University of Alberta, Edmonton, Canada.

APPENDIX A

Table A.1 Error comparison for 2D long reach test case at x =220 m

x = 220 m section	NRMSE %					
	N = 1			N = 2		
	Δx = 2 m	**Δx = 5 m**	**Δx = 10 m**	**Δx = 2 m**	**Δx = 5 m**	**Δx = 10 m**
FOU	0.902	3.11	11.889	0.645	2.362	8.82
QUICKEST	0.993	2.639	13.972	0.841	2.364	10.116
Superbee	1.055	2.892	14.374	0.816	1.931	10.017
MUSCL	0.947	2.887	13.784	0.698	1.832	9.672
Adaptive	0.95	2.581	13.355	0.684	1.714	9.142
5thOU	0.945	2.618	13.788	0.706	1.706	9.483
2ndOU	0.412	0.763	6.54	0.227	0.624	4.511

Table A.2 Error comparison for 2D long reach test case at x =2720 m

x = 2720 m section	NRMSE %					
	N = 1			N = 2		
	Δx = 2 m	**Δx = 5 m**	**Δx = 10 m**	**Δx = 2 m**	**Δx = 5 m**	**Δx = 10 m**
FOU	0.979	4.222	15.304	0.879	4.259	14.525
QUICKEST	1.108	3.64	17.803	1.066	4.052	16.682
Superbee	1.199	3.758	17.644	0.914	2.235	15.048
MUSCL	1.069	3.952	17.116	0.773	2.247	14.718
Adaptive	1.064	3.47	16.521	0.81	2.097	13.636
5thOU	1.042	3.61	16.981	0.796	2.109	14.351
2ndOU	0.501	1.236	11.513	0.385	1.418	11.478

Table A.3 Convergence and elapsed time of coupled 3D model for varying grid coarseness in horizontal long reach test case

Discretization (m)	Average Convergence steps (n_{its})			Elapsed time (s)		
	FOU	QUICKEST-L	Average	FOU	QUICKEST-L	Average
Δx=1	3072	3029	3051	12234.29	9651.87	10943.08
Δx=2	1501	1425	1463	1364.94	2008.54	1686.74
Δx=5	713	648	681	243.71	261.95	252.83
Δx=10	502	433	468	125.38	319.01	222.195

Table A.4 Convergence and elapsed time of coupled 3D model for varying grid coarseness in inclined (45°) long reach test case

Discretization (m)	Average Convergence steps (n_{its})			Elapsed time (s)		
	FOU	QUICKEST-L	Average	FOU	QUICKEST-L	Average
Δx=1	2232	2196	2214	6558.75	6407.29	6483.02
Δx=2	1131	1070	1101	1124.63	1236.6	1180.615
Δx=5	449	462	456	137.02	122.58	129.8
Δx=10	399	400	400	58.51	80.18	69.345

APPENDIX B

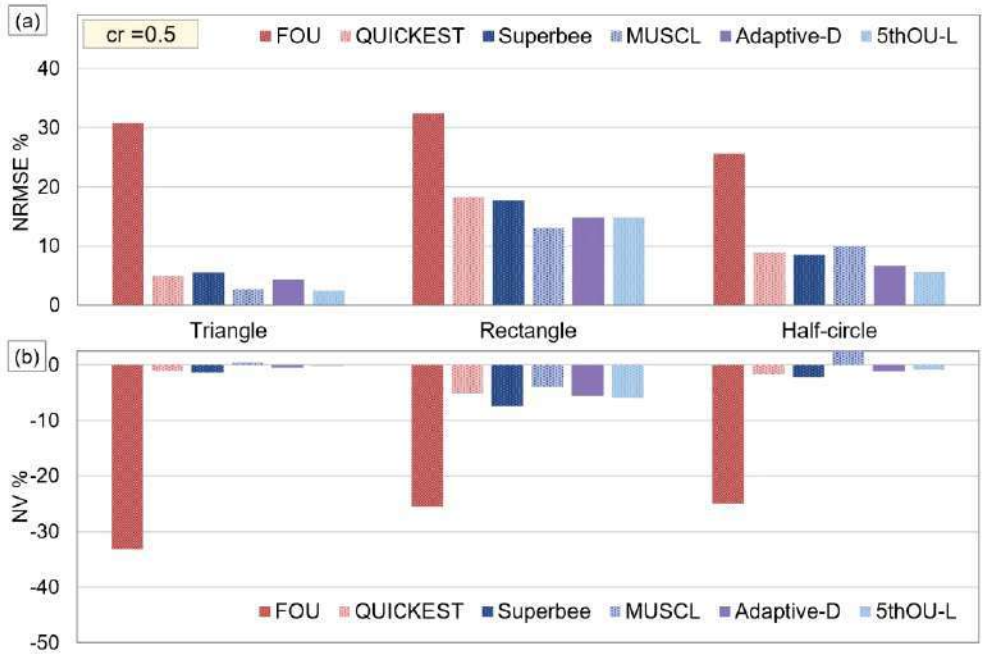

Figure B.1 Comparison between FOU and selected higher-order methods for $c_r = 0.05$ in 1D advection

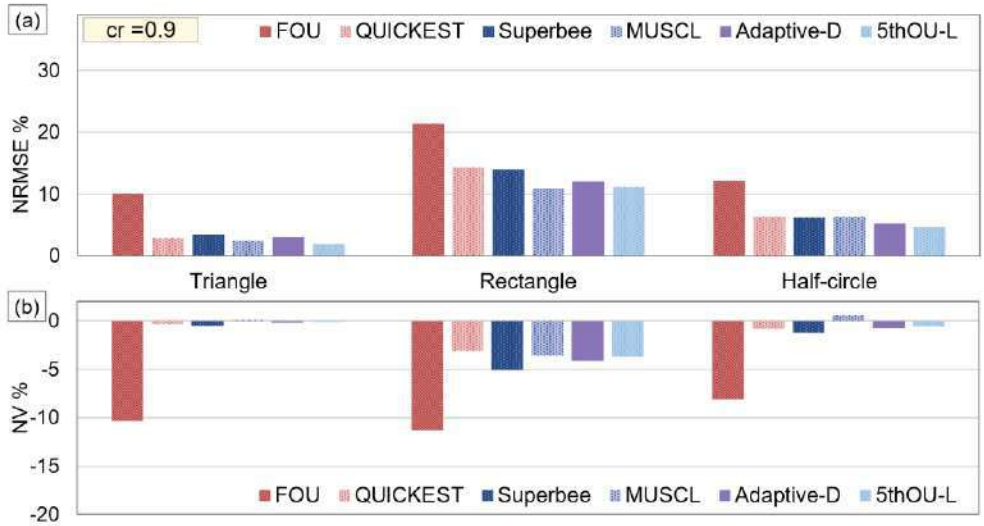

Figure B.2 Comparison between FOU and selected higher-order methods for $c_r = 0.09$ in 1D advection

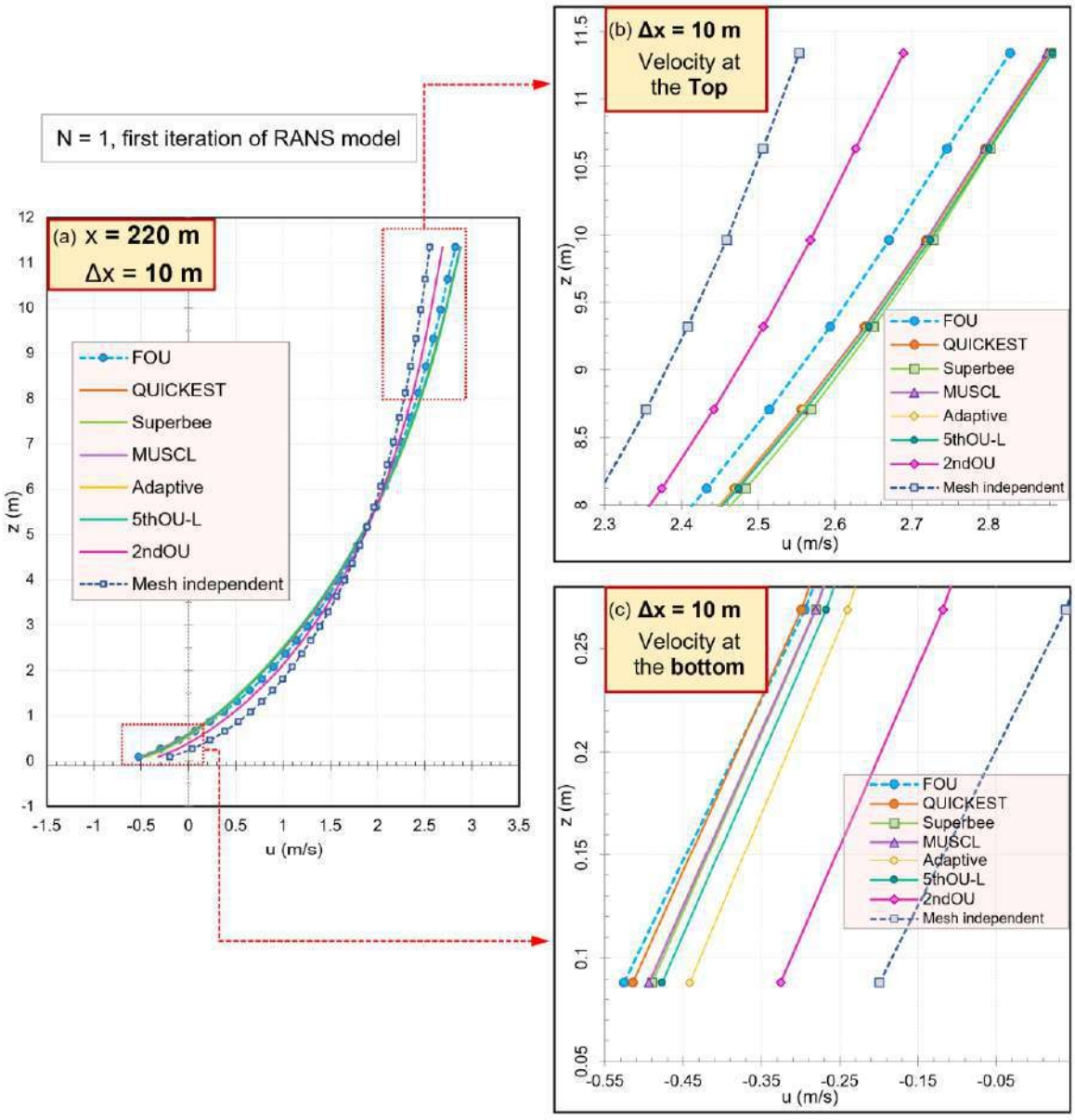

Figure B.3 Velocity profiles at x = 220 m, for Δx = 10 m (a) complete (b) top (c) bottom portion in 2D long reach test case

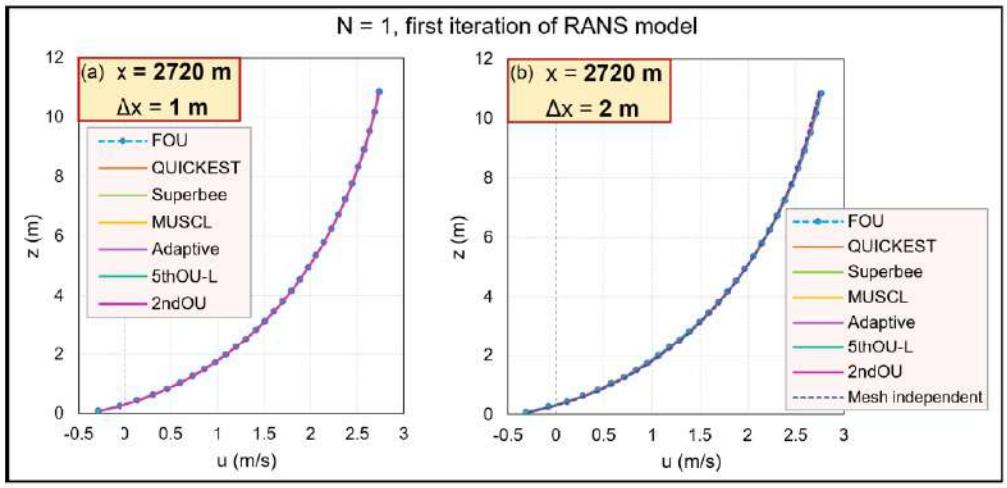

Figure B.4 Velocity profiles at x = 2720 m, for (a) Δx = 1 m (b) Δx = 2 m, in 2D long reach test case

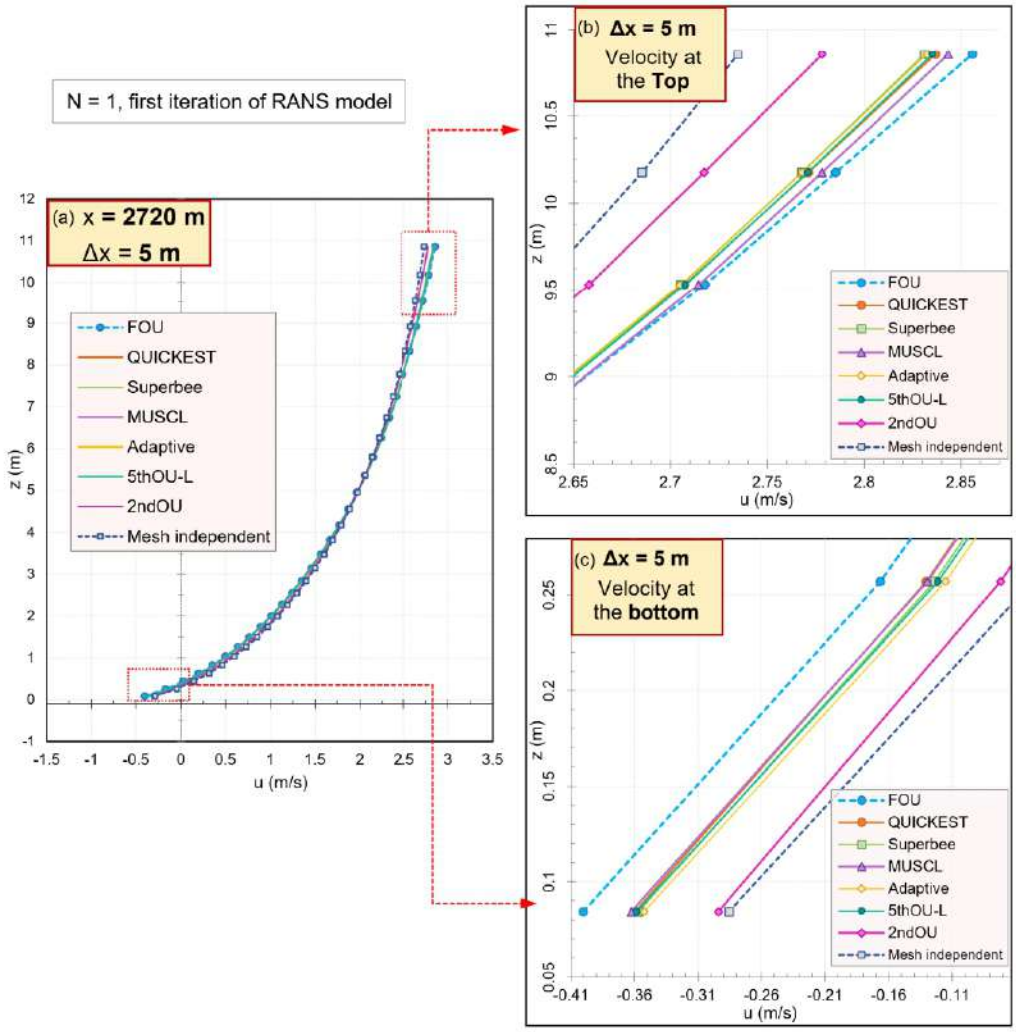

Figure B.5 Velocity profiles at x = 2720 m, for Δx = 5 m (a) complete (b) top (c) bottom portion, in 2D long reach test case

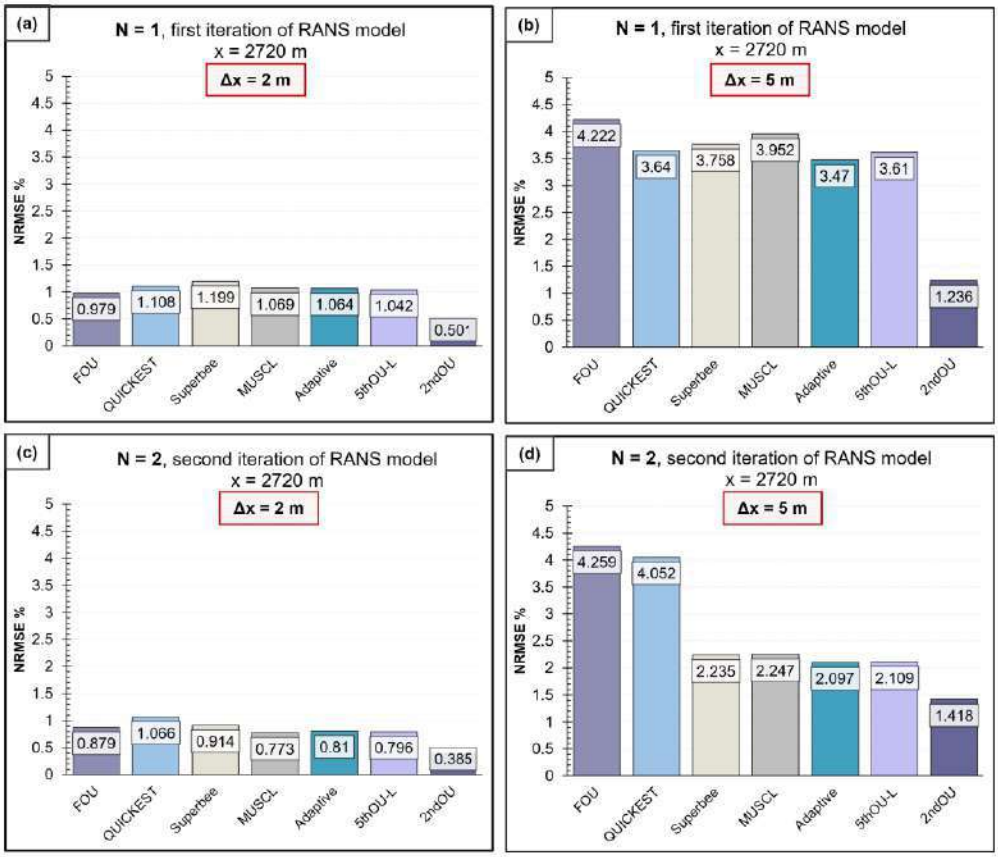

Figure B.6 Comparison between FOU and selected higher-order methods for increased grid spacing (a) N=1, Δx = 2 m (b) N=1, Δx = 5 m (c) N=2, Δx = 2 m (d) N=2, Δx = 5 m

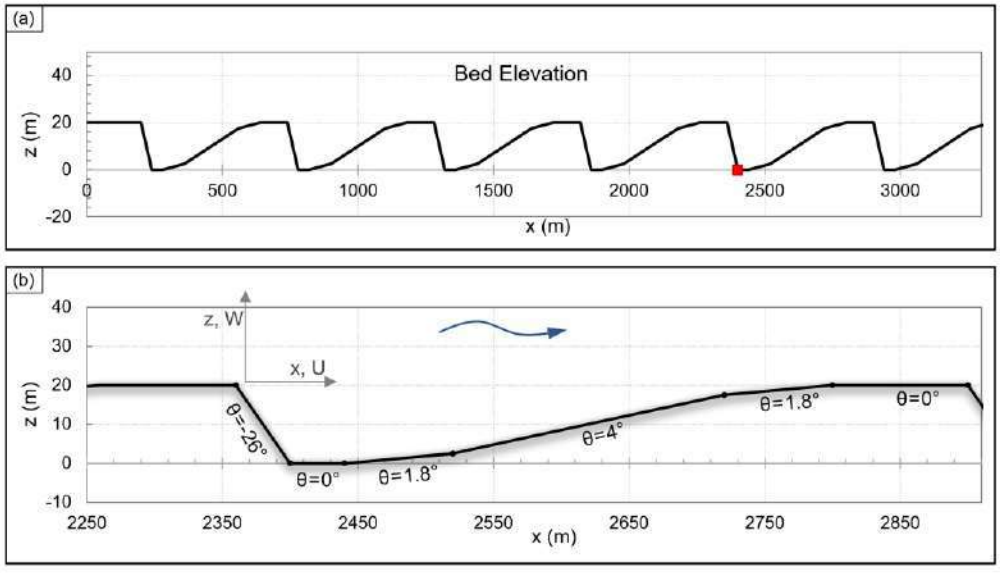

Figure B.7 Bed elevation of larger hypothetical test case (only for FOU and 2ndOU)

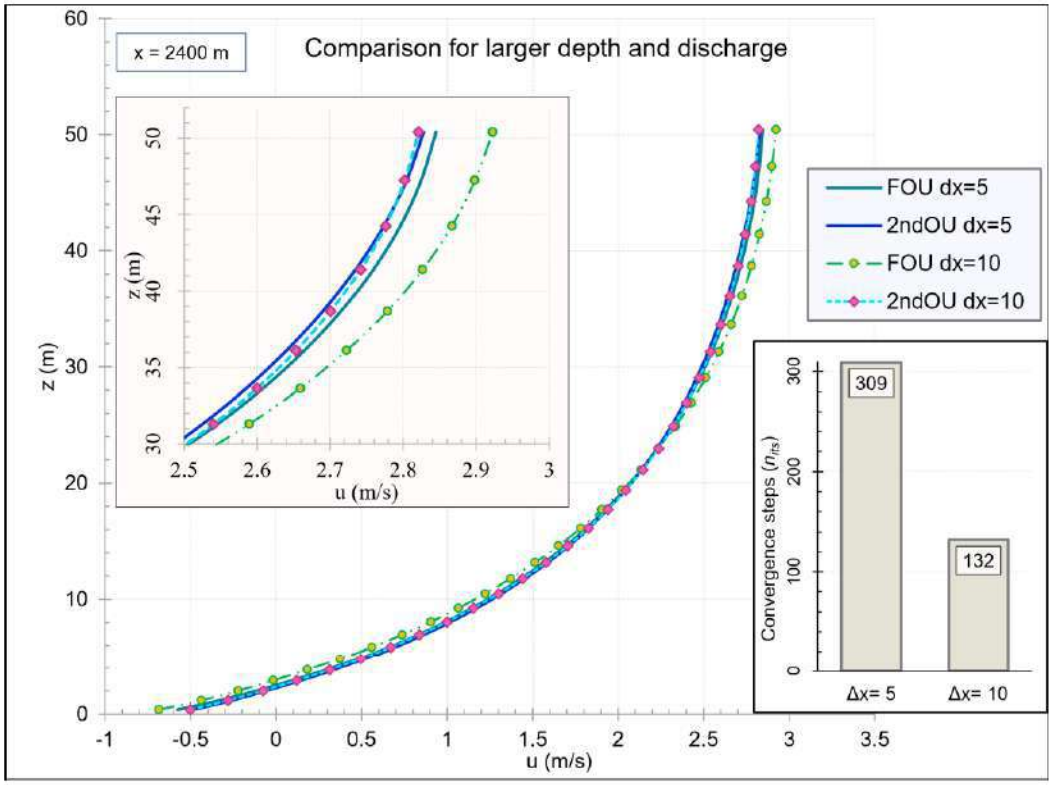

Figure B.8 Comparison of velocity profiles and convergence iterations in larger hypothetical bed

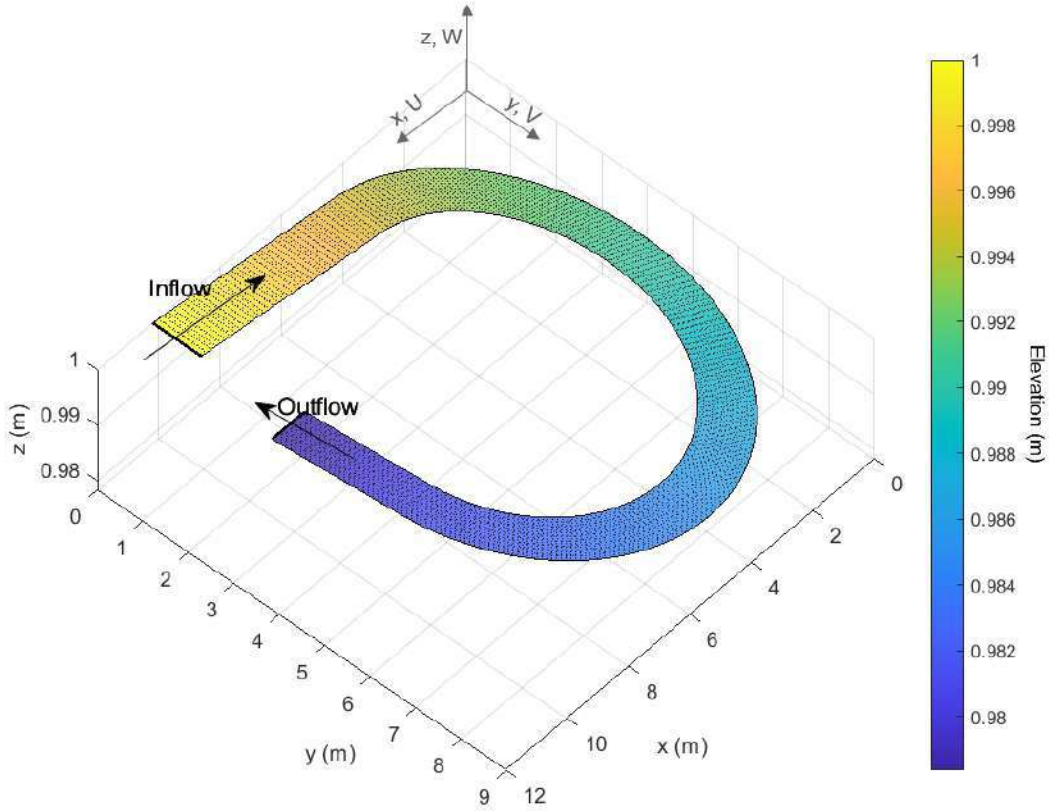

Figure B.9 Bed elevation for 3D flow in a curved channel

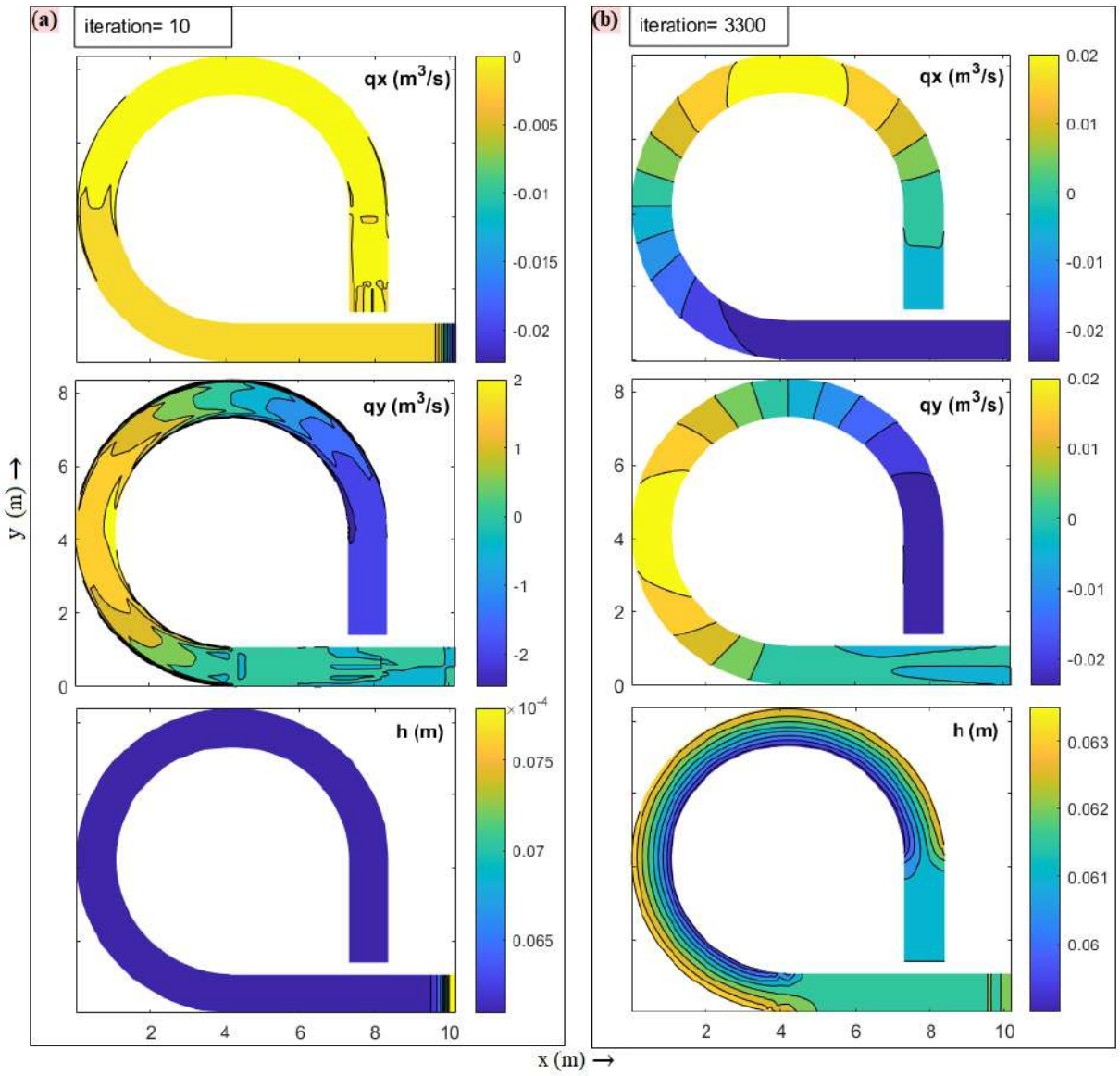

Figure B.10 3D depth-averaged model converging gradually for the curved channel conidtion

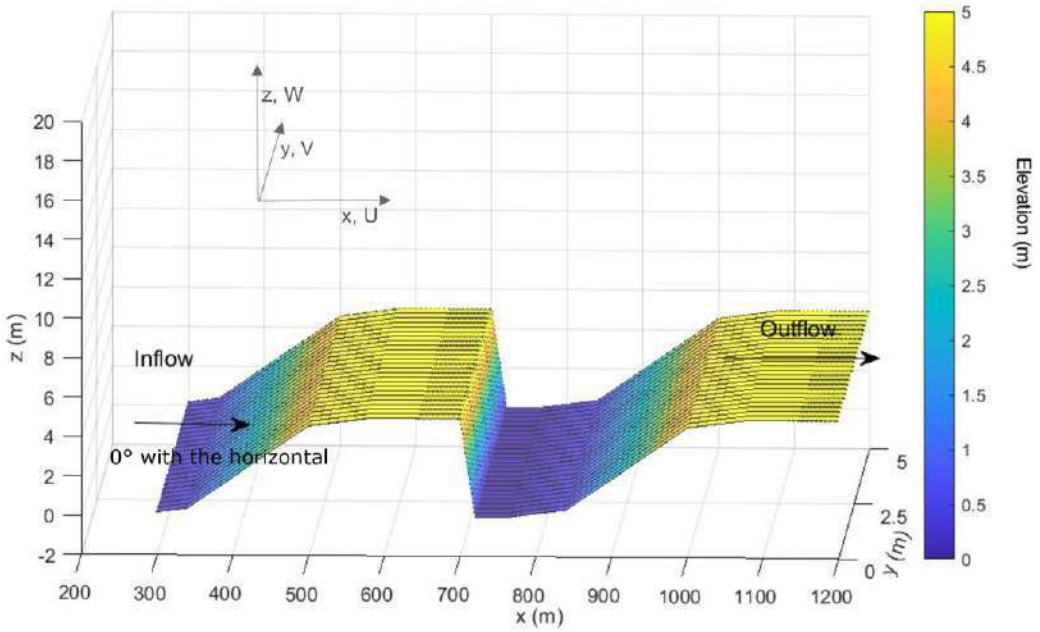

Figure B.11 Bed elevation for 3D horizontal long reach test case

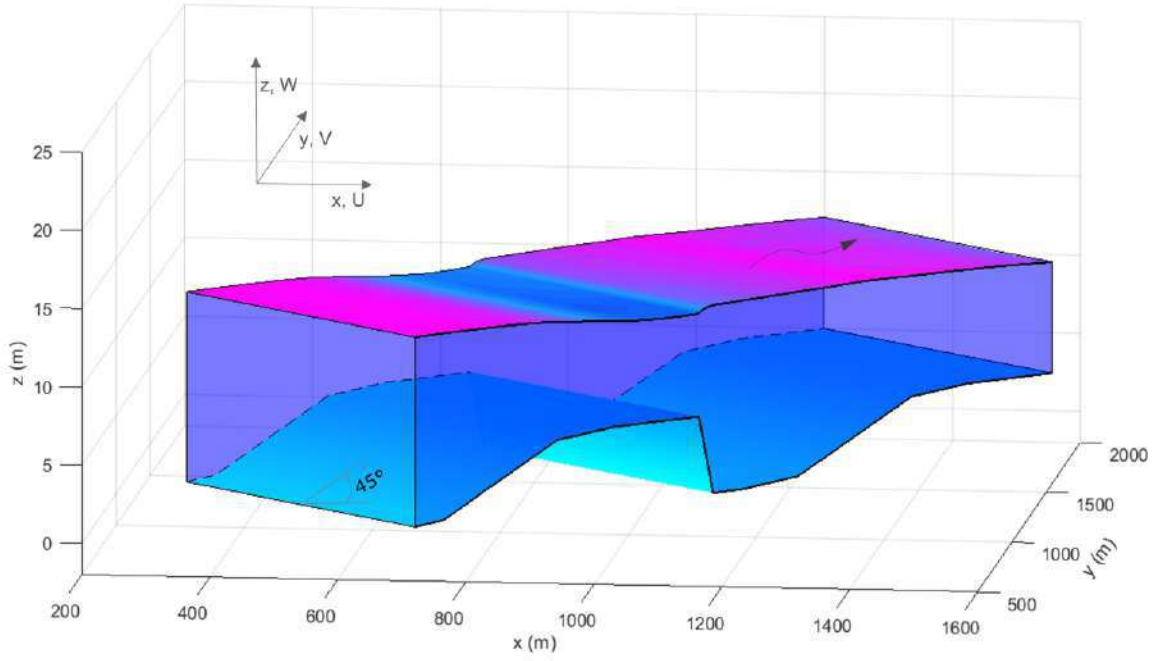

Figure B.12 Simulated water level for 3D inclined (45°) long reach test case

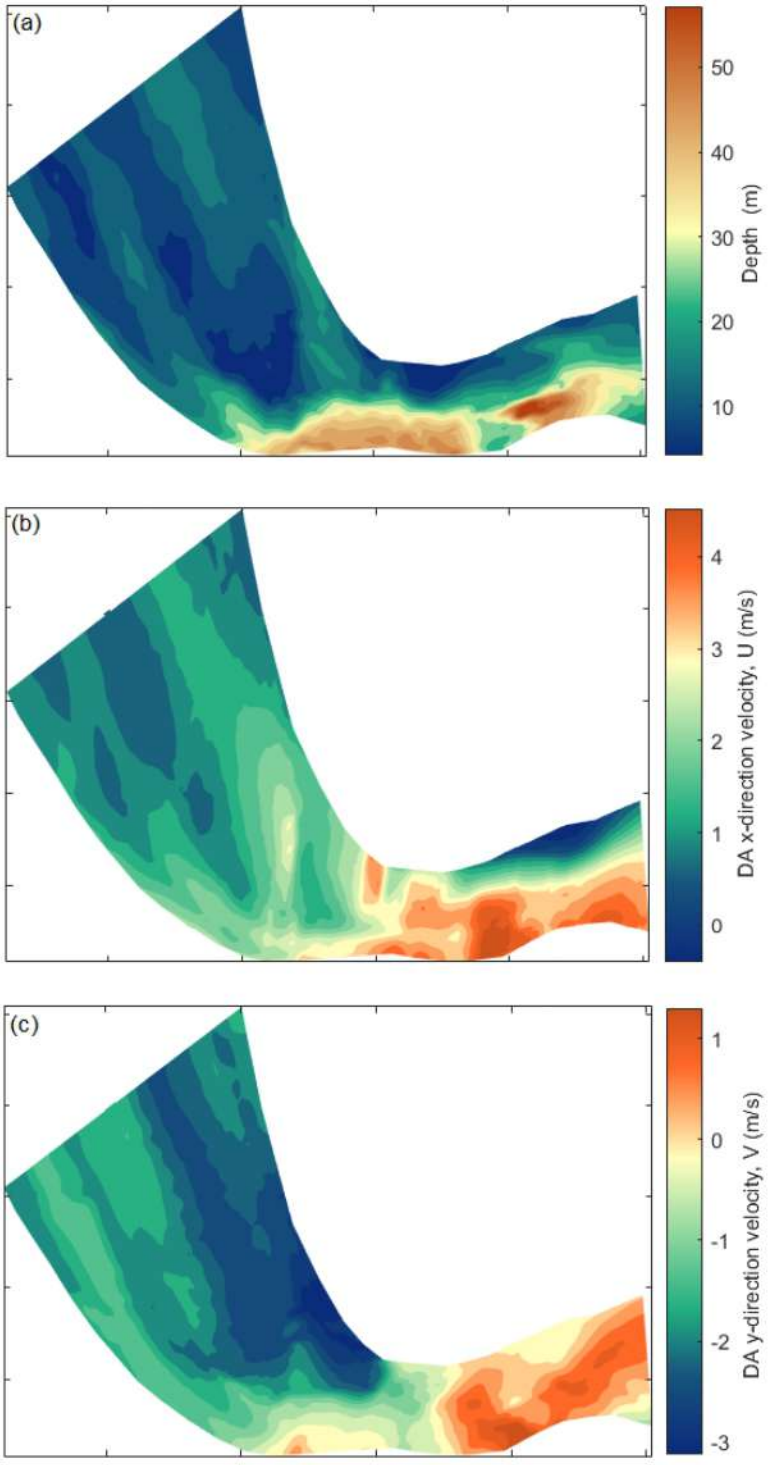

Figure B.13 (a) Water depth (b) depth-averaged x-direction velocity (c) depth-averaged y-direction velocity from River2D

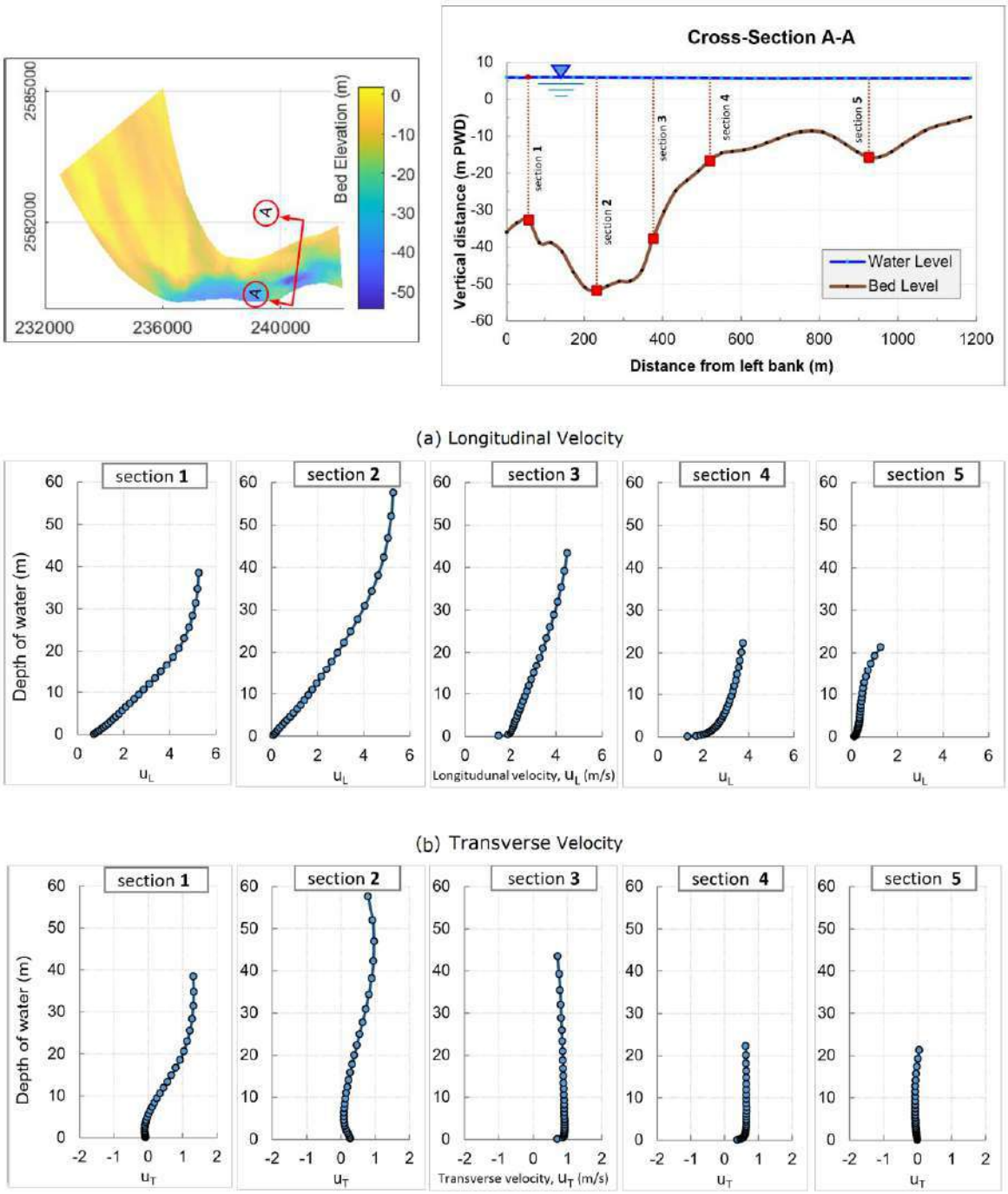

Figure B.14 Vertical velocity distributions found from the 3D QUICKEST model along a cross section of the channel near Naria

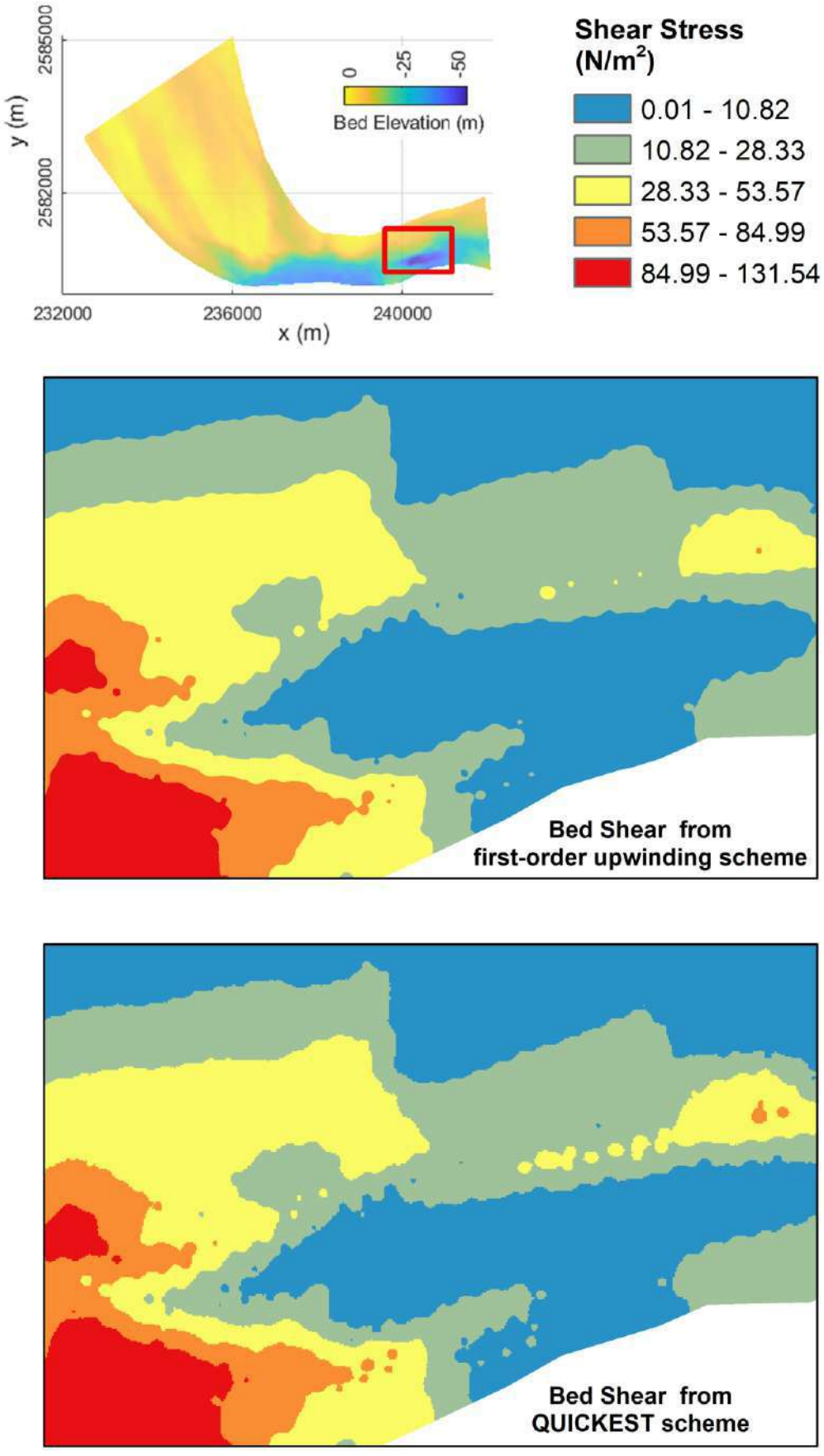

Figure B.15 Variation in bed shear stress found from the different schemes (first-order upwinding and QUICKEST)

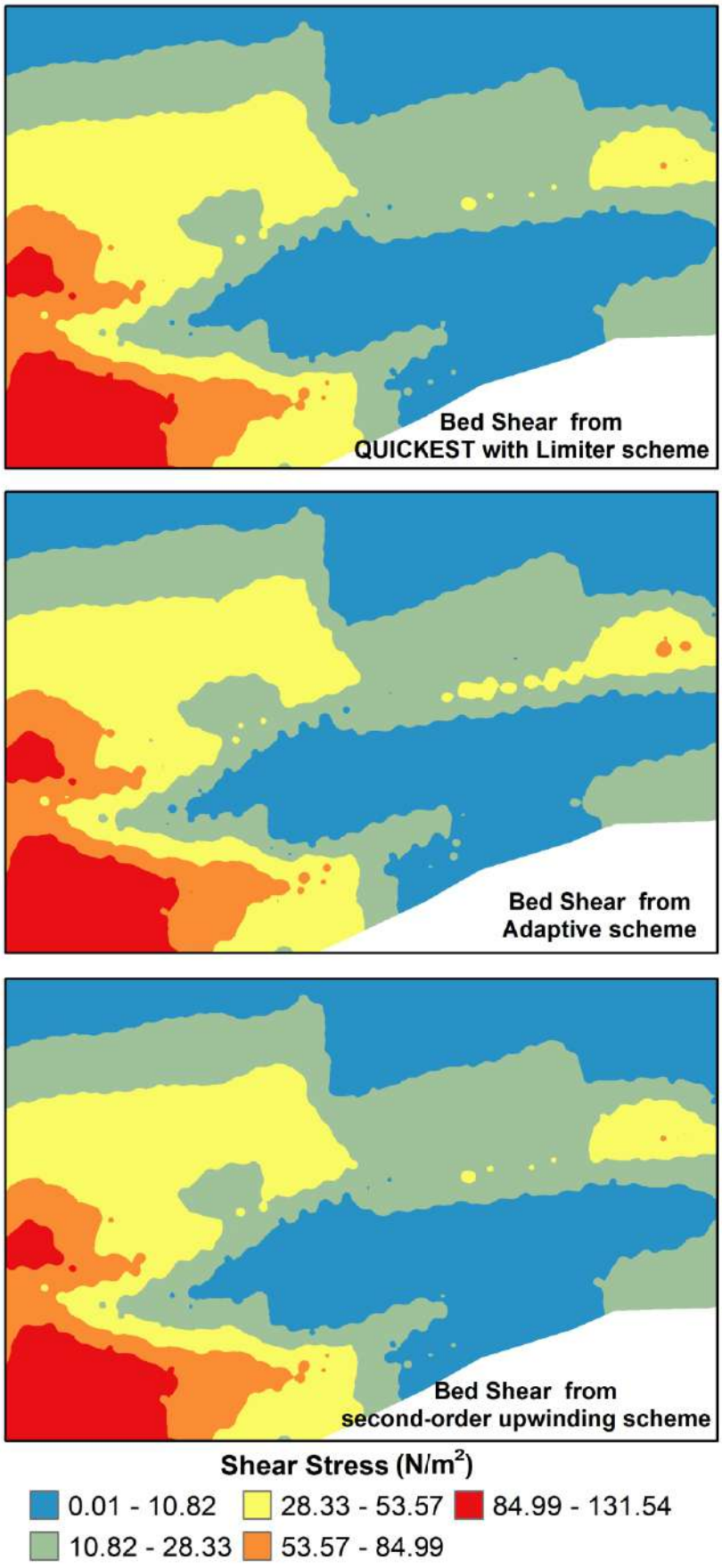

Figure B.16 Variation in bed shear stress found from the different schemes (QUICKEST with limiter, Adaptive and second-order upwinding)